



Thermophotovoltaic Energy Conversion Development Program

Kailash Shukla, Edward Doyle, and Frederick Becker
Thermo Power Corporation, Tecogen Division
A Thermo Electron Company
Waltham, Massachusetts

The NASA STI Program Office . . . in Profile

Since its founding, NASA has been dedicated to the advancement of aeronautics and space science. The NASA Scientific and Technical Information (STI) Program Office plays a key part in helping NASA maintain this important role.

The NASA STI Program Office is operated by Langley Research Center, the Lead Center for NASA's scientific and technical information. The NASA STI Program Office provides access to the NASA STI Database, the largest collection of aeronautical and space science STI in the world. The Program Office is also NASA's institutional mechanism for disseminating the results of its research and development activities. These results are published by NASA in the NASA STI Report Series, which includes the following report types:

- **TECHNICAL PUBLICATION.** Reports of completed research or a major significant phase of research that present the results of NASA programs and include extensive data or theoretical analysis. Includes compilations of significant scientific and technical data and information deemed to be of continuing reference value. NASA's counterpart of peer-reviewed formal professional papers but has less stringent limitations on manuscript length and extent of graphic presentations.
- **TECHNICAL MEMORANDUM.** Scientific and technical findings that are preliminary or of specialized interest, e.g., quick release reports, working papers, and bibliographies that contain minimal annotation. Does not contain extensive analysis.
- **CONTRACTOR REPORT.** Scientific and technical findings by NASA-sponsored contractors and grantees.

- **CONFERENCE PUBLICATION.** Collected papers from scientific and technical conferences, symposia, seminars, or other meetings sponsored or cosponsored by NASA.
- **SPECIAL PUBLICATION.** Scientific, technical, or historical information from NASA programs, projects, and missions, often concerned with subjects having substantial public interest.
- **TECHNICAL TRANSLATION.** English-language translations of foreign scientific and technical material pertinent to NASA's mission.

Specialized services that complement the STI Program Office's diverse offerings include creating custom thesauri, building customized data bases, organizing and publishing research results . . . even providing videos.

For more information about the NASA STI Program Office, see the following:

- Access the NASA STI Program Home Page at <http://www.sti.nasa.gov>
- E-mail your question via the Internet to help@sti.nasa.gov
- Fax your question to the NASA Access Help Desk at (301) 621-0134
- Telephone the NASA Access Help Desk at (301) 621-0390
- Write to:
NASA Access Help Desk
NASA Center for Aerospace Information
7121 Standard Drive
Hanover, MD 21076



Thermophotovoltaic Energy Conversion Development Program

Kailash Shukla, Edward Doyle, and Frederick Becker
Thermo Power Corporation, Tecogen Division
A Thermo Electron Company
Waltham, Massachusetts

Prepared under Grant NAS3-27565

National Aeronautics and
Space Administration

Lewis Research Center

Trade names or manufacturers' names are used in this report for identification only. This usage does not constitute an official endorsement, either expressed or implied, by the National Aeronautics and Space Administration.

Available from

NASA Center for Aerospace Information
7121 Standard Drive
Hanover, MD 21076
Price Code: A05

National Technical Information Service
5287 Port Royal Road
Springfield, VA 22100
Price Code: A05

FOREWORD

This work has been supported by DARPA (U.S. Department of Defense) under the management of NASA Lewis Research Center. The authors acknowledge the guidance provided by Dr. Robert Rosenfeld of DARPA and Mr. David Wilt of NASA-Lewis. We also acknowledge Mr. Phillip Jenkins of Essential Research and Mr. Steven Flammang of TECSTAR for contributing to this report.

TABLE OF CONTENTS

SUMMARY	1
1. INTRODUCTION.....	7
2. TECHNICAL APPROACH.....	9
2.1 SELECTIVE VS. BROAD-BAND EMITTERS	9
2.2 SYSTEMS ANALYSIS	10
3. SYSTEM DESIGN.....	15
4. COMPONENTS DEVELOPMENT.....	21
4.1 EMITTER DEVELOPMENT	22
4.1.1 Total Power Density Measurements	23
4.1.2 Spectrally Resolved Emitter Power.....	24
4.1.3 Long Wavelength Characterization of the Pathfinder Emitter.....	25
4.1.4 Temperature Measurement of Ytterbia Fibers	27
4.1.5 Radiation Distribution at PV Cell Plane	29
4.2 OPTICAL FILTER DEVELOPMENT	31
4.2.1 Dielectric Stack Filters.....	31
4.2.2 Conductive Film Filters.....	34
4.3 PV ARRAY AND HEAT SINK DEVELOPMENT.....	36
4.3.1 PV Cell Module Design	38
4.3.2 PV Module Fabrication	47
4.3.3 PV Module Testing	48
4.4 RECUPERATOR DEVELOPMENT	50
5. LABORATORY PROTOTYPE DEVELOPMENT.....	55
5.1 CONFIGURATION A LABORATORY PROTOTYPE.....	55
5.2 CONFIGURATION B LABORATORY PROTOTYPE	61
6. SINGLE MODULE TPV SYSTEM MODEL	69
6.1 PURPOSE	69
6.2 DESCRIPTION OF MODEL.....	69
6.3 MODEL RESULTS	73
7. CONCLUSIONS	79

LIST OF FIGURES

2.1	TPV Power Source Components	9
2.2	Ytterbia Emissive Power and Silicon PV Cell Efficiency	11
2.3	Erbia Emissive Power and Gallium Antimonide PV Cell Efficiency	12
3.1	Supported Continuous Fiber Radiant Structure.....	15
3.2	Micromixing Approach – Option A	16
3.3	Micromixing Approach – Option B.....	16
3.4	Configuration A, Two-Module, TPV Converter Schematic.....	18
3.5	Configuration B, Two-Module, TPV Converter Schematic	18
4.1	"Pathfinder" Emitter System.....	21
4.2	"Pathfinder" Emitter System with Control Panel	22
4.3a	Geometry for Power Density Measurements Using a 1.5" Diameter Aperture	23
4.3b	Geometry for Power Density Measurements Using a 0.5" Diameter Aperture	23
4.4	Spectral Exitance of an Emitter Viewed Through Two Quartz Windows	25
4.5	Percent Transmission of Various IR Window Materials.....	26
4.6	Spectral Ranges Characterized Using Various Window Materials	26
4.7	Exitance of an Emitter at Two Different Temperatures	28
4.8	Emissivity of a Single-Density Emitter at a Temperature of 2093 K	28
4.9	View Factor for Prototype TPV System – Emitter to PV Cell Plane	30
4.10	Measured View Factor for Prototype TPV System – Emitter to PV Cell Plane.....	30
4.11	Micrograph Showing Crazing in a Dielectric Filter	32

LIST OF FIGURES (Continued)

4.12	Transmission of Dielectric Filter a) As Received From the Manufacturer, and b) After Furnace Annealing.....	32
4.13	Absorption of a Dielectric Stack Filter a) As Received From the Manufacturer, and b) After Furnace Annealing.....	33
4.14	Dielectric Stack Filter Performance.....	33
4.15	Transmission, Reflection and Absorption of an ITO Filter	35
4.16	Model Transmission for a Composite Filter Composed of a Dielectric Stack and an ITO Thin Film	35
4.17	Response of Ytterbia Emitter and Silicon Cells	36
4.18	Baseline PERL Cell	37
4.19	Cell to Heat Sink Interface Options.....	40
4.20	PV Module Assembly Block Diagram	42
4.21	Side and Front View of PV Array Assembly.....	42
4.22	Module Thermal Performance	43
4.23	Flat Copper Cell Interconnect.....	44
4.24	Thirty Cell Module Under 1x Solar Concentration	45
4.25	PV Module Under 12x Concentration	46
4.26	PV Module Fabrication and Test Flow Chart.....	47
4.27	Spectral Characteristics Under Concentration.....	48
4.28	V_{OC} , I_{SC} and FF vs. Concentration.....	49
4.29	Air Preheat Temperature vs. Effectiveness for a Range of Flue Gas Inlet Temperatures	50
4.30	Ceramic Recuperator	52

LIST OF FIGURES (Continued)

5.1	Configuration A Emitter	56
5.2	Configuration A Water-Cooled Fuel Tube Manifold Assembly	56
5.3	Configuration A Prototype – Test Setup	57
5.4	Configuration A Prototype – Emitter Viewed Through a Dielectric Filter	57
5.5	Configuration A Prototype – Assembly With Swing-Away PV Array	58
5.6	Configuration A Prototype – Test Results	58
5.7	Location of Cells in the Three Parallel Circuit of PV Array	59
5.8	Configuration A Current – Voltage Characteristics	60
5.9	Configuration A Power Characteristics	60
5.10	Configuration A Fill Factor and Open Circuit Voltage	61
5.11	Configuration B Emitter	62
5.12	Configuration B Manifold Assembly	63
5.13	Configuration B Prototype – Partial Assembly (Side View)	63
5.14	Configuration B Prototype – Partial Assembly (Front View)	64
5.15	Configuration B Prototype – Emitter Face	64
5.16	Configuration B Prototype – Recuperator (Hot End)	65
5.17	Configuration B Prototype – Recuperator (Cold End)	65
5.18	Configuration B Laboratory Prototype	65
5.19	Configuration B Prototype – Test Data	66
5.20	Configuration B Prototype – Test Data	67

LIST OF FIGURES (Continued)

5.21	PV Array Power vs. Emitter Convertible Exitance for Configuration B Prototype	68
6.1	Single Module TPV System Model	70
6.2	TPV System Model Results – One Module Size	75
6.3	TPV System Model Results – One Module Size	75
6.4	TPV System Model Results – One Module Size	75
6.5	TPV System Model Results – One Module Size	76
6.6	TPV System Model Results – One Module Size	76
6.7	TPV System Model Results – One Module Size	76
6.8	TPV System Model Results – One Module Size	77
6.9	TPV System Model Results – One Module Size	77
6.10	TPV System Model Results – One Module Size	77
7.1	PV Cell Efficiency and Emitter Spectral Exitance vs. Wavelength	80
7.2	PV Array Power vs. Emitter Convertible Exitance for a Two-Module Laboratory Prototype	81

LIST OF TABLES

1.1	TPV Prototype Design Specifications	3
2.1	Comparison of Selected Emitter and PV Cell Combinations.....	13
3.1	TPV Prototype Design Specifications	19
4.1	Total Radiative Power Density of a Single-Density Emitter Viewed Through Two Quartz Windows	24
4.2	IR Content of an Emitter Viewed Through Two Quartz Windows.....	27
4.3	PV Array Design Specifications	37
4.4	Si Wafer Test Results	46
4.5	TPV Cell Module Performance Summary.....	49
4.6	Ceramic Recuperator Material Options	51
4.7	Recuperator Core Dimensional Characteristics.....	52
4.8	Recuperator Heat Transfer Effectiveness of Various Cell Density Cores at Several Fuel Firing Rates.....	53
6.1	Radiation Regions and Component Treatment for TPV System Model	72
7.1	PV Cell Characteristics.....	80

SUMMARY

Thermophotovoltaic (TPV) energy conversion, which uses photovoltaic (PV) cells to directly convert radiant thermal energy into electric power, has a number of important advantages for portable power generation in military applications. Since TPV is a direct energy conversion technology with no moving parts in the energy conversion system, it has the potential to provide quiet, reliable, maintenance-free electric power for thousands of hours. These systems also have the potential to be as efficient as small portable engine generators, operate on military logistic fuels, and start and operate in sub-freezing environments.

Individual components needed to produce TPV power systems such as PV cells, emitters, and optical filters are actively being developed by various agencies and companies. However, the key issue in realizing commercially viable TPV systems is the integrated performance of the major components and its impact on overall system efficiency and cost. In this regard, Thermo Power Corporation, with funding support from DARPA/NASA-Lewis, is developing completely integrated TPV power sources in the range of 100 to 500 watts to demonstrate the technological pathways for achieving system efficiencies and cost effectiveness consistent with the needs of military and commercial markets. The TPV generators being developed will initially use gaseous fuels with future capability for operating on liquid hydrocarbon fuels.

Technical Approach

The technical approach taken in this project is to use a wavelength selective fibrous emitter radiating to a bandgap matched photovoltaic array to minimize thermal and optical recuperation requirements, as well as nonrecoverable heat losses. While a well-matched emitter-photoconverter has significant design advantages, high PV cell efficiency and high optical and thermal recuperation is critical for high system performance. It is also important that other potential loss mechanisms such as photoconverter fill factor, radiation view factor, ancillary power requirements, and nonrecoverable thermal losses from optical windows and insulating surfaces be minimized.

For the initial prototype systems, fibrous ytterbia emitters, radiating in a wavelength selective band centered at 980 nm, are matched with high efficiency silicon photovoltaic converters. The ytterbia selective emitter system is based on Thermo Power's patented supported continuous fiber radiant structure (SCFRS) that can operate up to temperatures of 2100 K with good thermal shock resistance and rapid response time. The emitter consists of continuous fibers woven into a porous ceramic base. As such, the emitter preserves the advantages of gas light mantles that have traditionally operated at high temperatures for long times. Unlike gas mantles, the Thermo Power emitter can be made in planar, 15 cm x 15 cm or larger tiles without becoming fragile. A cellulose support process that is based on textile precursors is employed to fabricate the fibrous emitter structure. Continuous filament rayon yarn impregnated with aqueous metal salt solution (ytterbium nitrate in this case) is tufted into the porous ceramic support much like a rug-making process that yields an uncut looped pile. After tufting, the treated rayon is converted into a ceramic by means of a controlled heat treatment process.

System Design

Since the combustion air is preheated to much above the auto-ignition temperature of the fuel for high system efficiency, fuel has to be mixed with the air and combusted in close proximity of the fibers just above the surface of the substrate. This requirement is one of the most challenging aspects of the generator design, since it has implications for the temperature uniformity of the fibers and off-band radiation leaving the emitter. Several design approaches for mixing fuel and preheated air were analyzed and bench tested to determine the feasibility of obtaining stable combustion and uniform temperature distribution of the fibrous radiating surface. The two most promising configurations were selected for laboratory prototype development.

In Configuration A, fuel is delivered through perforated fuel tubes from the front of the emitter, and in Configuration B, fuel is delivered through fuel tubes from the back of the emitter. In both approaches, fuel is delivered from the fuel plenum through fuel tubes to very near the surface of the substrate and mixed with the preheated air. The objective in both cases is to achieve rapid air-fuel mixing to complete combustion within the fiber bed for good fuel efficiency. Also, a sufficient number of orifices (in Configuration A) and fuel tubes (in Configuration B) are used to provide uniformity of temperature distribution. To protect the PV array from direct contact of hot combustion gases and to reflect any nonconvertible radiation back to the emitter, two quartz windows with optical filters are used. Cooling air passes between the two windows to maintain them at temperatures consistent with the capability of the optical coatings.

In designing these systems, we established a module size based on the availability of critical component parts like ceramic emitter substrate, ceramic core for the recuperator, and the base material for optical filter (quartz). This was done for both cost and delivery reasons. When these criteria were applied, the active emitter area on a single substrate was limited to about 12 cm x 12 cm, the face area of the recuperator to 15 cm x 15 cm, and the maximum filter size to 15.25 cm x 15.25 cm. Assuming the dimensions of the PV array to be same as the active emitter area, the gross power output of a single module was determined to be in the range of 100 to 125 watts.

A detailed computer model was developed for a single module TPV system of the specific geometry and configuration of the systems under development. The purpose was: to provide an accurate model for predicting the performance of the TPV systems under development and comparing it to the test results, to gain a better understanding of the impact of various parameters on the performance of the overall TPV system, and to accurately predict the overall system performance gains that could be achieved with specific component improvements. The predictions can readily be extended to multiple module systems.

The design specifications for a two module engineering prototype generator developed during this phase of the program and for an advanced prototype generator are presented in Table 1.1. The current prototype generator is designed to operate at an emitter temperature of 2000 K and an air preheat temperature of 1350 K. These temperatures were selected based on our operating experience with fibrous ytterbia emitters and the temperature capabilities of materials readily available for fabrication of the ceramic recuperator. A detailed computer model of the prototype TPV system has also shown that the power density and efficiency of the system continues to increase as these temperatures are increased when an efficient optical filter is used. For the advanced prototype, the emitter temperature will be increased to 2100 K and the air preheat temperature will be increased to 1650 K. This will require the use of a higher temperature ceramic material for the recuperator.

Table 1.1 TPV Prototype Design Specifications

	Phase I Prototype	Advanced Prototype
Emitter Temperature – K	2000	2100
Air Preheat Temperature – K	1350	1650
Average Emitter Exitance – W/cm ²	3.50	5.00
Average Exitance View Factor	0.80	0.80
Average Exitance @ Array – W/cm ²	2.80	4.00
Emitter Area (2 Emitters) – cm ²	291	291
PV Array Area – cm ²	288	288
PV Cell Efficiency	38%	38%
PV Array Uniformity Factor	80%	85%
Gross Power (2 Emitters) – W	245	372
Ancillary Power – W	75	57
Net Power – W	170	315
Gross System Efficiency	6.5%	8.8%
Net System Efficiency	4.5%	7.5%

Systems Development

To characterize the emitter system and to facilitate development of the optical filter, PV cell and the heat sink, a 1/4 scale “pathfinder” emitter system was designed and fabricated. A number of different types of emitters were designed, fabricated, and tested. The variations included two substrate types, three overall fiber densities (half, single and double), three emitter sizes (7.6 cm x 7.6 cm, 7.6 cm x 11.4 cm, and 12 cm x 12 cm), and two fiber lengths. The characterization of the pathfinder emitter was done by Essential Research Inc. The following measurements were made: spectrally resolved emitter power density from 0.7 to 3.0 μm , total power density over all wavelengths, temperature measurements of the two quartz windows, and false-color images of the Pathfinder emitter using a CCD IR camera. In addition, new measurement techniques were used to calculate the temperature of emitter fibers and the long IR power density. The measurement showed that the emitter has a strong emission peak at 980 nm, silicon-convertible power of 3.24 W/cm², and total radiative power of 10.67 W/cm².

The temperature at the emitter fibers and the radiant exitance (W/cm²) from the emitter fibers was shown to be fairly uniform through the measurements made by Essential Research Inc. Uniform exitance at the emitter, however, does not result in uniform radiation at the PV cell plane. A simple view factor model was used initially to determine the magnitude of the non-uniformity of the radiation at the PV cell plane. The model, which accounted for the refractory walls interconnecting the emitter and PV array, predicted an average view factor (W/cm² @ array/W/cm² @ emitter) of 73% with a variation from 53% near the edge of the array to ~100% at the center of the array. Later measurements were made using the individual cells in the PV array to measure the non-uniformity and compare it to the model. The measured view factor varied from ~52% near the edge of the array to ~100% at the center of the array with an average of 80%.

Two types of filters were investigated for optical performance and mechanical stability by Essential Research Inc. One was a multilayer dielectric stack filter and the other was a thin “transparent” conductive coating also known as a solar control film. Use of the dielectric stack filter reduced the total output power to 60% of the unfiltered output and the silicon convertible radiation dropped by only 2%. In the near IR, the wavelength range between 1180 and 3500 nm and output power was reduced by a factor of four. With the use of the dielectric filter, the ratio of in-band to total radiation (convertible fraction) thus increased from 30% to 50%. Of the two types of filters evaluated, dielectric stack was chosen over thin film conductive coatings for use during this phase of the project, because of its higher in-band transmission, lower absorption, and high reflectivity in the out-of-band region. However, a composite filter with dielectric stack on one side and an ITO film on the other may be a viable option for a future prototype.

A compact, monolithic, high-efficiency, counter-flow, ceramic recuperator was fabricated and tested to provide air preheat temperatures of up to 1350 K. The desired air preheat temperature and the flue gas temperature are the key determinants of the recuperator material. However, temperature-related effects such as material differential expansion, thermal shock, and thermal conductivity must be considered and accounted for in a recuperator design. Metallic heat exchangers, used most often in industry, have two major limitations – temperature and corrosion. When constructed of stainless steel, the bulk material temperature should not exceed 925 K and the flue gas inlet temperature should be less than 1075 K. A stainless steel heat exchanger must therefore be protected by diluting the flue gas which will lower its performance. Ceramics can withstand considerably higher temperatures and are less susceptible to attack by flue gas constituents. However, proper design features are required for ceramic recuperators to achieve compact size and leak-free operation as well as avoid temperature-related problems such as thermal stress, fatigue cracks, and plastic deformation. The baseline material chosen for the initial prototypes was cordierite ($2\text{MgO} \cdot 2\text{Al}_2\text{O}_3 \cdot 5\text{SiO}_2$). Future recuperators will be fabricated using higher temperature materials like silicon carbide and whisker reinforced alumina.

The development of the silicon cell module and heat sink system was done by TECSTAR INC., Applied Solar Division. The primary objective of TECSTAR’s effort was to develop a photocell module whose performance was optimized for the operating characteristics of the Thermo Power ytterbia selective emitter. This requirement meant that the peak monochromatic efficiency of the photocell ideally should be about 45% and occur at or beyond (higher wavelength) the ytterbia emission peak at 980 nm. The PV cells provided by TECSTAR had a peak monochromatic cell efficiency of 35% at 920 nm. At the ytterbia emission peak of 980 nm, the monochromatic cell efficiency dropped to 33% and continued to drop at higher wavelengths where the ytterbia emitter was still emitting strongly. As a result, the overall efficiency of this cell in converting radiation below 1180 nm, was reduced to 27% when matched with the ytterbia emitter. The characteristics of the TECSTAR cells were compared to data provided by another supplier of TPV silicon cells, SunPower Corporation. These “new PV cells”, which will be used in the next generation prototype, are much better matched to the ytterbia emitter. They have a peak monochromatic efficiency of 46% at the ytterbia peak of 980 nm and an overall efficiency of 38% when matched with the ytterbia emitter.

The two laboratory prototype TPV generators have been tested extensively. We have operated at emitter temperatures of 2000 K and air preheat temperatures of 1200 K for many hours and have demonstrated the feasibility of the micromixed surface combustion concept needed to operate at these conditions. A convertible exitance of 3.7 W/cm^2 has been measured at the emitter and, in separate tests of the optical

filter, a 50% convertible radiation fraction has been achieved. For the two module prototype which was tested without optical filters, a peak power output of 150 watts and a gross system efficiency of 1.0% was measured with the TECSTAR array at an emitter convertible exitance of 3.7 W/cm^2 and an air preheat temperature of 1200 K. At the same emitter convertible exitance level, the arrays with the new PV cells should produce ~290 watts. The higher power output projected for the new arrays also includes the impact of the higher packing factor and lower cell interconnection losses which are achievable with the new PV cells.

The power increase with the new array will also result in a corresponding increase in the overall system efficiency. Substantial further increases in the system efficiency will be made by incorporating the dielectric stack filters, raising the air preheat from 1200 K to 1350 K by increasing the recuperator core cell density from 16 cells/in² to 25 cells/in², and improving combustion air distribution across the emitter so that the average air/fuel ratio can be reduced substantially without local fuel-rich zones occurring. Based on projections made using the results from the detailed TPV system model, these changes could increase the gross system efficiency from the 1.0% measured with the two emitter prototype to ~4.8%.

Conclusions

The work performed on the program to date has identified the technological pathways for the development of efficient, portable thermophotovoltaic power sources in the power range of 100 to 500 watts. The technology is based on the use of rare earth selective emitters and matched photovoltaic cells. Highly efficient thermal and optical energy recovery are also an integral part of the technology. The technology has been demonstrated at the laboratory prototype level where the key components of the system – emitter, PV array, recuperator, and optical filter – have been integrated into an operating prototype. Future plans are to build and demonstrate a completely self-contained, portable TPV power source based on this technology.

1. INTRODUCTION

In both military and commercial markets a need exists for portable electric power units for a variety of applications. Examples of these applications include 20 to 100 watt person-portable power systems for communication equipment and soldier systems, 100 to 500 watt power systems for grid independent appliances, and greater than 500 watt systems for remote site instrumentation power, camping and construction site power generation, and emergency power source during net power outages. Many of these applications are currently powered by engine generators or batteries. Existing engine generators, however, are noisy, polluting, and of limited life. Batteries, on the other hand, have problems related to low power density, limited shelf life, limited charge-discharge cycling, minimal repair capability, high cost and disposal. Advanced power systems are, therefore, needed that do not have the limitations of motor generators or batteries and are quiet, have high power density, and are fueled systems (replenished from a fuel source) with long shelf life and low maintenance.

There are a number of competing technologies, in various stages of development, which are capable of meeting these requirements for portable power systems. These include fuel cells, alkali-metal-thermal-to-electric-conversion (AMTEC), thermoelectrics, and thermophotovoltaics (TPV). Of all these potential technologies, we believe thermophotovoltaics, which uses photovoltaic cells to directly convert radiant thermal energy into electrical power, is the most attractive approach. The continuous combustion used for TPV permits a greater degree of control of exhaust products and noise relative to internal combustion engines. The absence of moving parts in the main power stream is expected to provide vibration-free operation, low maintenance, and long life.

Fuel cells, which convert chemical energy directly into electricity by chemical reaction between an electrolyte and a fuel such as hydrogen or methanol, is the prime competitor to TPV for portable power systems. Fuel cells are more efficient than TPV by about a factor of 2. However, compared to fuel cells, TPV can operate in a subfreezing environment on a variety of fuels including logistic fuels, like diesel, JP4, and JP8. Thermoelectrics is a well established and reliable technology but is much lower in efficiency than TPV, and will remain so until advanced thermoelectric materials with higher conversion efficiencies can be developed. AMTEC, also referred to as the sodium heat engine, is an immature technology but has the potential of being competitive.

Of the direct conversion processes, TPV is potentially the least costly because of its simplicity and the availability of cost effective photoconverters. If all these advantages of TPV can be exploited, the range of potential applications for TPV systems can be quite diverse. TPV can also be coupled with other direct conversion systems to make a hybrid device. For example, AMTEC or thermoelectrics are compatible as a bottoming cycle to TPV, by coupling the waste heat from the high temperature emitter of a TPV system to the hot end of an AMTEC or thermoelectric converter.

Individual components needed to produce TPV power systems, such as PV cells, emitters, and optical filters, are actively being developed by various agencies and companies. However, the key issue in realizing commercially viable TPV systems is the integrated performance of the major components and its impact on overall system efficiency and cost. In this regard, the key objective of this program was to develop an integrated TPV energy conversion system to demonstrate the technological pathways for achieving system efficiencies and cost effectiveness consistent with the needs of military and commercial markets. The selection of the fuel is an important consideration for a portable power source. The ultimate

goal of this program is to be able to operate the TPV generator on a variety of fuels from natural gas to diesel. However, the goal for this initial phase was to use gaseous fuels to keep the focus of the effort on the main objective of demonstrating a high efficiency integrated TPV system.

2. TECHNICAL APPROACH

Thermophotovoltaics (TPV) is an energy conversion process where a primary energy source (chemical flame, solar energy, nuclear reactor, etc.) elevates a radiating structure to incandescent temperatures. The radiant energy (visible and infrared) is captured on an array of semiconductor photoconverters (e.g., solar cells) and converted directly into electrical power which is available at terminals on the array. The major components of a TPV power source are illustrated in Figure 2.1. These are: (1) a radiant emitter which is heated by the combustion of fuel, (2) an optical filter for recovering long wavelength photons, (3) a photovoltaic (PV) converter, and (4) a recuperator for the recovery of waste heat. In addition to the major components, there are also auxiliary components for fuel supply and storage, for delivery of combustion air and cooling air for PV array heat sink and filter, and for power conditioning. The key design issues are the efficiency and properties of the radiant emitter, the effectiveness of the optical filter for recuperation of sub-bandgap photons, the optimization of the photovoltaic converter performance, and the effectiveness of waste heat thermal recuperation.

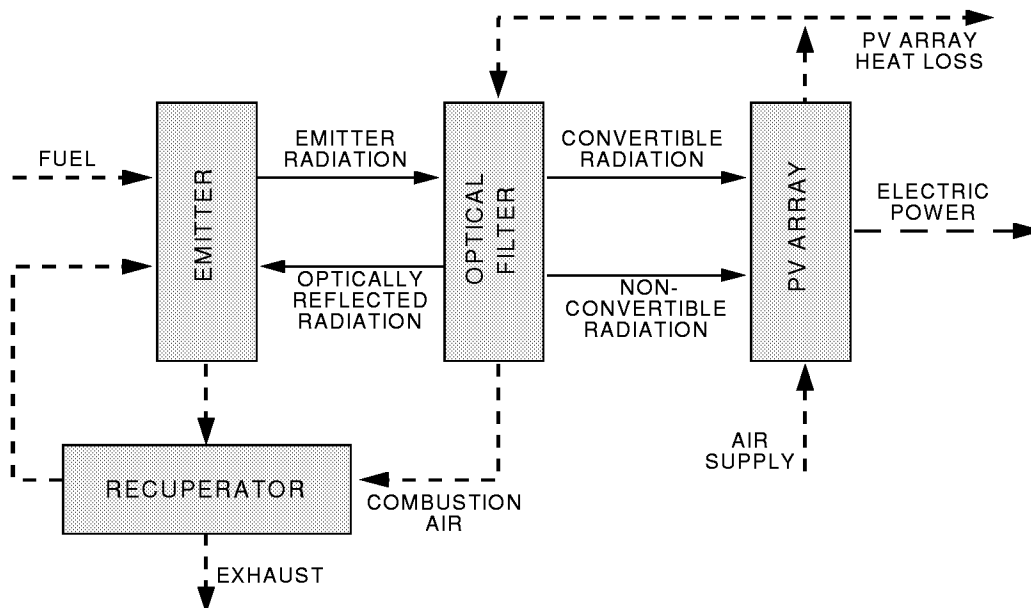


Figure 2.1 TPV Power Source Components

2.1 SELECTIVE VS. BROAD-BAND EMITTERS

All semiconductor photoconverters of conventional design convert radiant energy efficiently over a narrow optical bandwidth that is related physically to the energy gap of the semiconductor from which the photoconverter is fabricated. The spectral responsivity of a typical, high performance silicon photoconverter is shown in Figure 2.2. At wavelengths less than the absorption edge of silicon ($1.15\ \mu\text{m}$), a silicon device converts incident radiation into electrical power, with maximum cell responsivity (measured in amp/watt) at about $1\ \mu\text{m}$. With less energetic (longer wavelengths) photons, the silicon cell photoconverter is incapable of converting incoming radiation into electrical power because these long wavelength photons are unable to generate hole-electron pairs, which are necessary for power conversion. At wavelengths lower than $1\ \mu\text{m}$, the silicon's responsivity drops significantly because the incoming

photons have excessive energy for efficient conversion. This excessive photon energy is carried away as kinetic energy by the hole-electron pair, and is quickly lost by collisions with the silicon lattice, which subsequently rises in temperature. Thus potentially useful energy is lost in an irreversible manner that serves only to elevate the photoconverter's temperature and lowers its conversion efficiency.

Radiant structures, on the other hand, can produce broadband or wavelength-selective radiation. Broadband emitters produce higher radiant fluxes for a given operating temperature. However, much of the radiant energy is wasted unless a highly efficient optical filter is used between the emitter and the PV cell. A sufficiently effective filter, however, may be complex, expensive, and not operable in harsh, high temperature, combustion environments. Selective emitters, on the other hand, produce relatively large fractions of radiant output at wavelengths that are closely matched with the bandgap of the PV cell. These wavelengths produce the highest efficiencies and dissipate the least thermal energy in the optical filter, windows, and the PV cell (Ref. 1).

The selective emitters of most interest are compounds containing the rare-earth elements. These elements may be characterized as atoms with incomplete inner electron shells. Electronic transitions can occur among these vacancies, and energetically, these transitions occur at wavelengths in the near IR and visible portions of the optical spectrum. In addition, the outer valence electrons of the rare earth elements act like electrostatic shields which somewhat isolate the inner electrons from the effects of the external varying crystal fields. This shielding makes the rare earth ions behave like gaseous ions and emit line-spectra, rather than continuous spectra. This causes the selectivity of the rare-earth oxides, characterized by a single high emittance emission band with much lower emittance outside this band. The emission band of ytterbia, Yb_2O_3 , centered at 0.98 microns, matches amazingly well with the bandgap of silicon photovoltaic cells. Erbium, Er_2O_3 , exhibits a narrow band emission centered at 1.55 microns which makes it a suitable emitter for Ge or GaSb photoconverters. Holmium, Ho_2O_3 , has an emission peak centered at 2 microns which corresponds to III-V PV cells such as indium gallium arsenide. The ytterbia emission spectrum is plotted in Figure 2.2, along with the silicon cell efficiency, as a function of wavelength. A 2000 K, gray (or black) body spectral emission is also plotted to demonstrate the large amount of nonconvertible emission from the broadband emission source. Similar curves for an erbium emitter and gallium antimonide cell are plotted in Figure 2.3.

2.2 SYSTEMS ANALYSIS

Two system analysis models were developed during the program. The first is a simplified TPV systems analysis model which is used mainly for comparing various approaches on a consistent basis. This model and the results obtained from it are described in this section of the report. The second is a detailed model for a single module TPV system of the specific geometry and configuration of the systems under development. It is a much more accurate model for predicting the performance of the TPV systems under development and comparing it to the test results. The predictions can readily be extended to multiple module systems. This second systems analysis model and the results obtained from it are presented in Chapter 6.

The simplified TPV systems analysis model was prepared for the purpose of comparing the combinations of PV cells and emitters shown in Figures 2.2 and 2.3 (silicon/blackbody, silicon/ytterbia, gallium antimonide/blackbody, and gallium antimonide/erbium). The model breaks the wavelength spectrum into bandwidths of 10 nm from 400 to 5000 nm and 100 nm from 5000 to 50,000 nm. The characteristics of the PV cells and emitters, as a function of wavelength, were curve fit and entered into the model in equation form. The emitter radiative output, PV cell efficiency and electric power output were then calculated at each wavelength interval and summed over the spectrum from 400 to 50,000 nm. The model then calculated the key parameters for the main components using the thermophysical properties of air, fuel, and combustion products. The efficiency of the TPV system was then calculated for various values of optical recovery efficiency (fraction of out-of-band radiative energy recovered), recuperator effectiveness, emitter to PV array view factor, array cell packing factor, and electrical circuitry loss factor.

For the PV cell and emitter combinations that were examined, the specific electric power output (W/cm^2) and TPV system efficiency always increased with increasing emitter temperature over the range from 1700 K to 2000 K. The system efficiency also increases for higher values of optical recovery and recuperator efficiencies, whereas the specific electric power output is basically a function of the emitter temperature only, for a particular emitter type, when the view factor and array factors are fixed.

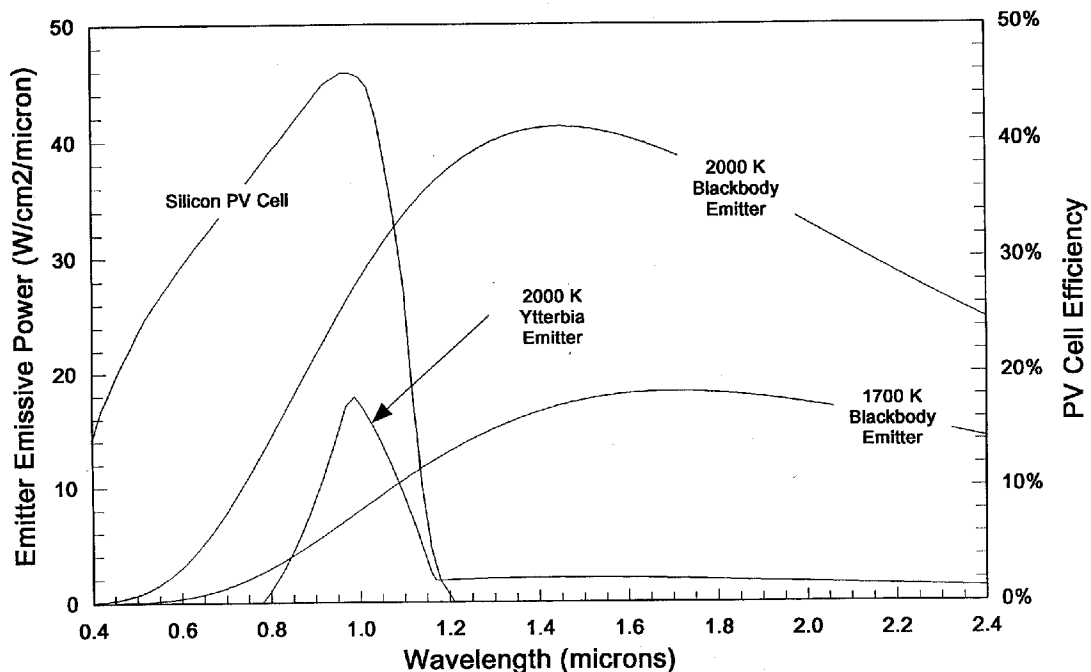


Figure 2.2 Ytterbia Emissive Power and Silicon PV Cell Efficiency

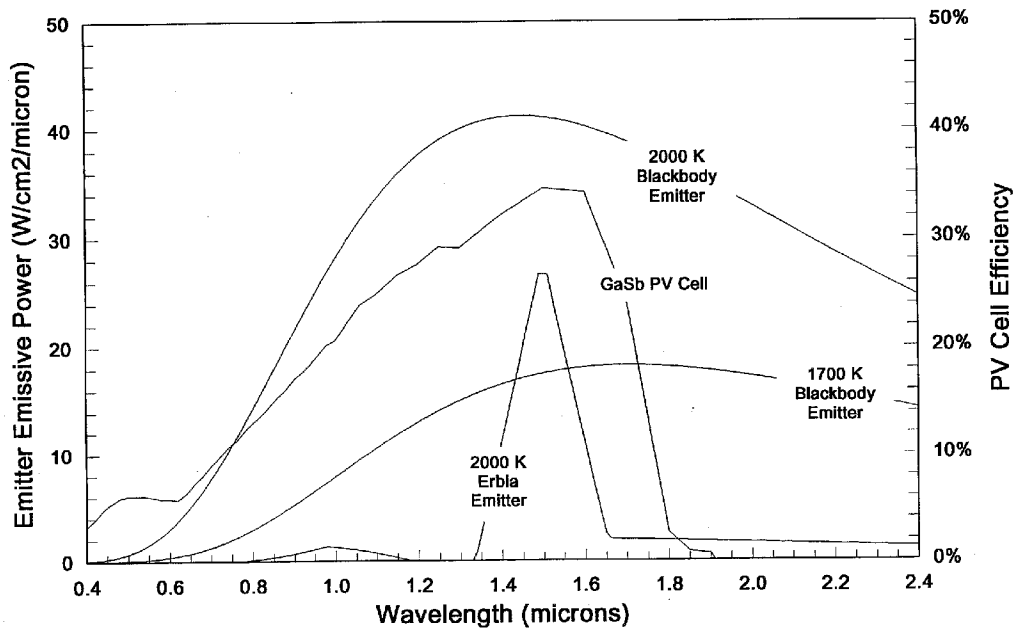


Figure 2.3 Erbia Emissive Power and Gallium Antimonide PV Cell Efficiency

The results of this analysis are shown in Table 2.1 for the six cases that are illustrated in Figures 2.2 and 2.3. For all cases, the recuperator efficiency was set at a readily attainable value of 80%. The optical recovery factor was set at 75% for the blackbody cases, but was reduced to 25% for the selective emitter cases (ytterbia and erbia) because the characteristics of selective emitters make it more difficult to recover as high a fraction of the off-band energy due to low absorptivity in the off-band region.

The TPV system efficiency is highest (10.13%) for the silicon/ytterbia combination at 2000 K, followed by gallium antimonide/erbium at 2000 K (9.06%), gallium antimonide/blackbody at 2000 K (8.80%), and gallium antimonide/blackbody at 1700 K (8.15%). Use of a blackbody emitter with silicon PV cells results in much lower TPV system efficiencies than with the selective ytterbia emitter and, as a result, the use of a blackbody emitter with silicon cells is not a good approach.

As would be expected, the specific electric power output with gallium antimonide cells is much higher with a blackbody emitter (6.02 W/cm^2 at 2000 K and 2.25 W/cm^2 at 1700 K) than with the selective erbia emitter, but this also brings with it a substantial heat removal problem at the PV array (40.97 W/cm^2 and 18.26 W/cm^2 respectively). The specific electric power output for the silicon/ytterbia combination (1.07 W/cm^2) is a bit higher than for the gallium antimonide/erbium combination (0.97 W/cm^2) at 2000 K. The heat removal load at the PV array is also much lower for the selective emitter cases (6.21 W/cm^2 for silicon/ytterbia and 6.37 W/cm^2 for gallium antimonide/erbium) than for the blackbody emitter cases studied.

Table 2.1 Comparison of Selected Emitter and PV Cell Combinations

PV Cell Type	Silicon			Gallium Antimonide		
Emitter Type	Black Body	Black Body	Ytterbia	Black Body	Black Body	Erbia
Emitter Temperature (K)	1700	2000	2000	1700	2000	2000
PV Cell Efficiency (%)	36.5	35.5	38.7	27.0	25.8	30.4
Optical Recovery Efficiency (%)	75	75	25	75	75	25
Recuperator Effectiveness (%)	80	80	80	80	80	80
Specific Electric Power (W/cm²)	0.60	2.41	1.07	2.25	6.02	0.97
PV Array Heat Load (W/cm²)	12.78	26.63	6.21	18.26	40.97	6.37
Exhaust Loss (W/cm²)	4.65	13.23	3.32	7.12	21.40	3.34
Fuel Heat Input (W/cm²)	18.03	42.26	10.60	27.64	68.38	10.69
TPV System Efficiency (%)	3.35	5.69	10.13	8.15	8.80	9.06

The technical approach taken in this project, based on the above analysis, was to use a wavelength selective fibrous emitter (ytterbia) radiating to a bandgap matched (silicon) photovoltaic array to minimize thermal and optical recuperation requirements, as well as nonrecoverable heat losses. While a well matched emitter-photoconverter has significant design advantages, high PV cell efficiency and high optical and thermal recuperation is critical for high system performance. It is also important that other potential loss mechanisms such as photoconverter fill factor, radiation view factor, ancillary power requirements and nonrecoverable thermal losses from optical windows and insulating surfaces be minimized.

3. SYSTEM DESIGN

The ytterbia emitter system chosen for this program is based on Thermo Power's patented supported continuous fiber radiant structure (SCFRS) that can operate up to temperatures of 2200 K with good thermal shock resistance and rapid response time. The emitter, shown schematically in Figure 3.1, consists of continuous fibers woven into a porous ceramic base. As such, the emitter preserves the advantages of gas light mantles that have traditionally operated at high temperatures for long times. Unlike gas mantles, the Thermo Power emitter can be made in planar, 15 cm x 15 cm or larger tiles without becoming fragile.

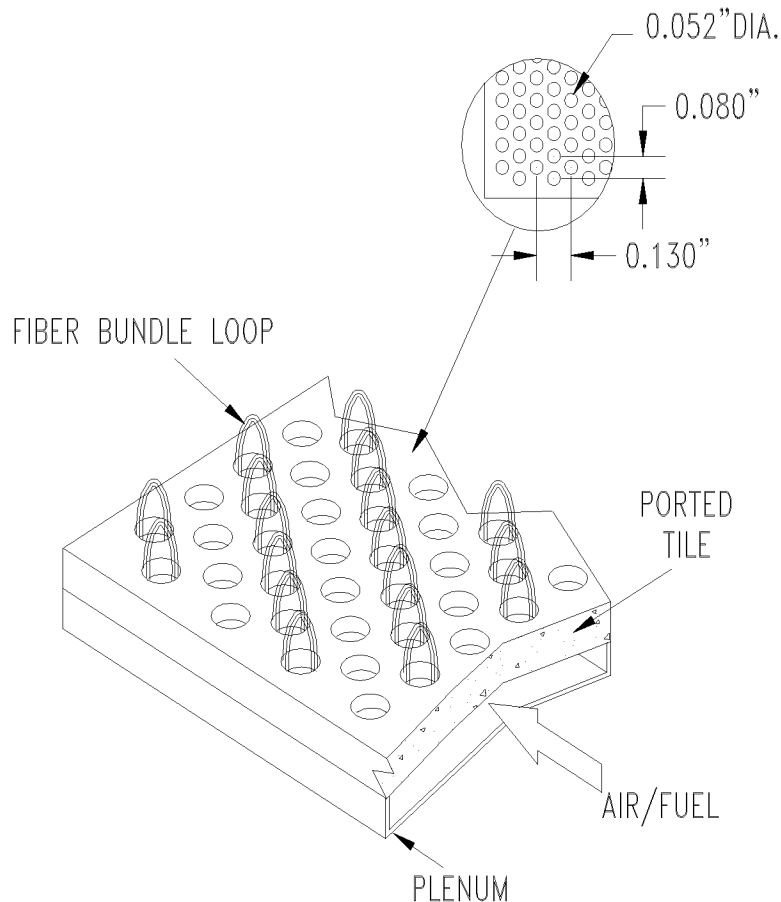


Figure 3.1 Supported Continuous Fiber Radiant Structure

The combustion air flows through the open pores in the ceramic substrate which supports the ytterbia emitter in fibrous form. Since the combustion air is preheated to much above the auto-ignition temperature of the fuel, fuel has to be mixed with the air and combusted in close proximity of the fibers just above the surface of the substrate. This requirement is one of the most challenging aspects of the generator design, since it has implications for the temperature uniformity of the fibers and off-band radiation leaving the emitter. Several design approaches for mixing fuel and preheated air were analyzed and bench tested to determine the feasibility of obtaining stable combustion and uniform temperature distribution of the fibrous radiating surface. The two most promising approaches are shown schematically in Figures 3.2 and 3.3.

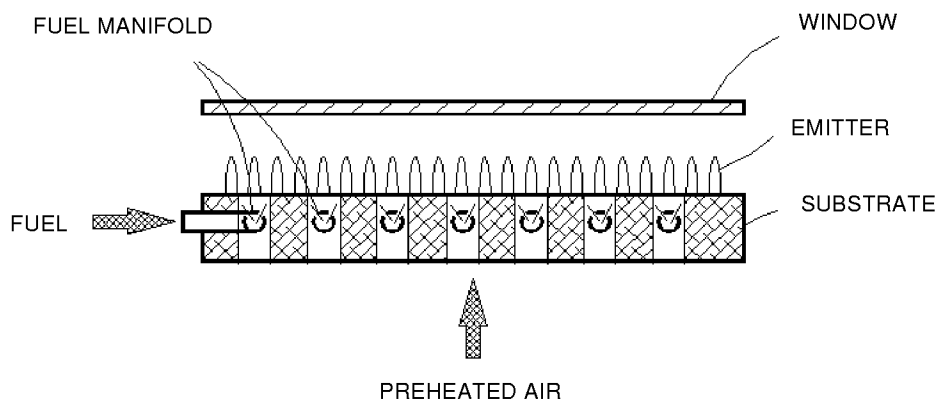


Figure 3.2 Micromixing Approach - Option A

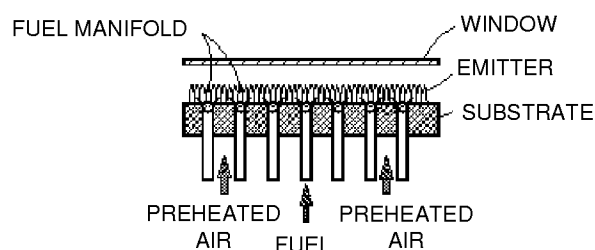


Figure 3.3 Micromixing Approach - Option B

In the first approach, Option A, fuel tubes are located in the air passages within the substrate just below the surface and fuel is injected from orifices in the fuel tubes to mix with preheated air. Option B achieves the same goal with a different fuel tube configuration which requires a considerably larger number of fuel tubes. In both approaches, fuel is delivered from the fuel plenum through fuel tubes to very near the surface of the substrate and mixed with the preheated air. The objective in both cases is to achieve rapid air-fuel mixing to complete combustion within the fiber bed for good fuel efficiency. Also, a sufficient number of orifices (in Option A) and fuel tubes (in Option B) are used to provide uniformity of temperature distribution.

Two configurations of TPV power converters based on these approaches were designed, fabricated, and tested. In designing these systems, we established a module size based on the availability of critical component parts like ceramic emitter substrate, ceramic core for the recuperator, and the base material for optical filter (quartz). This was done for both cost and delivery reasons. When these criteria were applied, the active emitter area on a single substrate was limited to about 12 cm x 12 cm, the face area of the recuperator to 15 cm x 15 cm, and the maximum filter size to 15.25 cm x 15.25 cm. Assuming the dimensions of the PV array to be the same as the active emitter area, the gross power output of a single module was determined to be in the range of 100 to 125 watts.

The schematic of a two-module TPV converter of Configuration A is shown in Figure 3.4.

In this configuration, a single emitter/photovoltaic array is close-coupled to a ceramic recuperator. This arrangement provides a compact design and can be scaled-up for higher power output by adding more modules. In the Configuration B TPV converter, shown in Figure 3.5, two emitters are coupled to a single very high effectiveness recuperator. This arrangement provides easier access and more space in the rear of the emitter substrate for fuel delivery system and is the preferred configuration, especially for liquid fuels. In operation, the combustion products pass through the ceramic recuperator to preheat the combustion air to about 1350 K. The combustion air flows through the back of the porous ceramic substrate which supports the ytterbia emitter in a filament form. As described earlier, since the preheated air temperature is far in excess of the auto-ignition temperature of the fuel, and in order to minimize the temperature of the substrate, the fuel is micromixed with the air just above the substrate surface. This enables the ytterbia filaments to see the maximum gas temperature and associated radiative output potential. To protect the PV array from direct contact of hot combustion gases and to reflect any nonconvertible radiation back to the emitter, two quartz windows with optical filters are used. Cooling air passes between the two windows to maintain them at temperatures consistent with the capability of the optical coatings.

The design specifications for the two module engineering prototype generator to be developed during this phase of the program and for an advanced prototype generator are presented in Table 3.1. The current prototype generator is designed to operate at an emitter temperature of 2000 K and an air preheat temperature of 1350 K. These temperatures were selected based on our operating experience with fibrous ytterbia emitters and the temperature capabilities of materials readily available for fabrication of the ceramic recuperator. A detailed computer model of the prototype TPV system has also shown that the power density and efficiency of the system continues to increase as these temperatures are increased when an efficient optical filter is used. For the advanced prototype, the emitter temperature will be increased to 2100 K and the air preheat temperature will be increased to 1650 K. This will require the use of a higher temperature ceramic material for the recuperator.

The planar emitters and PV arrays in the prototype system are essentially equal in area and square in shape. With a total emitter/PV array area of 290 cm^2 (for two modules), the Phase I prototype is designed to produce a gross power of 245 watts at a gross efficiency of 6.5%. The net power and efficiency are 170 watts and 4.5% respectively, after allowing power for the ancillary equipment. With the same total emitter/PV array area, the advanced prototype with higher temperature capability will be able of producing a gross power of 372 watts at a gross efficiency of 8.8%. The net power and efficiency will be 315 watts and 7.5% respectively, after allowing power for the ancillary equipment.

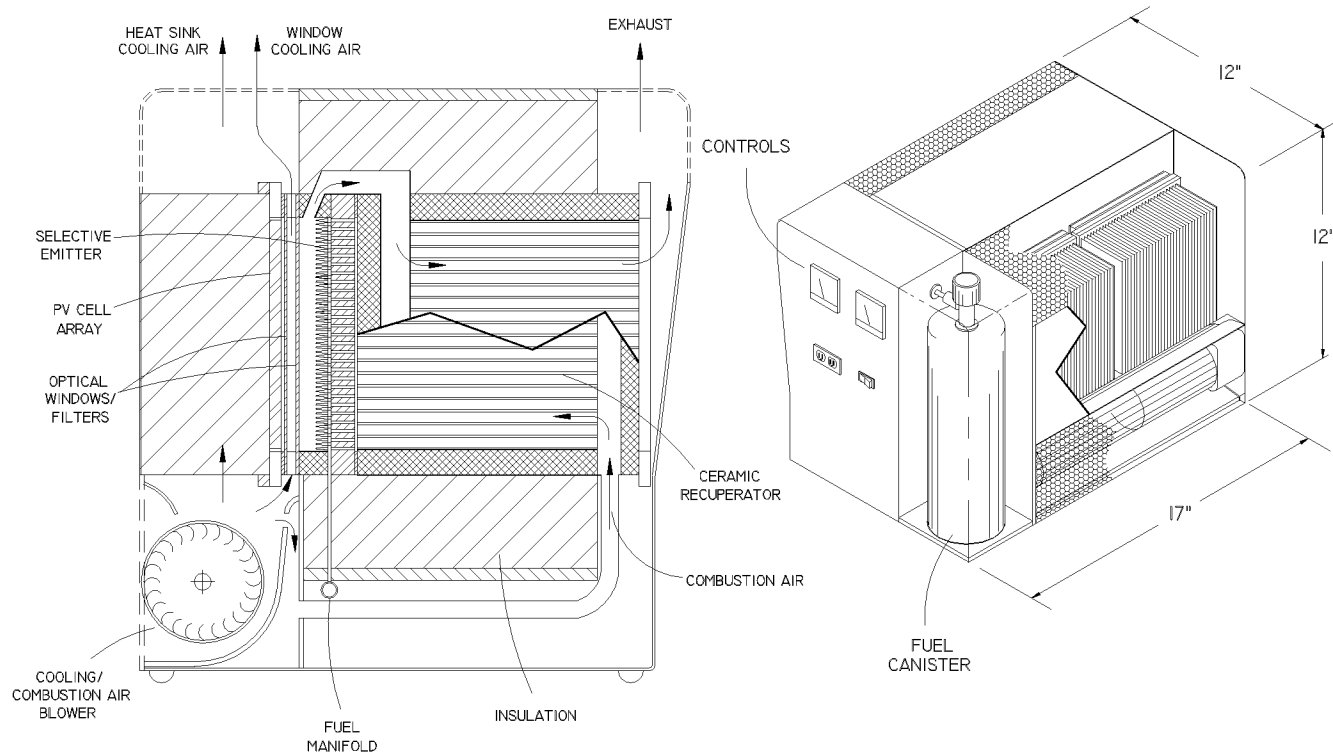


Figure 3.4 Configuration A, Two-Module, TPV Converter Schematic

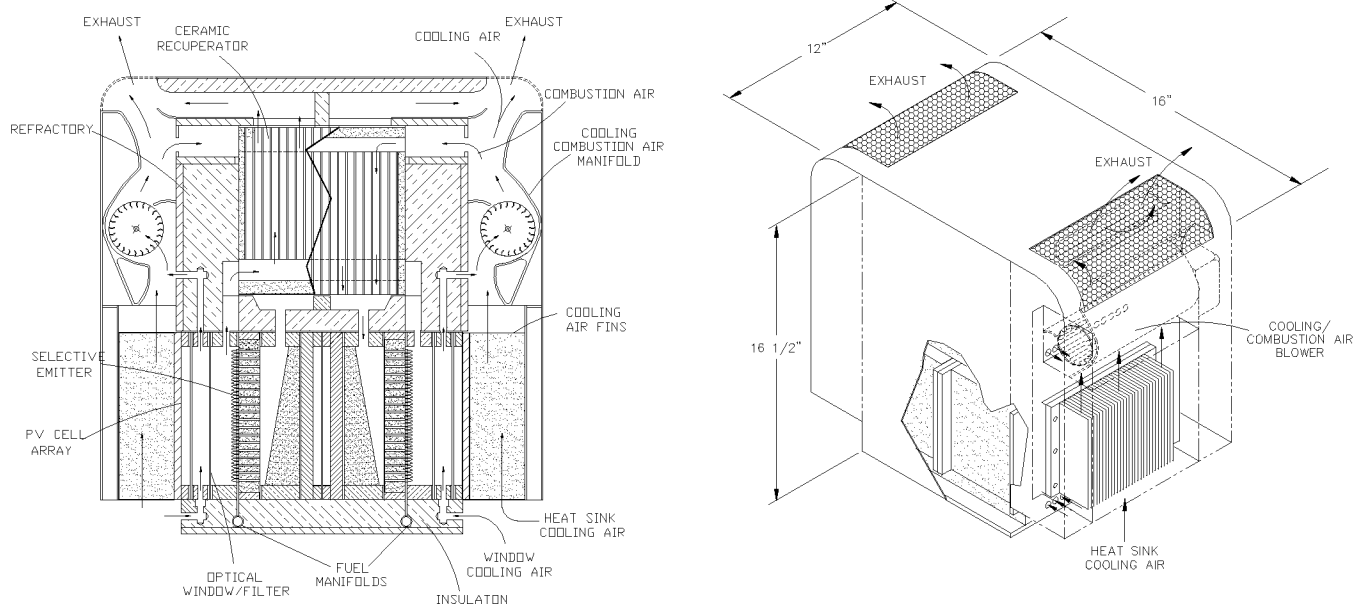


Figure 3.5 Configuration B, Two-Module, TPV Converter Schematic

Table 3.1 TPV Prototype Design Specifications

	Phase I Prototype	Advanced Prototype
Emitter Temperature – K	2000	2100
Air Preheat Temperature – K	1350	1650
Average Emitter Exitance – W/cm ²	3.50	5.00
Average Exitance View Factor	0.80	0.80
Average Exitance @ Array – W/cm ²	2.80	4.00
Emitter Area (2 Emitters) – cm ²	291	291
PV Array Area – cm ²	288	288
PV Cell Efficiency	38%	38%
PV Array Uniformity Factor	80%	85%
Gross Power (2 Emitters) – W	245	372
Ancillary Power – W	75	57
Net Power – W	170	315
Gross System Efficiency	6.5%	8.8%
Net System Efficiency	4.5%	7.5%

4. COMPONENTS DEVELOPMENT

To characterize the emitter system and to facilitate development of the optical filter, PV cell and the heat sink, a 1/4 scale “pathfinder” emitter system, shown schematically in Figure 4.1, was designed and fabricated. The photograph of the “pathfinder” system with its control panel and a preheater capable of heating the air-fuel mixture to 800 K is presented in Figure 4.2. The emitter structure used in this system is the supported continuous fiber system depicted in Figure 3.1, where the emitter is attached to a plenum that provides the air/fuel premix. It employs a monolithic ceramic support that is chosen for mechanical strength and not for optical properties or thermal stress considerations. The support material used for this system was a cordierite ported tile (Hamilton Porcelain #242), normally used for radiant burners. During operation, the air/fuel premix flows through the open pores in the substrate and burns above the substrate with the flame front located within the ytterbia fibers. This emitter delivers a high level of uniform silicon convertible exitance in planar form.

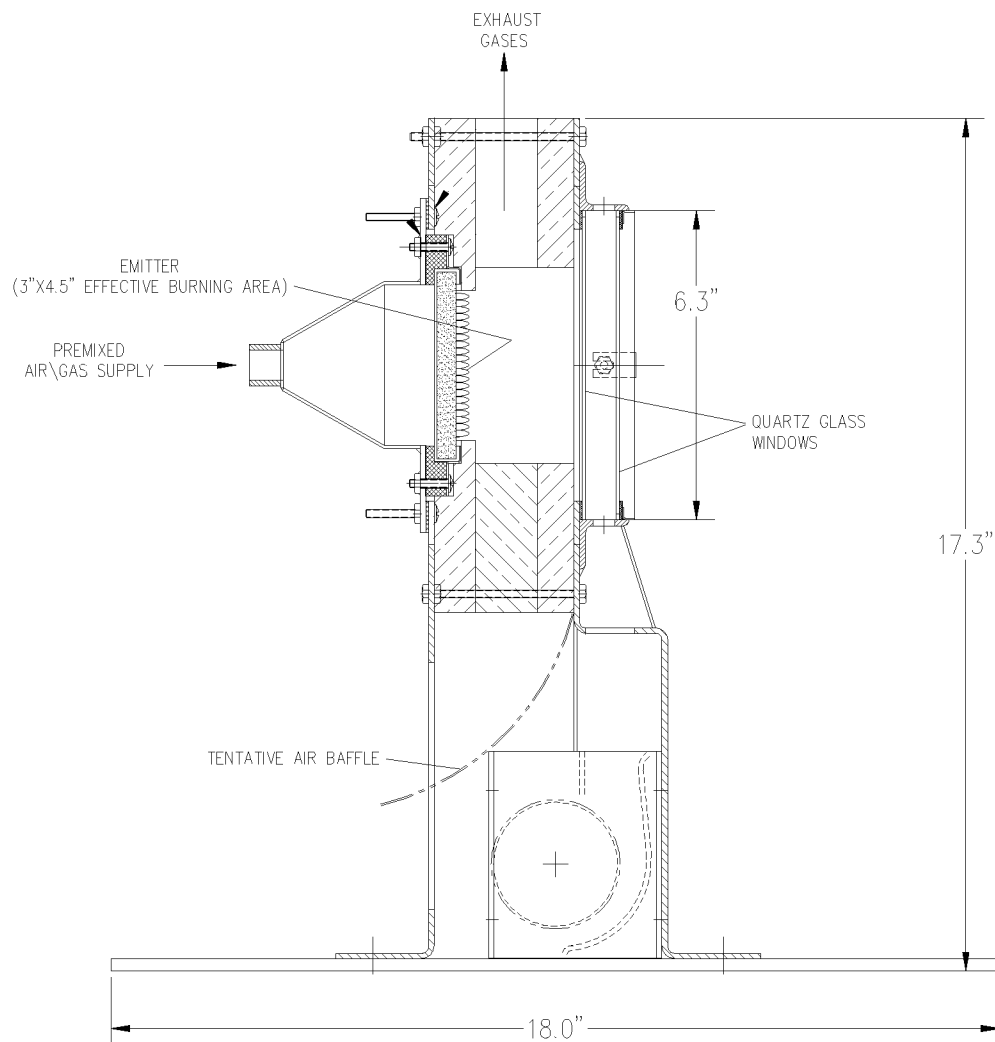


Figure 4.1 "Pathfinder" Emitter System

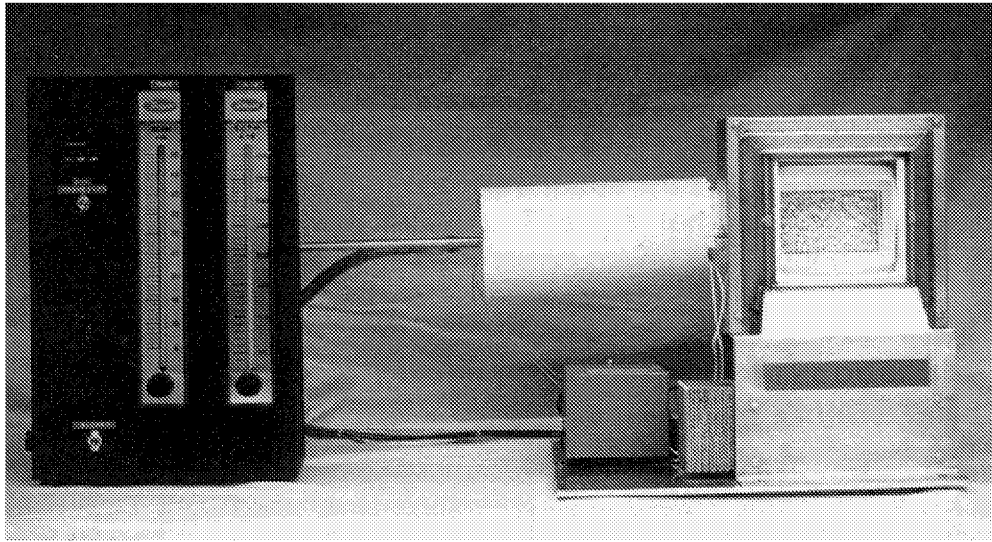


Figure 4.2 “Pathfinder” Emitter System with Control Panel

4.1 EMITTER DEVELOPMENT

The fibrous emitter structures were fabricated by a cellulose support process that is based on textile precursors. Continuous filament rayon yarn, impregnated with ytterbium nitrate salt solution, were tufted into the porous ceramic support much like a rug making process that yielded an uncut loop pile. After tufting, the treated rayon was converted into a ceramic by means of a controlled heat treatment process. At low temperatures and with a controlled gas ambient, the nitrate salt in the rayon was converted into the oxide. The heat treatment was continued at higher temperatures which pyrolyzed the rayon until an oxide skeleton remained which has the morphology of the textile structure, but with greatly reduced dimensions. A final high temperature sintering step was used to further densify and strengthen the ceramic filaments. After sintering, the ytterbia fibers were bonded to the plenum side of the substrate with alumina cement. The same alumina cement was used to plug some of the remaining ports in a regular fashion to adjust emitter porosity for combustion stability. A peripheral border around the active emitter area was also sealed off with alumina cement to prevent leakage when the assembly was attached to the plenum.

A number of different types of emitters were designed, fabricated, and tested. The variations included two substrate types, three overall fiber densities (half, single and double), three emitter sizes (7.6 cm x 7.6 cm, 7.6 cm x 11.4 cm, and 12 cm x 12 cm), and two fiber lengths. The two substrates differed in port size, number of ports per unit area, and porosity. The substrate used for earlier emitters, designed for premix operation in the pathfinder, had a port size of 0.052” and the other substrate designed for micromix operation in the engineering prototypes of both Configurations A and B had a port size of 0.100”. The larger port size allows use of 1/16" O.D. fuel tubes to be located within the ports while still leaving enough space for air to flow around it, as required for the micromix operation shown in Figures 3.2 and 3.3. This substrate, however, has fewer ports requiring more fibers per port to provide the same overall fiber density.

The characterization of the pathfinder emitter was done by Essential Research Inc. The following measurements were made: spectrally resolved emitter power density from 0.7 to 3.0 μm , total power density over all wavelengths, temperature measurements of the two quartz windows, and false-color

images of the Pathfinder emitter using a CCD IR camera. In addition, new measurement techniques were used to calculate the temperature of emitter fibers and the long-IR power density.

4.1.1 Total Power Density Measurements

Total power measurements were made of a single-density emitter behind two quartz windows. The test setup is shown schematically in Figure 4.3. The detector (power meter) is a pyroelectric radiometer with a circular aperture of 0.5 cm^2 . The detector's field-of-view is limited to just the emitter surface by a 1.27-cm (0.5-in.) or 3.81-cm (1.5-in.), diameter aperture placed between the emitter and the detector. For the 3.81-cm diameter aperture, the maximum area viewed by the detector is a 6.1-cm diameter circle centered on the emitter. For the 1.27-cm diameter aperture the viewed area is 4.8 cm in diameter. View factor was calculated based on a geometry of two parallel, concentric disks, one being the detector opening and the other being the aperture. This view factor is valid as long as the detector can only "see" emitter surface through the aperture and none of the surrounding insulation. Table 4.1 lists the measurement parameters.

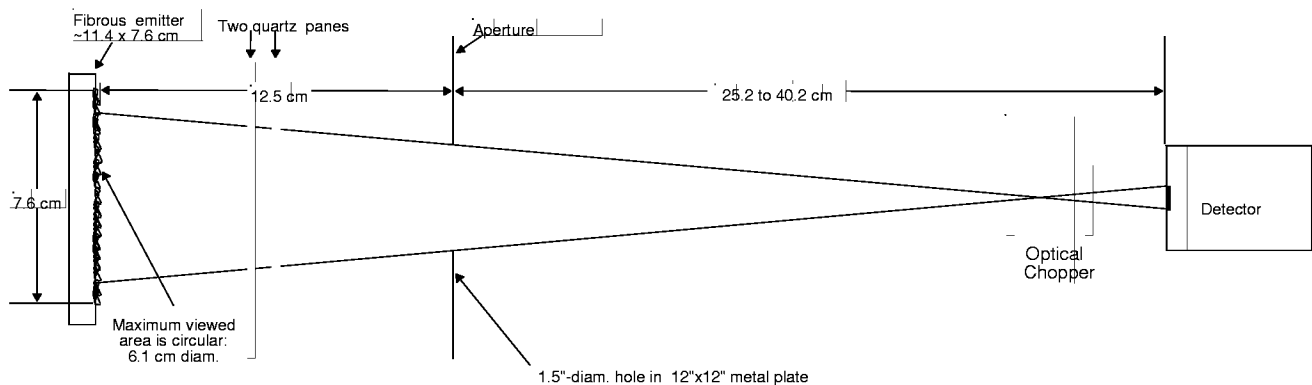


Figure 4.3a Geometry for Power Density Measurements Using a 1.5" Diameter Aperture

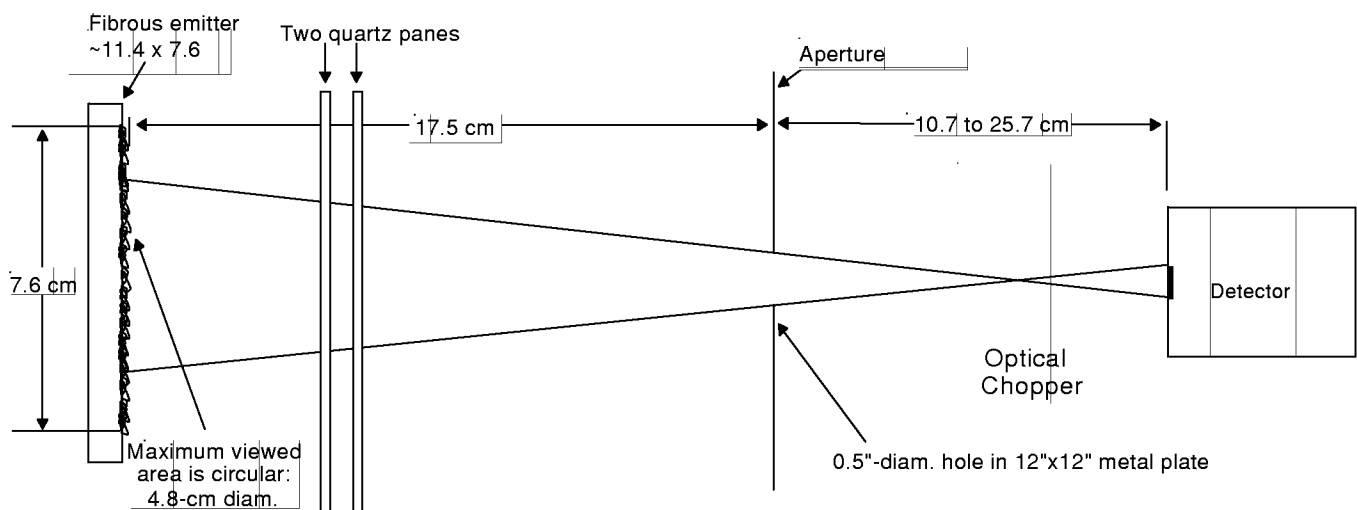


Figure 4.3b Geometry for Power Density Measurements Using a 0.5" Diameter Aperture

**Table 4.1 Total Radiative Power Density of a Single-Density Emitter
Viewed Through Two Quartz Windows**

Aperture Diameter	Detector Diameter	Aperture-to-Detector Distance	Measured Power (W/cm ²) (x 10 ⁻³)	View Factor (x 10 ⁻³)	Power Density at Emitter Surface (W/cm ²)
(cm)	(cm)	(cm)			
3.81 ↓	0.798 ↓	25.2	60.6	5.68	10.67
		30.2	42.9	3.96	10.83
		35.2	31.7	2.92	10.86
		40.2	24.5	2.24	10.94
1.27 ↓	0.798 ↓	10.7	37.9	3.50	10.81
		15.7	17.6	1.63	10.76
		20.7	10.2	0.940	10.85
		25.7	7.06	.610	11.57
					Average: 10.9

In general, the measurements are very consistent and show that the power density of a single density emitter, as viewed through two quartz windows, has an average value of 10.9 W/cm². For each aperture, there is a slight trend for increased power density with increasing aperture-to-detector distance. This can be attributed to nonuniformity in the emitter surface.

4.1.2 Spectrally Resolved Emitter Power

Spectrally resolved power density measurements of the emitter were made by Essential Research Inc. with a spectral radiometer that made use of a dual-grating monochromator and three detectors: silicon and germanium operating in the photovoltaic mode and a lead sulfide detector operating in the photoresistive mode. With these detectors, a wavelength range from 680 to 3100 nm can be measured with a spectral resolution of 10 nm from 700 to 1300 nm and 40 nm from 1300 to 3100 nm. Figure 4.4 shows the exitance vs. wavelength of a single-density emitter as viewed through two quartz windows. The power density values represent the power at the emitter surface and passing through the two quartz windows. The peak emitter output is at 980 nm. The PV silicon cell can convert radiation up to approximately 1180 nm. If the spectrum is integrated from 680 to 1180 nm, the power is 3.24 W/cm². This is the power available to the silicon PV cell for electrical conversion. If one takes into account the transmission losses for the two windows (~ 6.6% loss per window), the emitter surface is generating 3.71 W/cm² of silicon convertible energy. If the spectrum in Figure 4.4 is integrated over the entire range of 680 to 3100 nm, the power is 8.40 W/cm². Both the total power density measurements and the spectrally resolved measurements were made under similar emitter operating conditions. The difference between the total power measurement (10.9 W/cm²) and the integrated spectral measurement (8.40 W/cm²) is 2.50 W/cm². The majority of this 2.5 W/cm² is presumably at IR wavelengths beyond 3100 nm. Some of that energy, from 3100 to 3500 nm, is coming from the emitter. The rest of it comes from the hot quartz windows.

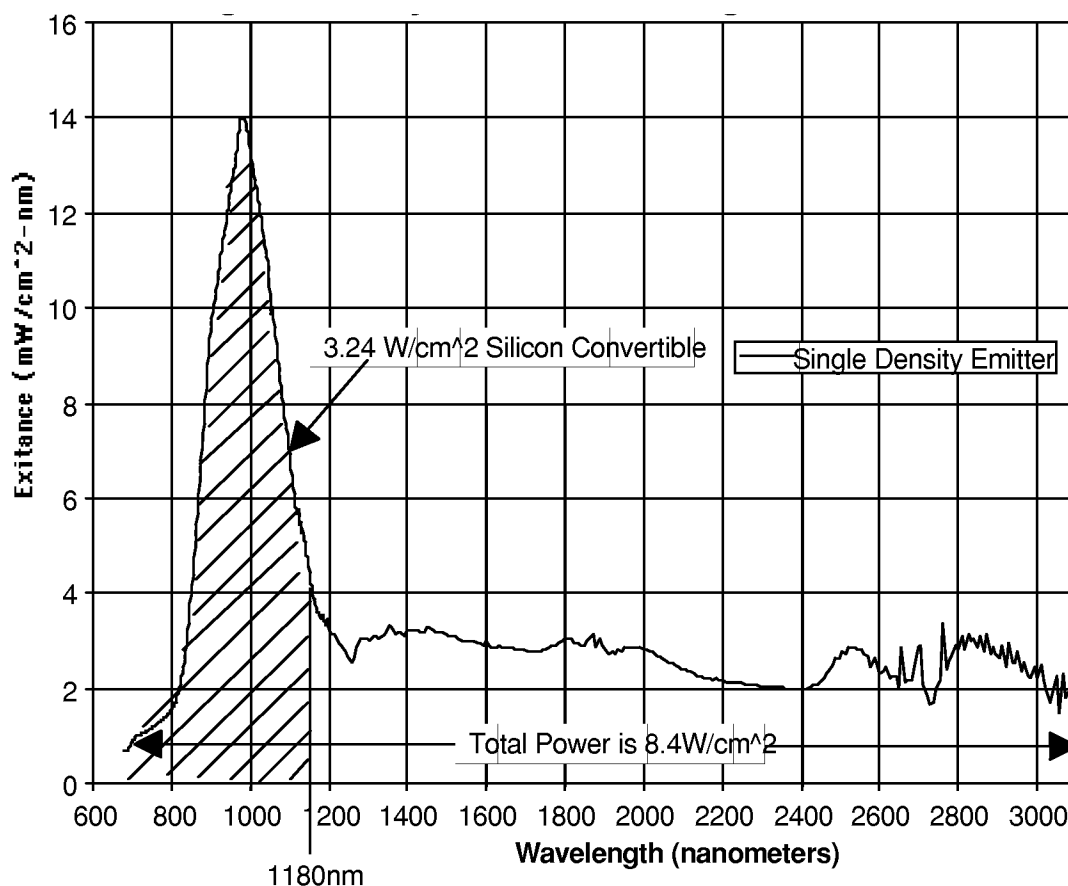


Figure 4.4 Spectral Exitance of an Emitter Viewed Through Two Quartz Windows

4.1.3 Long Wavelength Characterization of the Pathfinder Emitter

The previous section described spectral characterization from 700 to 3100 nm. For a complete picture, the spectral content and power levels beyond 3100 nm are needed to properly design filters and emitters. Essential Research Inc. has developed a method to measure the IR emitter power in four wavelength “blocks”: from 1.8 to 3.5, 3.5 to 6, 6 to 9, and 9 to ~24 μm . This is an adequate resolution to characterize the IR portion of the emitter spectrum.

Figure 4.5 shows the transmission properties of various window materials. If total power measurements are made with and without a sapphire window, the spectra can be corrected for the reflection losses of the sapphire and differenced to obtain the spectral power from 6 μm to longer wavelengths. (Six microns is the cut-off wavelength of sapphire, which is defined as the wavelength where transmission falls below 50%.)

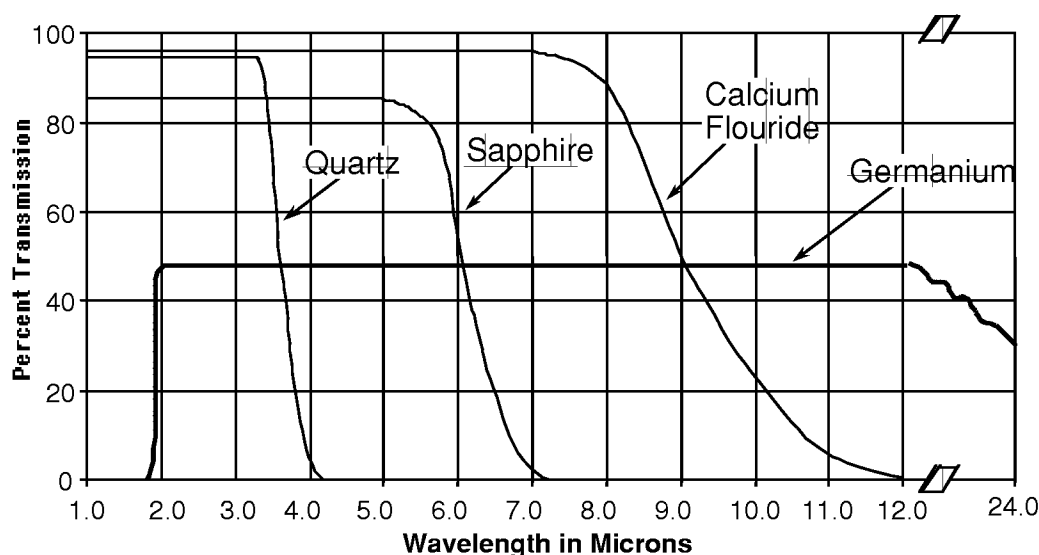


Figure 4.5 Percent Transmission of Various IR Window Materials

Continuing this methodology a spectrum measured with a quartz window (cut-off wavelength 3.5 μm) can be corrected for reflection loss and subtracted from the one taken with sapphire window to obtain the power between 3.5 and 6 μm . By adding CaF_2 and Ge to the list, the four wavelength blocks mentioned above are obtained as illustrated in Figure 4.6. A Perkin-Elmer I-19 spectrophotometer and a Nicolet FTIR were used to measure the cut-off wavelengths and reflection losses for each of the window materials. Using the same operating conditions, a series of measurements using the various window materials were made. The results are summarized in Table 4.2. Since these measurements were made with two quartz windows in front of the emitter, it is likely that all of the radiation beyond 4 μm is coming from the quartz windows themselves and not the emitter surface.

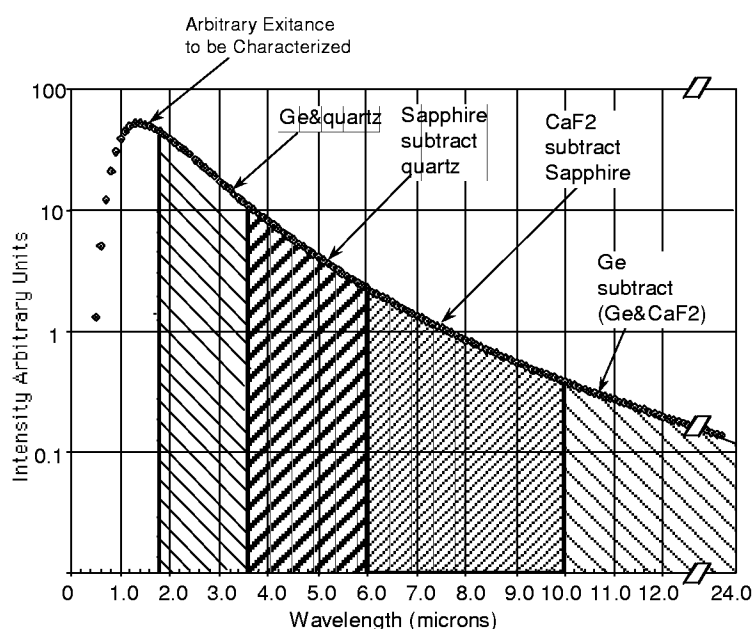


Figure 4.6 Spectral Ranges Characterized Using Various Window Materials

**Table 4.2 IR Content of an Emitter Viewed Through
Two Quartz Windows**

Spectral Range (microns)	Power Density (W/cm ²)
0.2-1.85	4.6
1.85-4	4.80
4-6	1.26
6-9	0.01
9-24	0
Total: 10.67	

4.1.4 Temperature Measurement of Ytterbia Fibers

One of the most important design parameters of the emitter is the ytterbia fiber temperature. Since the fibers are very thin, it is difficult to get a direct temperature measurement of the fiber by attaching a thermocouple (TC). The approach so far has been to position the thermocouple in the vicinity of the fibers and assume that the combustion gases are heating up the TC to the same temperature as the fibers. By making a correction for TC diameter, the fiber temperature is estimated. This is not an ideal method for many reasons, the most practical one being that it is difficult to maintain the position of the TC junction in the flame front. Essential Research Inc. developed a temperature measuring technique that uses both TC measurements and optical pyrometry to better measure the fiber temperature.

The governing equation for the radiation emitted by the fiber is given by a modified version of Planck's blackbody function:

$$E = \frac{\epsilon C_1 \lambda^{-5}}{\exp(C_2 / \lambda T) - 1} \quad (1)$$

Where λ is wavelength, E is the radiation emitted by the fibers at wavelength λ and temperature T, ϵ is the emissivity at wavelength λ , T is temperature in Kelvin, and C_1 and C_2 are known constants. If E can be measured at a given wavelength at two different temperatures (T_0 and T_1), it can be shown that:

$$T_1 = \frac{-\Delta T k + \sqrt{(k \Delta T)^2 + 4k \Delta T}}{2k} \quad (2)$$

where,

$$k = \frac{\lambda}{C_2} \ln \left(\frac{E_0}{E_1} \right) \quad (3)$$

$$\text{and,} \quad T_0 - T_1 = \Delta T \quad (4)$$

Once T is known, emissivity can be calculated from (1).

Although the exact temperature given by a thermocouple near the flame front is not very reliable, the difference between two flame temperature readings should accurately reflect the change in fiber temperature, ΔT . The only other assumption made is that ϵ remains constant over the temperature range. By choosing wavelengths near the emissive peak, the radiation is assumed to be coming solely from the fibers and not the substrate.

Using this method, emitter power was measured at two different temperatures over a wavelength range of 900 to 1200 nm (see Figure 4.7). The two thermocouple readings were 1688 and 1598°C. Using these data, the fiber temperature was calculated to be 2093 ± 50 K. Using this temperature, the emissivity from 900 to 1200 nm was calculated and is depicted in Figure 4.8.

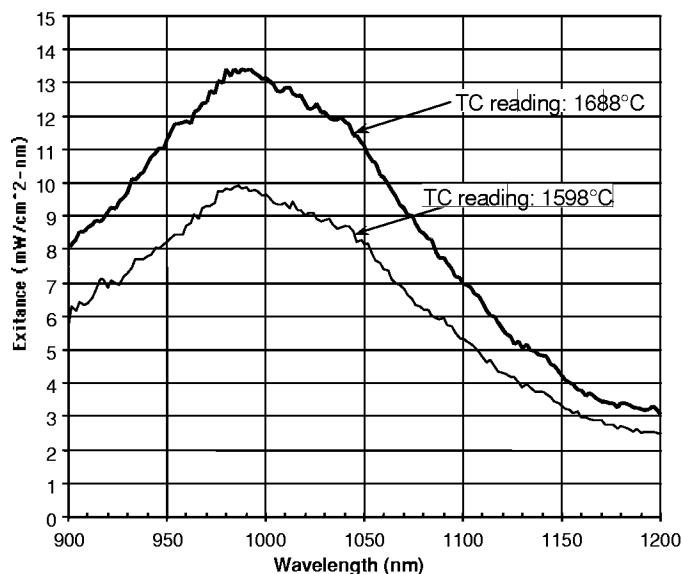


Figure 4.7 Exitance of an Emitter at Two Different Temperatures

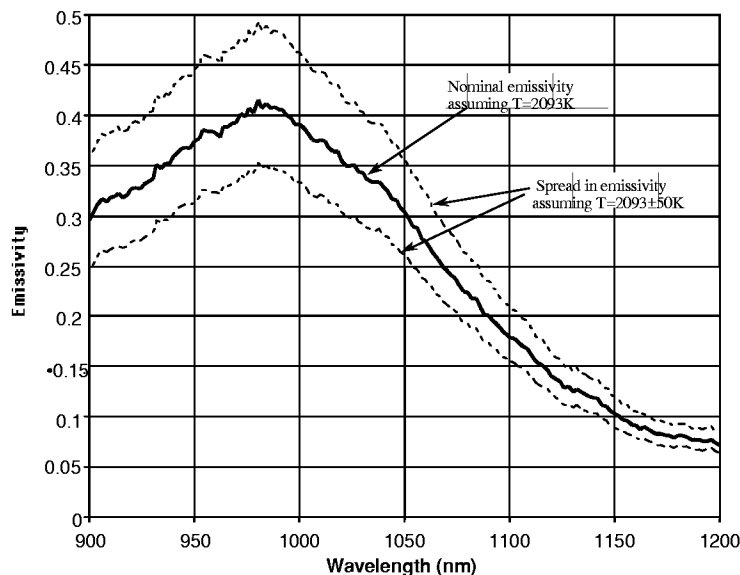


Figure 4.8 Emissivity of a Single-Density Emitter at a Temperature of 2093 K

4.1.5 Radiation Distribution at PV Cell Plane

The temperature at the emitter fibers and the radiant exitance (W/cm^2) from the emitter fibers was shown to be fairly uniform through the measurements made by Essential Research. Uniform exitance at the emitter, however, does not result in uniform radiation at the PV cell plane. A simple view factor model was used initially to determine the magnitude of the non-uniformity of the radiation at the PV cell plane. Later measurements were made using the individual cells in the PV array to measure the non-uniformity and compare it to the model.

View Factor Model

A prediction of the distribution of the radiation at the PV array plane was made by modeling the emitter and PV array as parallel, equal-area circular-disks separated and interconnected by insulated (refractory) walls and calculating the view factor (W/cm^2 @ array/ W/cm^2 @ emitter). The net radiation to the refractory walls is equal to zero and all the radiation arriving at the refractory walls is either reflected or absorbed and re-emitted. The refractory walls are also treated as diffuse with a cosine distribution of the reflected and re-emitter radiation. To assess the effect of the refractory walls, the predictions were also made assuming no interconnecting walls between the emitter and the array.

The results of these predictions are presented in Figure 4.9. The impact of the refractory walls is quite substantial. It raises the exitance at the center of the PV array from ~70% of that at the emitter to ~100%. It also raises the predicted average exitance over the entire PV array from 53% to 76%. The refractory walls also raise the predicted exitance near the edge of the PV array from ~38% to 53% of the emitter exitance.

View Factor Measurements

The responsivity characteristic of the PV cells in the array was used to measure the actual view factor at each cell location when the TPV system was in operation. This was done by individually measuring the short-circuit current of each of the PV cells in the array with the emitter operating at a steady-state condition. By assuming the responsivity (short-circuit current/incident radiation - A/W) of the individual cells to be the same, the incident radiation and the actual view factor at each PV cell location was determined. These results are shown in Figure 4.10. From these measurements, the average view factor was determined to be 80%.

A comparison of Figures 4.9 and 4.10 shows that:

- the refractory walls must be taken into account to accurately predict the view factors
- the measured average view factor (80%), is higher than predicted (76%)
- at 95% of the distance to the edge of the array, the measured local view factor (~70%) is much higher than predicted (~52%).

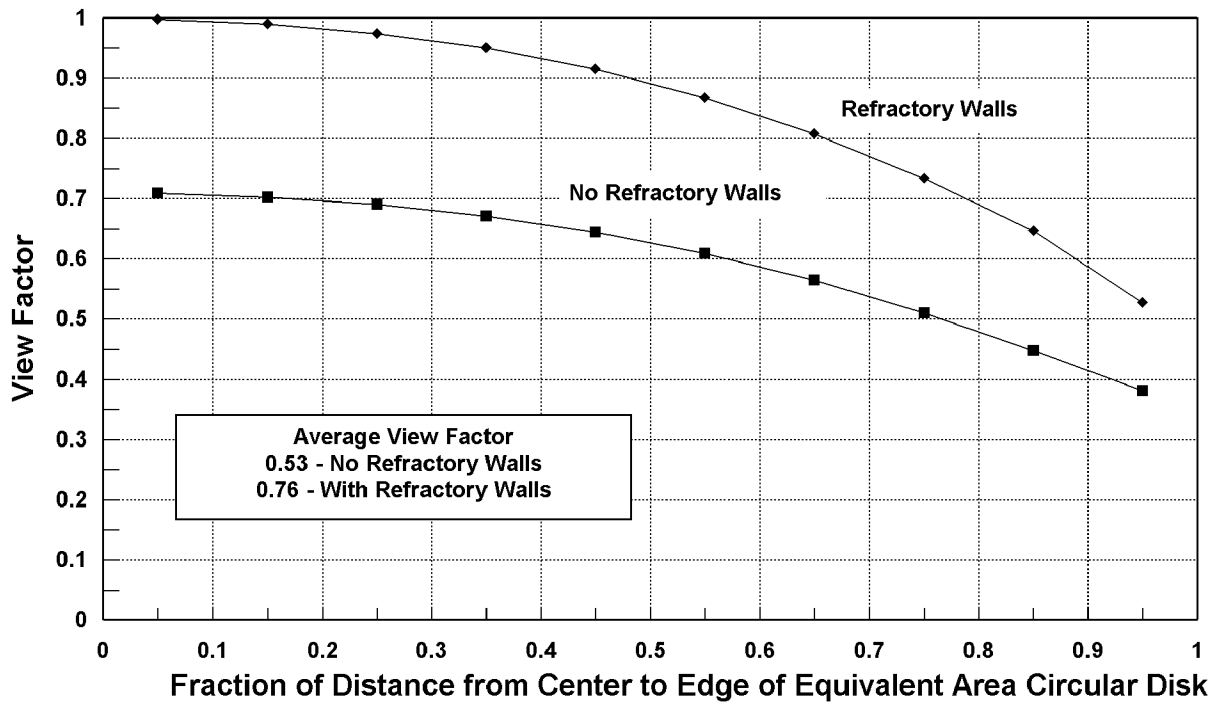


Figure 4.9 Predicted View Factor for Prototype TPV System – Emitter to PV Cell Plane

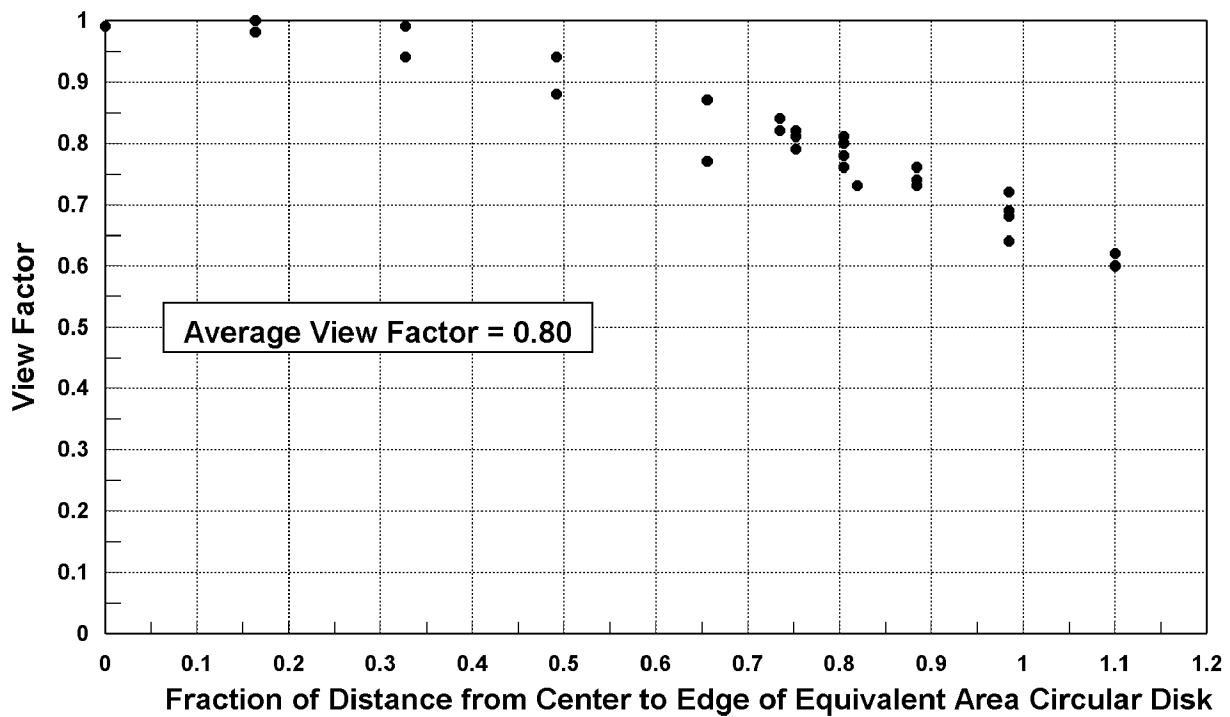


Figure 4.10 Measured View Factor for Prototype TPV System – Emitter to PV Cell Plane

4.2 OPTICAL FILTER DEVELOPMENT

Optical filters play an important role in any high-efficiency thermophotovoltaic (TPV) energy conversion system. Filters recycle radiation with energies less than the response of the TPV cells, reduce the heat load on TPV cells, and even recycle a portion of combustion exhaust gas heat. The requirements for optical filters in a TPV system are demanding. An ideal optical filter must have high transmission where the TPV cell responds, high reflectivity in the long-wavelength region beyond the cell response, and low absorption at all wavelengths. The high operating temperatures and large temperature gradients inside a TPV system make for extraordinary operating conditions that cause failure of both optical filter coatings and substrates. This section presents the optical development work carried out by Essential Research Inc.

The design of the optical filter is complicated by several system-level constraints. First, the system requires two windows (or filters) between the emitter and the TPV cells. The front window (the one closest to the emitter) keeps hot exhaust gases from impinging on the cells. This front window heats up to temperatures in excess of 850°C. A second window is needed to block radiative and convective heat transfer from the front window to the cells. In addition, cooling air must flow between the two windows to prevent the front window from exceeding the maximum service temperature of quartz (1000°C), and the second window from getting so hot as to require a third window. Since we know of no filter that can survive an operating temperature of 800°C, the filter must be located on the second window or on the TPV cell itself.

Another system consideration is how efficiently light reflected from the optical filter will be absorbed by the ytterbia fibers. Ytterbia fibers, by design, have very low emittance at long wavelengths and thus low absorption. Therefore, long wavelength radiation reflected back to the fibers will not be absorbed effectively by the fibers. The radiation will either be absorbed by the substrate holding the fibers, the alumina walls surrounding the fibers, or the window/filter combination. Also, view factor can greatly affect recycling efficiency. For example, if both the emitter-to-filter and filter-to-emitter view factors were 0.94, then the highest recycling efficiency can be no greater than the product of the two: 0.88.

Two types of filters were studied for their optical performance and mechanical stability in the Pathfinder emitter. One was a multilayer dielectric stack filter deposited on quartz and the other was a thin-film “transparent” conductive coating also known as a “solar control film” deposited on glass. These two technologies were chosen for both their potential high performance and low cost at production levels.

4.2.1 Dielectric Stack Filters

The dielectric stack filters are similar in design to production coatings used for tungsten-filament, quartz-envelope lamps. For lamp coatings, the dielectric filter is deposited on the outside of the quartz envelope and reflects wavelengths longer than the visible spectrum (>700 nm) back to the filament for recycling. The thermal stability of these coatings is well known; they are routinely tested for a 2000 hr operation at 650°C and show little degradation. For TPV, the lamp coating must be modified to match the longer wavelength response of the silicon cell (i.e., be transparent out to 1180 nm). By and large, the operating conditions, coating design, and production techniques are the same for the coating desired for TPV as the high volume lamp coating. The modification involved increasing the number of stacks and the total coating thickness to push the transmission edge out to 1180 nm. This modification produced the projected shift in transmission on the first try.

The dielectric stack filters, as received by Essential Research from the manufacturer, demonstrated a disappointing performance. In-band transmission was too low (only about 85%) and in-band absorption was nearly 10%, which was unacceptably high for use in a TPV system. More catastrophically, however, they failed in less than 20 min. when run in the Pathfinder system. Collaborating with the manufacturer, Essential Research identified a manufacturing defect that caused both the low in-band transmission and premature failure. The defect was a consequence of the film modification, but was corrected easily by annealing the filter at 550°C for 5 hours. This annealing schedule produced a uniform looking filter with hairline cracks (crazing) in the film and transmission better than that for the filter as received from the manufacturer. Figure 4.11 is a micrograph of the cracks taken at a magnification of 55X.

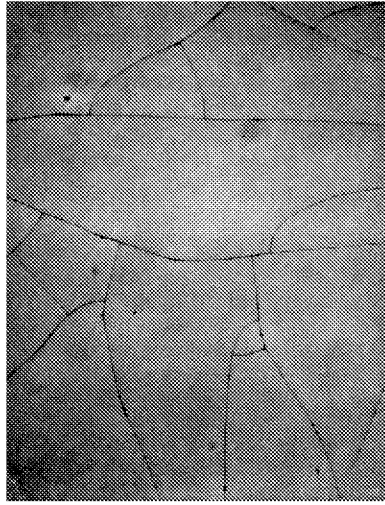


Figure 4.11 Micrograph Showing Crazing in a Dielectric Filter

The measured transmission and absorption improvement relative to the as-received filter, are illustrated in Figures 4.12 and 4.13. The corrected dielectric stack filter had an in-band transmission of ~95%, reflected radiation over the range of 1180 to 3200 nm, and survived the Pathfinder operating environment.

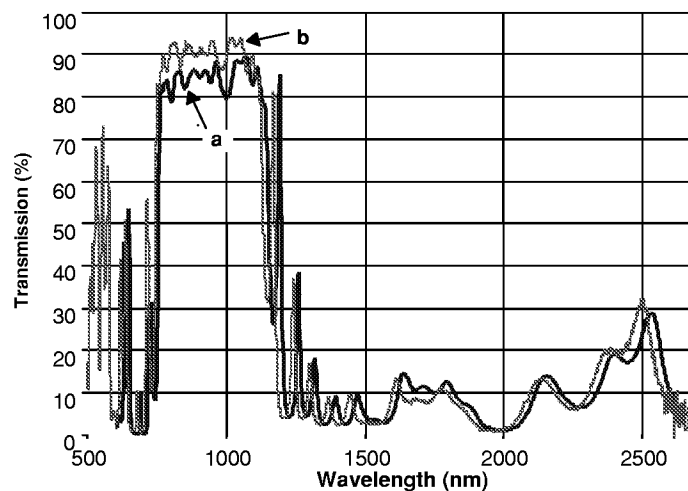


Figure 4.12 Transmission of Dielectric Filter
 a) As Received From the Manufacturer, and b) After Furnace Annealing

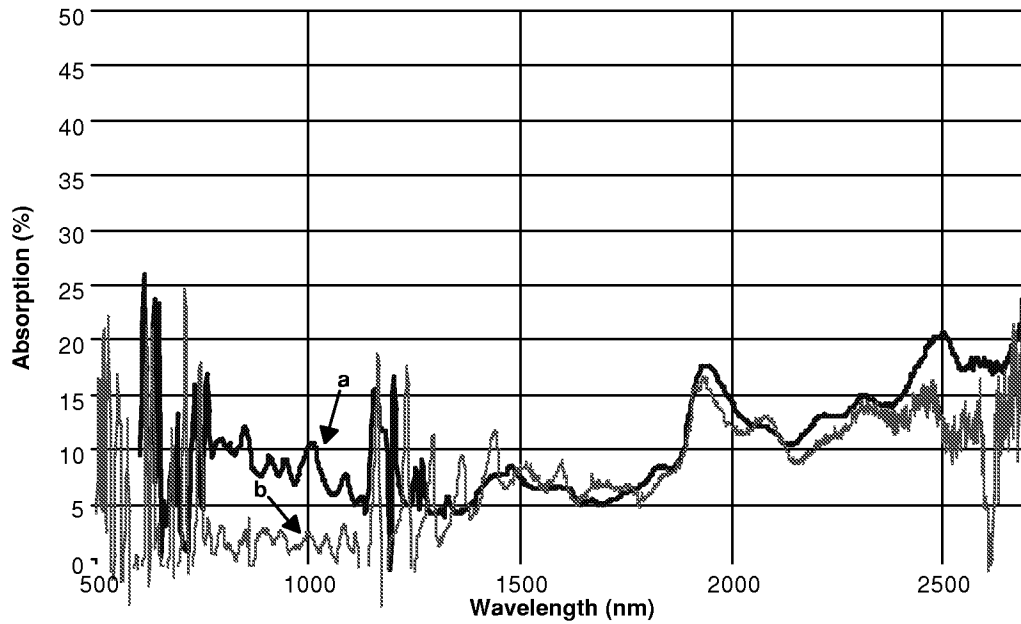


Figure 4.13 Absorption of a Dielectric Stack Filter
a) As Received From the Manufacturer, and b) After Furnace Annealing

The dielectric stack filter performance is shown in Figure 4.14 by comparing the spectral content of the power radiated for two operating conditions: two quartz windows, and the combination of one quartz window and a dielectric stack filter.

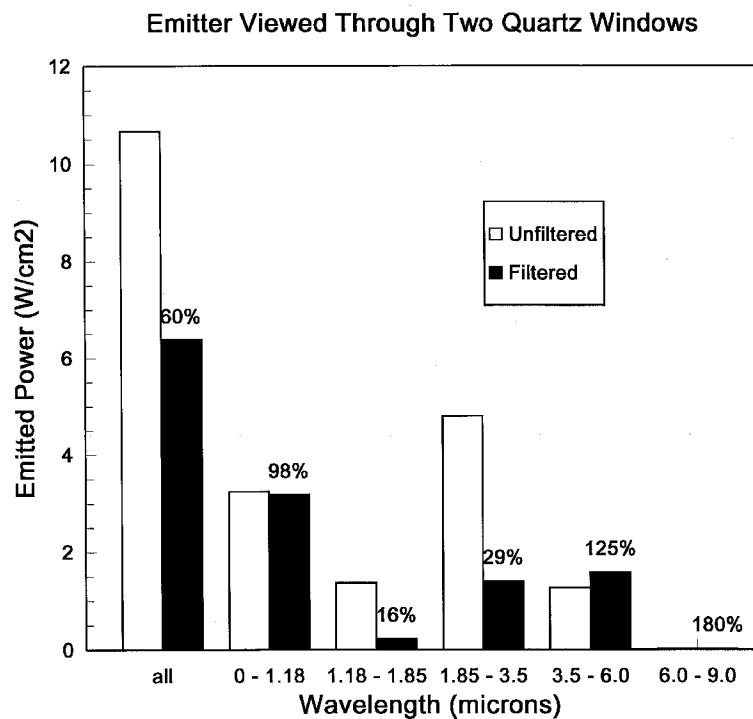


Figure 4.14 Dielectric Stack Filter Performance

The first two bars show the effect on total power: the dielectric stack reduced output power to 60% of the unfiltered output. The next two bars show that the silicon convertible radiation dropped by 2% with the use of a filter. In the near IR, the wavelength range between 1180 and 3500 nm, output power was reduced by a factor of four: just 24% of the unfiltered power level. With the use of a filter, the ratio of in-band to out-of-band radiation (convertible fraction) thus increased from 30% to 50%.

The experimental investigations revealed at least two recycling mechanisms. First, using quartz windows alone, heat is transferred from the hot front window to the emitter via thermal radiative coupling. In addition, when a dielectric stack filter is run in the second window position, reflected radiation is absorbed by either the emitter fibers or substrate and recycled.

4.2.2 Conductive Film Filters

Thin-film conductive coatings are commonly used as long-wavelength reflecting filters. Free electrons within the coating reflect light in the same manner as electrons in a metallic mirror. Long-wavelength radiation is more efficiently reflected by free electrons than shorter wavelengths. So, if the film has a very low electron population, only the longest wavelengths will be reflected; shorter wavelengths will pass through the film. By controlling the free-electron population (i.e. conductivity) in the film, the spectral characteristics of the filter can be controlled. The conductivity of the film is manipulated either by varying film thickness or the free-electron density. However, these films have two negative characteristics relative to dielectric stack filters: they have higher absorption of the transmitted light and the transition from reflection to transmission is not nearly as sharp.

Thin-film conductive coatings fall into two categories: thin metallic films ($<200 \text{ \AA}$) where conductivity is controlled by film thickness, or conductive oxides where both film thickness and free-electron density are controlled. An entire industry has developed around these types of coatings for architectural use. Conductive oxide coatings are used on windows to allow the majority of the sun's radiation into a building while reflecting the long-wavelength radiation. These coatings are inexpensive and widely manufactured. If effective for TPV use, they will add little additional cost to the system. For this study, thin-film indium-tin-oxide (ITO) coatings were evaluated as long-wavelength, out-of-band reflectors.

The transmission, reflection and absorption of the ITO film is shown in Figure 4.15. The transmission of in-band radiation is about 85% which is too low. More problematic is the absorption of out-of-band radiation which averages close to 20%. Also the transition from reflection to transmission is unacceptably long. The reflectance for wavelengths longer than 3500 nm, however, is nearly unity, as measured with an FTIR spectrometer.

Of the two types of filters evaluated, dielectric stack was chosen over thin film conductive coatings for use during this phase of the project, because of its higher in-band transmission, lower absorption and high reflectivity in the out-of-band region. However, a composite filter with dielectric stack on one side and an ITO film on the other may be a viable option for a future prototype. The transmission of the combination filter is shown in Figure 4.16. Compared to the dielectric stack, the composite filter has a higher reflection of the out-of-band radiation but a much lower transmission of in-band power.

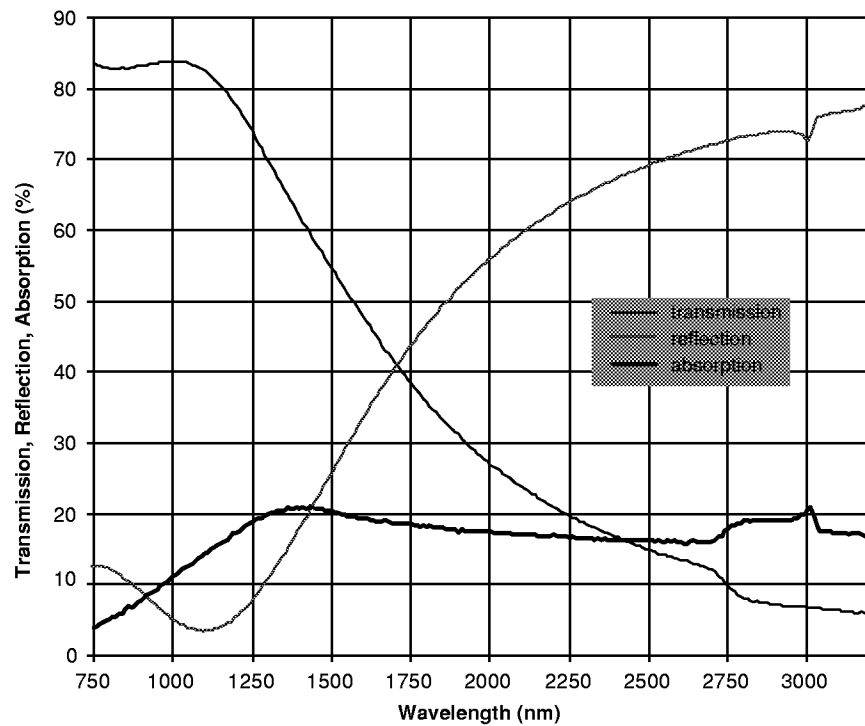


Figure 4.15 Transmission, Reflection and Absorption of an ITO Filter

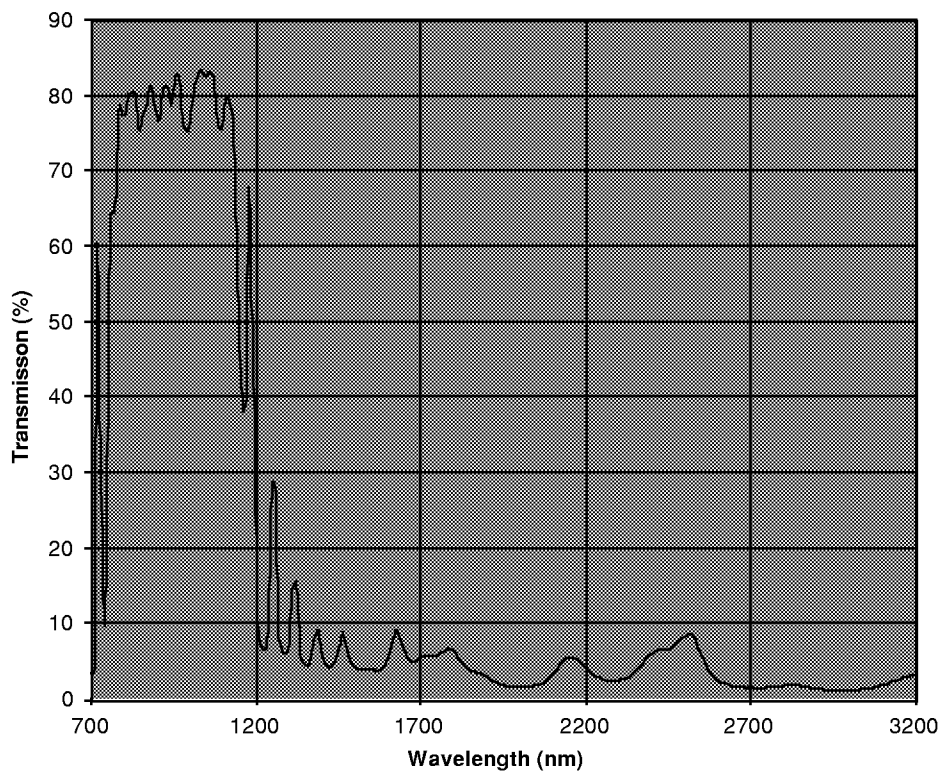


Figure 4.16 Model Transmission for a Composite Filter Composed of a Dielectric Stack and an ITO Thin Film

4.3 PV ARRAY AND HEAT SINK DEVELOPMENT

The development of the PV array and heat sink was done by TECSTAR INC., Applied Solar Division. The primary objective of TECSTAR's effort was to develop a silicon photocell whose performance was optimized for the operating characteristics of the ytterbia selective emitter being developed at Thermo Power. This requirement meant that the peak monochromatic efficiency of the photocell be about 45% and it should occur at or beyond (higher wavelength) the ytterbia emission peak at 980 nm. Shown in Figure 4.17 is the ytterbia emission spectrum and the spectral response curves for a good solar silicon cell and an optimized TPV silicon cell. The optimized cell is designed to provide higher current near the silicon bandgap edge and is therefore better matched to the emitter spectrum.

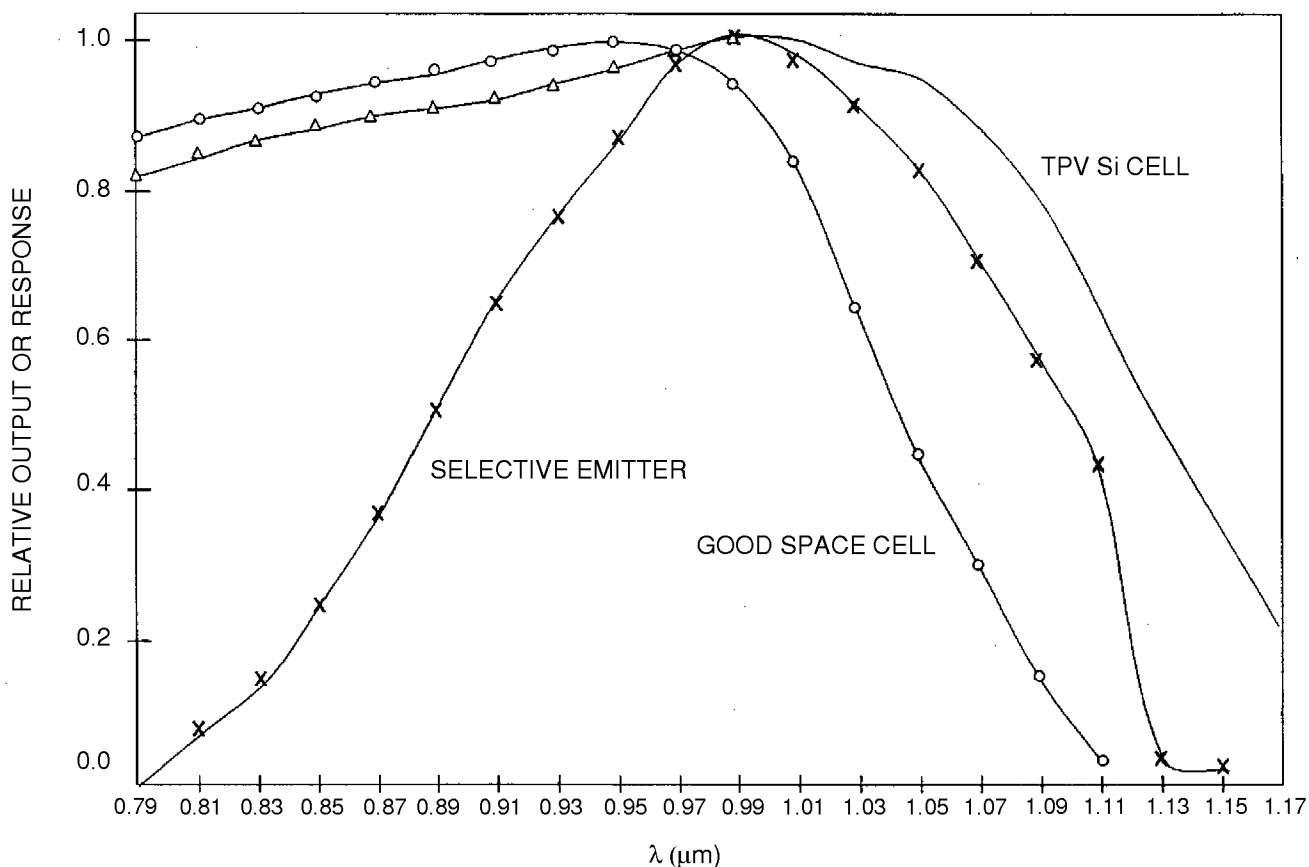


Figure 4.17 Response of Ytterbia Emitter and Silicon Cells

The baseline TPV silicon cell for this program was the Passivated Emitter Rear Locally (PERL) diffused solar cell depicted in Figure 4.18. The distinguishing feature of this cell is the localized diffusion points at the rear contact of the cell. To assist in the development of these high efficiency PERL cells, TECSTAR placed a subcontract with Unisearch LTD Consultants at the University of New South Wales for the design and manufacture of ~120 PERL cells and for transfer of the technology to TECSTAR. This group is experienced in the design and manufacture of high efficiency PERL cells and has previously demonstrated a monochromatic efficiency of 45%.

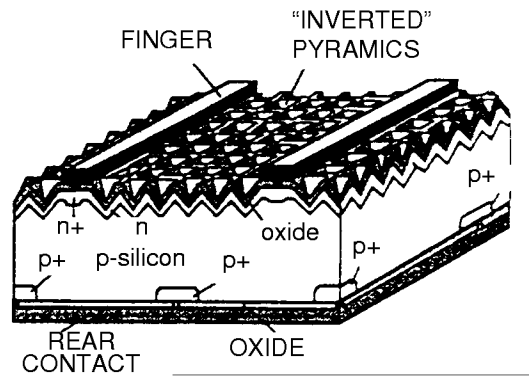


Figure 4.18 Baseline PERL Cell

The PV array consists of eleven (11) modules, each with three (3) cells. The PV array design specifications, which are provided in Table 4.3, were derived from the system definition that evolved early in the program.

Table 4.3 PV Array Design Specifications

	Specification
Si convertible input @ PV array	3.5 W/cm ²
Number of cells/module	3
Number of cells/array	33
Array electric power	167 W
Average cell power	5.1 W
Average cell open circuit voltage	800 mV
Average cell short circuit current	7.9 A
Average CFF	80%
In-band cell efficiency	36%

4.3.1 PV Cell Module Design

4.3.1.1 Overview

The photocell was designed for operation in the concentrated light of the emitter and has a surface area measuring four square centimeters (1 cm x 4 cm). The basic module assembly is formed by interconnecting and mounting cells onto a thermally conductive, electrically isolated base. Provisions in the base allow transport of heat away from the module via a water cooling circuit. The thermal management of the cell was designed to accommodate 20 W/cm². This is ~3 times the total radiation measured by Essential Research with the optical filter and was selected to provide a good safety margin and capability for future power increases. The selection of the proper substrate in mounting configuration was the subject of a detailed design trade study. Proper selection of the substrate topology was especially important given the high radiant flux of the emitter.

The design of the interconnected cell topology is constrained by the close spacing required for maximum energy transfer density. The back surfaces of the series connected cells must be bonded to an intermediate insulating surface to provide electrical isolation while maintaining a low thermal impedance path to the cooling system. Electrical insulators such as Al₂O₃, AlN, very thin SiO₂, and Kapton were considered to provide the optimal compromise between electrical and thermal characteristics. The reduction in solar absorption is accomplished by reflecting as much as possible of the incident selective emitter energy at wavelengths outside the response band of the cell. This results in lower operating temperature and higher cell performance.

A thermal shutdown module is needed to provide over-temperature protection for the module assembly in the event that coolant supply is interrupted during the operation of the TPV system. The thermal shutdown is comprised of a module mounted thermocouple connected to a digital temperature monitor. The temperature monitor has a programmable temperature alarm that provides a fuel shutoff signal to the emitter assembly.

4.3.1.2 Subsystem Design Trades

Given the guiding requirements of density, modularity, and performance, the following design constraints were established: 1) the module assembly must provide interface and environmental control for the PV cells, 2) the module assembly is essentially a heat sink that transports sufficient heat flux in order to maintain cell temperatures within operational limits, and 3) the cells must be electrically isolated in order to facilitate series interconnections.

Module Configuration

The module configuration is driven by the need for high packing-factor, effective thermal management, and reliable operation. It was the intent of the design team to produce a design that allowed validation of full-scale technology attributes that would be part of a viable production system, while allowing flexibility needed for effective laboratory evaluation.

The determination of the area of the emitters drove the active area of the array to be 132 cm². The conductive rear surface of the cell meant that high electrical isolation between cells would be necessary.

Given that the module would have to maintain isolation while sinking a heat flux density of 20 W/cm^2 , high thermal conductivity would be an essential element of any design approach.

The shingled cell configuration offers the highest packing factor but has limited flexibility. The shingled cells must have intimate contact with the heat sink and maintain good electrical contact with adjacent cells. The temperature gradient between the cells and the heat sink would result in excessive stress. Compounding the inherent nonuniformity of thermal characteristics is that the contact of the cell cantilevered over the adjacent cell would not be in contact with the heat sink. The shingled cell configuration does not lend itself to reworking. Modification of cell interconnection schemes could not be achieved with this approach. Given the need for flexibility due to the unknown effective view factor and spatial uniformity, this approach was deemed unacceptable. This approach does however represent a viable option for a mature system.

Unlike the shingled approach, the planar configuration offers a multitude of options to provide cell-to-cell isolation. The isolation interface is the easiest to achieve at the cell interface due to the mechanics inherent in the water cooled system. The planar configuration perhaps provided one of the most desirable features of the design in that the series/parallel circuit configurations are not limited. An independent interconnection scheme provided that ability to accommodate the nonuniform emission and nonideal view factor effects of the emitter. This feature was highly beneficial given that the degree of nonuniformity could not be assessed until system integration.

Cell to Heat Sink Bonding

Several cell-to-heat sink interface methods were considered in the design phase. The candidate schemes are composed of various combinations of insulating and adhesive type materials such as epoxy, Kapton, and aluminum oxide. A performance index was calculated for each approach based upon the sum of the thermal resistance of layers between the cell and the aluminum heat sink. A depiction of each approach and the associated resistance stack is provided in Figure 4.19. A description of four of the configurations follows:

Configuration 1

Kapton was at first considered the most viable insulating medium, however, an application using Kapton would still require other compounds to provide adhesion. As such, a cell soldered onto a copper-on-Kapton film that is bonded onto an aluminum heat sink with acrylic adhesive, or an autoclave process, was determined a viable application of Kapton. The performance index assigned to this configuration was quite good, however, the process was cumbersome and expensive. Additionally, the risk of cell breakage at soldering is high because of the large difference in thermal expansion between the cells and the aluminum heat sink.

Configuration 2

This approach provides the highest performance index of all configurations examined. This configuration was initially selected as the baseline, but was later rejected because of the inability to ensure that electrical isolation is maintained over the operational environment. Although the epoxy chosen was electrically nonconductive, the presence of pin holes or contaminants could lead to shorting.

Configuration 3

This approach consists of a cell bonded onto a Kapton layer that is bonded onto a bare aluminum heat sink. The performance index was low because of the stacking of thermal resistance in the epoxy and Kapton layers.

Configuration 4

The performance index of this configuration is 94% of the early baseline approach and has additional provisions to ensure isolation between the cell and heat sink. The aluminum heat sink is anodized (approximately .002" thick) to protect from electrical shorting while providing good thermal conduction. Electrically conductive epoxy was considered for this configuration but was ultimately not selected due to electrical continuity tests indicating a potential for isolation breakdown at an imperfection in the anodized layer. Nonelectrically conductive epoxy added extra electrical isolation with only a minor addition to the net thermal resistance.

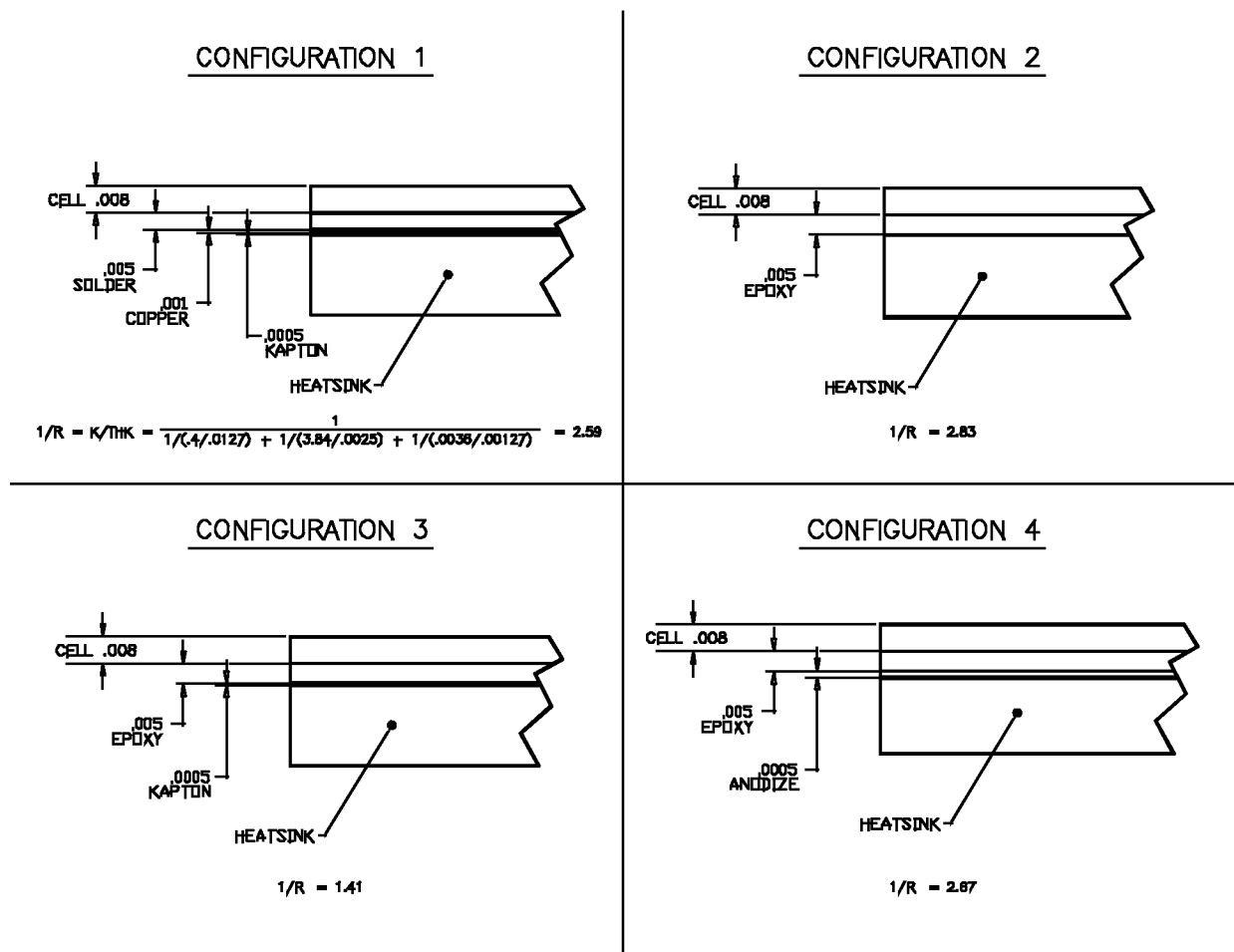


Figure 4.19 Cell to Heat Sink Interface Options

Other configurations examined early in the program include several bolted techniques. Cells were individually soldered onto small aluminum bases and then bolted to a heat sink at an anodized interface. This configuration was deemed inadequate because of the many mechanical joints that could loosen with thermal expansion and the unknown thermal interface conditions between the cell block and the heat sink. This can be accomplished by carefully designed bolted joints between PV cell strings and heat sink mounting plate or a bonded joint (epoxy or solder). The advantage of a bolted joint is that it permits easy removal of the array. The disadvantage is that it results in a higher joint temperature difference, and consequently a higher array temperature.

Thermal Management

Various configuration trades were considered to remove the heat from the cell modules. There are two keys to maintaining the array temperature as low as possible. First, there must be good thermal coupling between the mounting plate and the heat transport device. A bonded joint is preferred because it results in a lower temperature difference. Second, there must also be good thermal coupling between the heat transport device and ambient air. Air and water were considered as the two primary candidate transport mediums.

Analysis indicated that air cooling would be difficult given the thermal load of 20 W/cm^2 . The area of the array is not sufficient to reject waste heat directly off the array itself. Heat transfer coefficients with an air flow simply cannot be made high enough to conduct the heat away without a very high array-to-air temperature difference and high parasitic blower power. Some heat transport mechanism, either passive heat pipes or an active coolant circuit, is required to remove heat away from the array to a heat exchanger where a sufficient dissipation area can be provided. Heat pipes would be the ultimate solution for portability and system efficiency due to the power and weight penalty of an electric pump system. An approach utilizing heat pipes as transport devices would eliminate the water pump power demand, but would increase cost beyond the scope of this project. Water cooling was determined to provide an optimal solution that met the performance requirements established for this program.

4.3.1.3 PV Module Assembly

The PV module assembly block diagram is shown in Figure 4.20. A key feature of the design is that the cells can be interconnected in various series and parallel schemes to accommodate the nonuniform emission at the array due to view factor effects.

The PV array is comprised of two manifold assemblies and eleven PV modules. The manifolds are constructed of aluminum, and provide a hard interface and coolant port for each module assembly. Each PV module assembly is populated with $1 \text{ cm} \times 12 \text{ cm}$ of cell area, thereby providing a PV array with 132 cm^2 of cell area.

The design approach here is quite unlike standard silicon concentrators. In this case, the PV cells are designed to maximize efficiency over the total active area by packaging highly responsive cells into a dense array configuration. The emitter design determines the area of the PV array and the cells are sized to provide the required terminal voltage and current. The flat cable interconnects are soldered using standard production processes. Figure 4.21 illustrates the modularity and tight packing factors of the module assembly (10 PV modules shown).

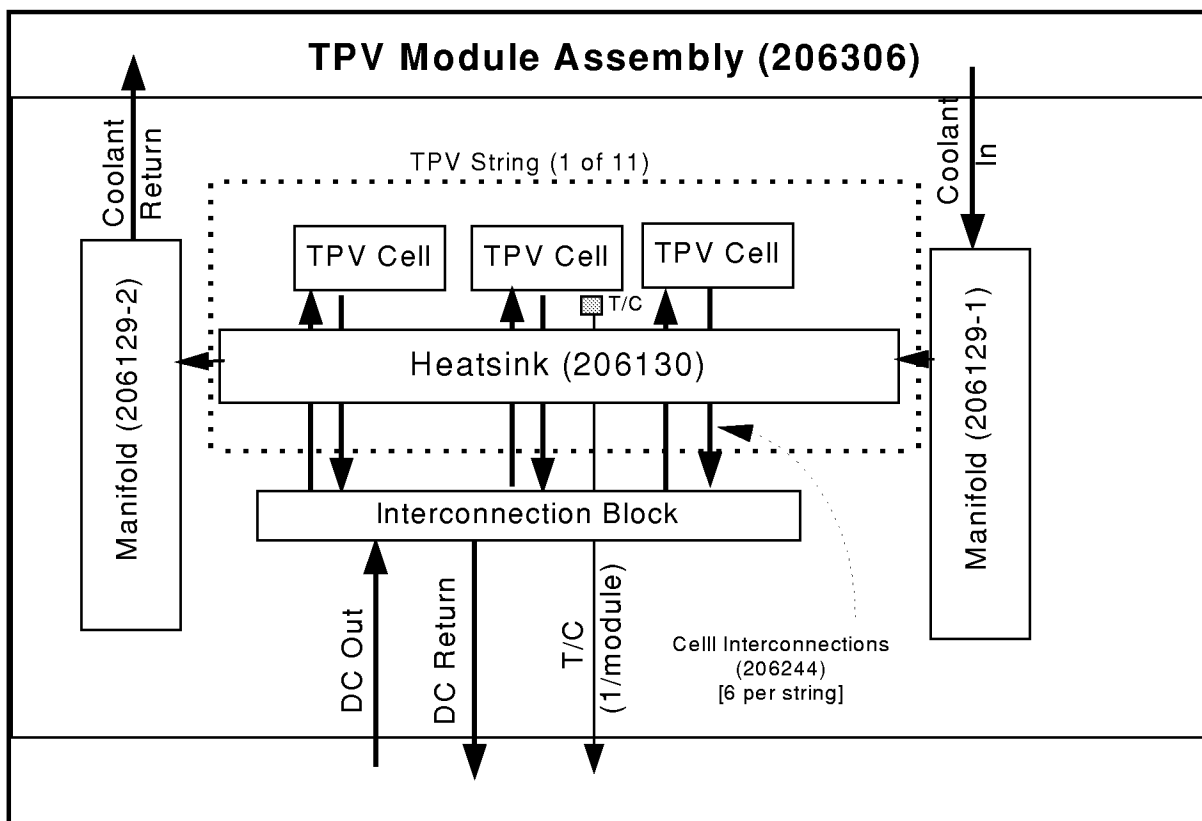


Figure 4.20 PV Module Assembly Block Diagram

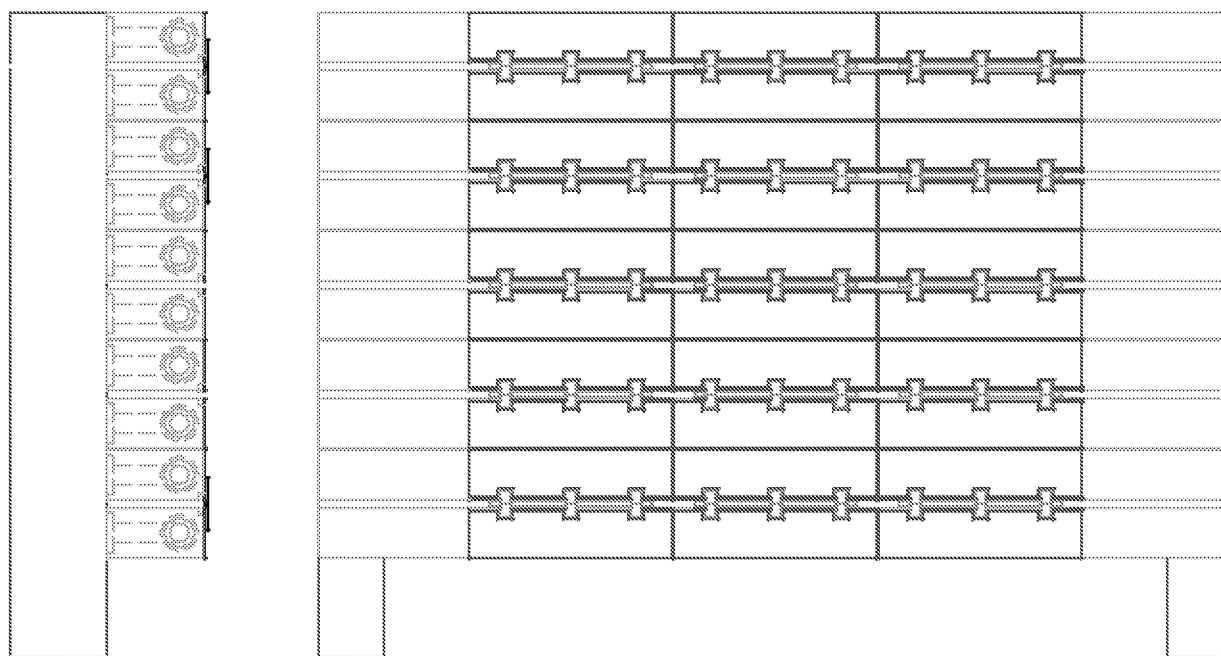


Figure 4.21 Side and Front View of PV Array Assembly

The high heat loads imposed upon the PV cells along with the inverse relationship between cell temperature and performance were significant drivers in the design of the module assembly. In order to achieve optimal performance and reliability, the photoarray heat sink is designed to transport all absorbed nonconvertible thermal energy away from the PV cells while limiting the temperature rise within a few degrees of ambient.

An increase in PV cell temperature translates in lower cell voltages at a rate of $0.4\%/^{\circ}\text{C}$. Although there is a slight increase in cell current with temperature, the net power output for the cell is inversely proportional to temperature. Given this relationship, maintaining optimum cell performance requires effective thermal management. The nominal cell temperature was established to be within 10°C of ambient. The module exceeded this requirement when subjected to a heat load of approximately $10\text{ W}/\text{cm}^2$ (Figure 4.22).

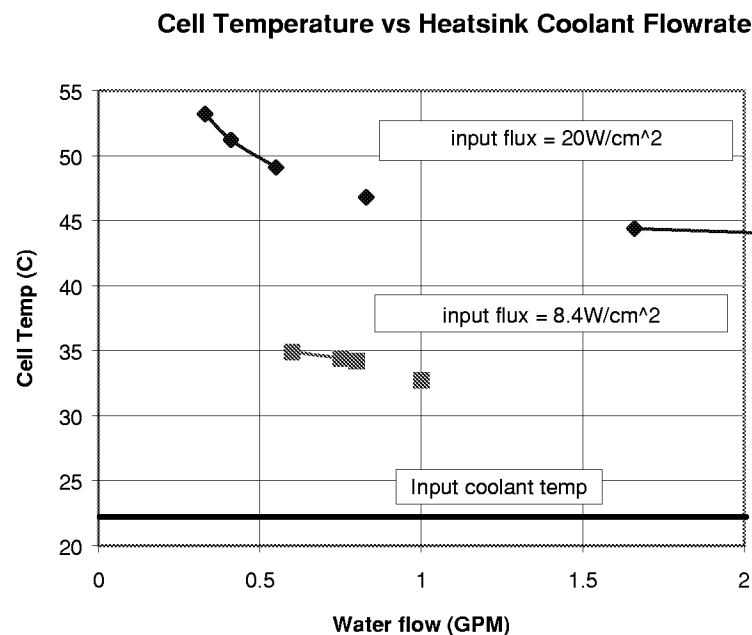


Figure 4.22 Module Thermal Performance

Heat Sink Design

The heat sink removes and rejects unwanted heat from the PV array to maintain high cell performance. The quantity of rejected heat is a direct function of the spectral content of the source, the quantum efficiency of the photocell, parasitic losses, and the electrical impedance of cell and load.

The heat sink design provides sufficient thermal conductivity while maintaining electrical isolation between the conductive metal bases of each photocell in order to preserve the integrity of the series connected photocell circuits. The electrical interconnection design provides an independent, low resistance and high-current carrying path to each cell. This approach simplifies the fabrication and repair while maximizing flexibility in the configuration and evaluation of the array.

Electrical Interconnect

Given the requirement of limitation on maximum cell temperature, the use of soldered interconnect was considered acceptable for this application. A brazed or welded contact could be used to withstand higher operational temperatures, but the requirement for reworkability pointed toward the use of solder for interconnect attachment.

Conventional interconnecting uses typically thin (.001" - .002") silver plated molybdenum or Invar and the interconnects are attached (soldered or welded) to the top of one cell and to the bottom of the next cell in series. In such a configuration, a string of interconnected cells must be bonded down simultaneously. After bonding, any subsequent reworking to replace a cell would be difficult if not impossible because the whole bottom of the cell should be bonded, including the interconnect area, for thermal sinking. These constraints also pointed to the need to make interconnects from each cell independent of other cell interconnects in the module and to make the electrical connections for the cell behind the heat sink, instead of physically between the cells.

Wire was initially considered to interconnect the cells. It was determined that the cells must be bonded to the heat sink under the whole active area of the cell. In order to do this, all interconnecting must be done only in the ohmic region to the cell. The concept was to use a small gauge (approximately 20 AWG) multi-stranded insulated wire soldered onto the front and back edges of the cell at ohmic. The small gauge was necessary to allow the insulated portion to pass through the narrow gap between the heat sinks (approximately 060") to the area behind the heat sinks. Each cell required 6 wires, three each for the top and bottom ohmic locations. Also, the current carrying capacity was to be on the order of 7-8 amps per cell translating to approximately 2.5 amps per wire. This capacity forced the minimum gauge wire size limit.

The idea of using a thin insulated copper conductor was pursued as a method of achieving the required ampacity within the envelope constraints. A thin flexible conductor could be soldered to the cells and, because it was not stranded, the wicking and subsequent stiffening of the conductor were expected to be minimized. The use of Kapton as the insulator was a good choice because of the heat involved and it is an industry standard for flex cables. A flex cable offered considerable advantages over the round wired approach. Each "flex cable" could be made to attach to either the top or the bottom of the cell and routed between the heat sinks to interconnect behind the heat sinks. The current carrying capacity is easily accommodated with three .004" thick by .040" wide pads on each flex cable (Figure 4.23) which solder to three points on either the top or the bottom of the cells. A test flex cable was made by hand and proved to accommodate the configuration as required.

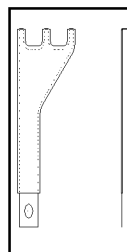


Figure 4.23 Flat Copper Cell Interconnect

Cell Design

The silicon PV cells are a critical element of the PV module subsystem. The salient design attributes of the PERL cell for this TPV application include: a response tailored to the spectral exitance of the fibrous ytterbia emitter, a size that allows practical module voltages via interconnections, and performance over sustained operation under concentrated light.

Spectral control is a key element for optimization of the PV cell. The spectral response of the cell is designed to allow tailoring to the spectral characteristics of the emitter. The PV cell was designed to be optimized for the approximately 55:1 power ratio that exists between a cell illuminated by the Tecogen emitter and a one-sun device. The spectral response is shifted, or tuned, by changing the diffusion and antireflection (AR) coating characteristics.

The convolution of the spectral response of the photocell and the spectral exitance from the emitter provides the current generated in the cell. A projection of the output power was calculated using theoretical values of V_{oc} , I_{sc} , and curve fill factor (CFF). An I-V curve for a thirty cell module is shown in Figure 4.24. An I-V curve for a three-cell TPV string under 12x concentration is shown in Figure 4.25. These graphs depict the performance potential of the design if used in front of a uniform light source.

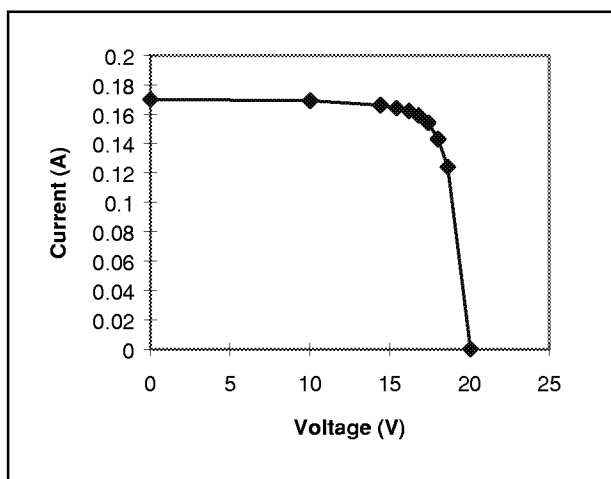


Figure 4.24 Thirty Cell Module Under 1x Solar Concentration

The optimum energy conversion efficiency is obtained when the product $J_{sc} \times V_{oc} \times CFF$ is maximized. J_{sc} optimization involves reducing the bandgap to cover as much of the emitter output wavelength, fine tuning the cell structure, and optimizing the antireflection coating designs. To maximize the cell voltage-curve fill factor product, the bulk carrier lifetime must be high and the cell surfaces and contacts must be passivated. The test results of the bulk lifetime measurements are presented in Table 4.4.

Improvement over standard silicon cells was achieved by additional processing of the back surface. A reflecting metal layer was deposited on the back surface of the Si TPV cell to reflect photons whose energy is below that of the active bandgap. The high reflectance of the material minimizes the impact of active area obscured by recouping the reflected photons. Some of the reflected photons returned to the emitter are expected to be recouped, thus enhancing the efficiency of the TPV system. This phenomena should augment the effect of the separate optical filter that is inserted between the emitter and TPV module.

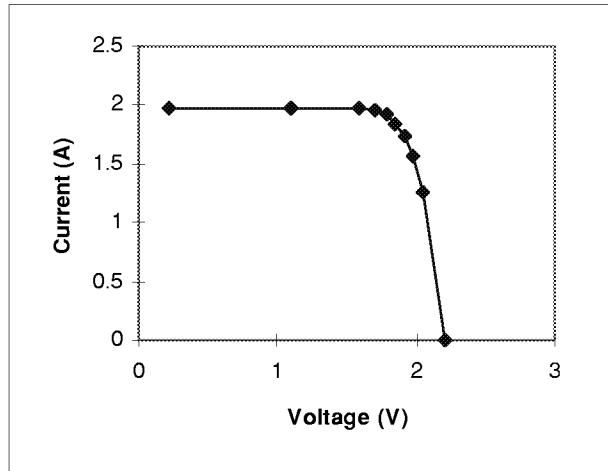


Figure 4.25 PV Module Under 12x Concentration

Table 4.4 Si Wafer Test Results

Wafer	Oxidation	Sinter	Passivation	Resistivity (Ohm-cm)	Lifetime (us)
TECSTAR #1	X			0.6	11.5
TECSTAR #1	X	X		0.6	25
TECSTAR #1	X	X	X	0.6	200
TECSTAR #2	X			0.72	n/a
TECSTAR #2	X	X	X	0.72	153
UNSW (Wacker)	X	X	X	0.5	116

Cell Processing

A textured front surface of the baseline cell design was selected as a means to reduce reflectance. With texturing, much of the energy that is normally reflected away from the cell is captured. The development of a pyramid pattern with the required geometric attributes required detailed tuning in concert with other process variables. Many variations in chemical and photolithography processing techniques were tested in order to mitigate undercutting inherent during pyramid etching.

The front and back surfaces are passivated to minimize the recombination of locally generated carriers. This increases the cell voltage and also increases current. The passivation layers are clean SiO₂ layers thermally grown at a well-controlled high temperature.

The contacts are particularly important for the TPV device. The front contact is grid with sufficient metal coverage to collect and conduct the generated current, in this case around 2 A/cm². The contact metal to the rear contacts are also passivated to eliminate recombination. This is achieved by oxidation with photoresist registration about locally diffused contact region. The back surface contact metal contacts the back surface field in small unpassivated areas.

A chemically stable layer of protective silicon dioxide is essential. Every oxide thickness has to be perfect for the subsequent steps. The oxide process time and temperature profile are critical and were key development parameters. Many rework operations were required for such steps over the course of determining the optimum process techniques. Alternative processes such as oxide deposition and plasma etch and were considered.

A photolithography process produces the patterns of the photomask design on the surface of the wafer. Consistency in this process is critical. Optimization of the inherently large number of process variables was a time consuming task. Key parameters in this optimization included the thickness and uniformity of photoresist, soft bake temperature and duration, and exposure and developer settings.

4.3.2 PV Module Fabrication

Because of the complex nature of the cell design, there were many process factors that had to be considered in the course of manufacturing optimization. The optimization process was made manageable by identifying and modeling the salient features of each process. The result of each key step in the process was evaluated for specific parameters necessary to assert the achievement of results desired by the associated process step. An overview of the module fabrication process flow is provided in Figure 4.26.

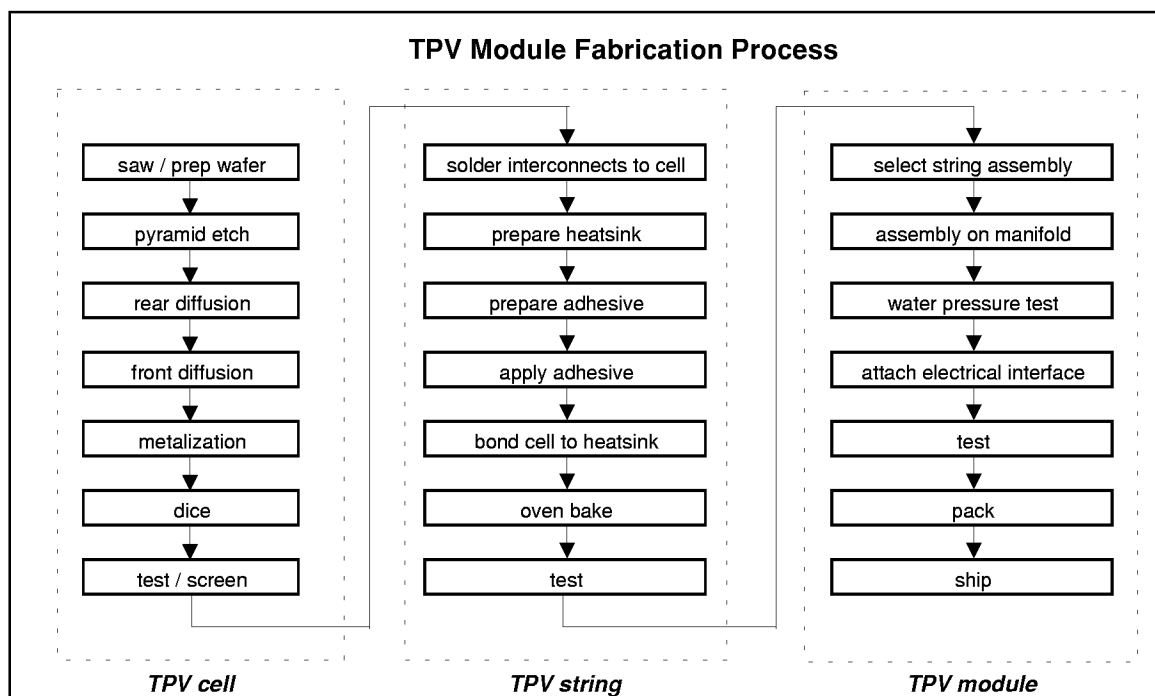


Figure 4.26 PV Module Fabrication and Test Flow Chart

4.3.3 PV Module Testing

The measured spectral response of the PV cell as a function of varying intensity levels is provided in Figure 4.27. An important consideration in the design was the material selection of the front surface grid used to collect generated currents. Low series resistance is crucial since each cell can carry several amps. The relationships of V_{oc} , I_{sc} and FF as a function of solar concentration that were achieved by the cell are shown in Figure 4.28. In this figure, the target zone represents the performance level needed to achieve the performance requirements established for the cell. The graph clearly depicts that V_{oc} is within the target zone, and I_{sc} and FF are approximately 13% below target. Given that the fill factor represents the highest percentage of power available from the power product ($I_{sc} \times V_{oc}$), it is clear that room for improvement exists.

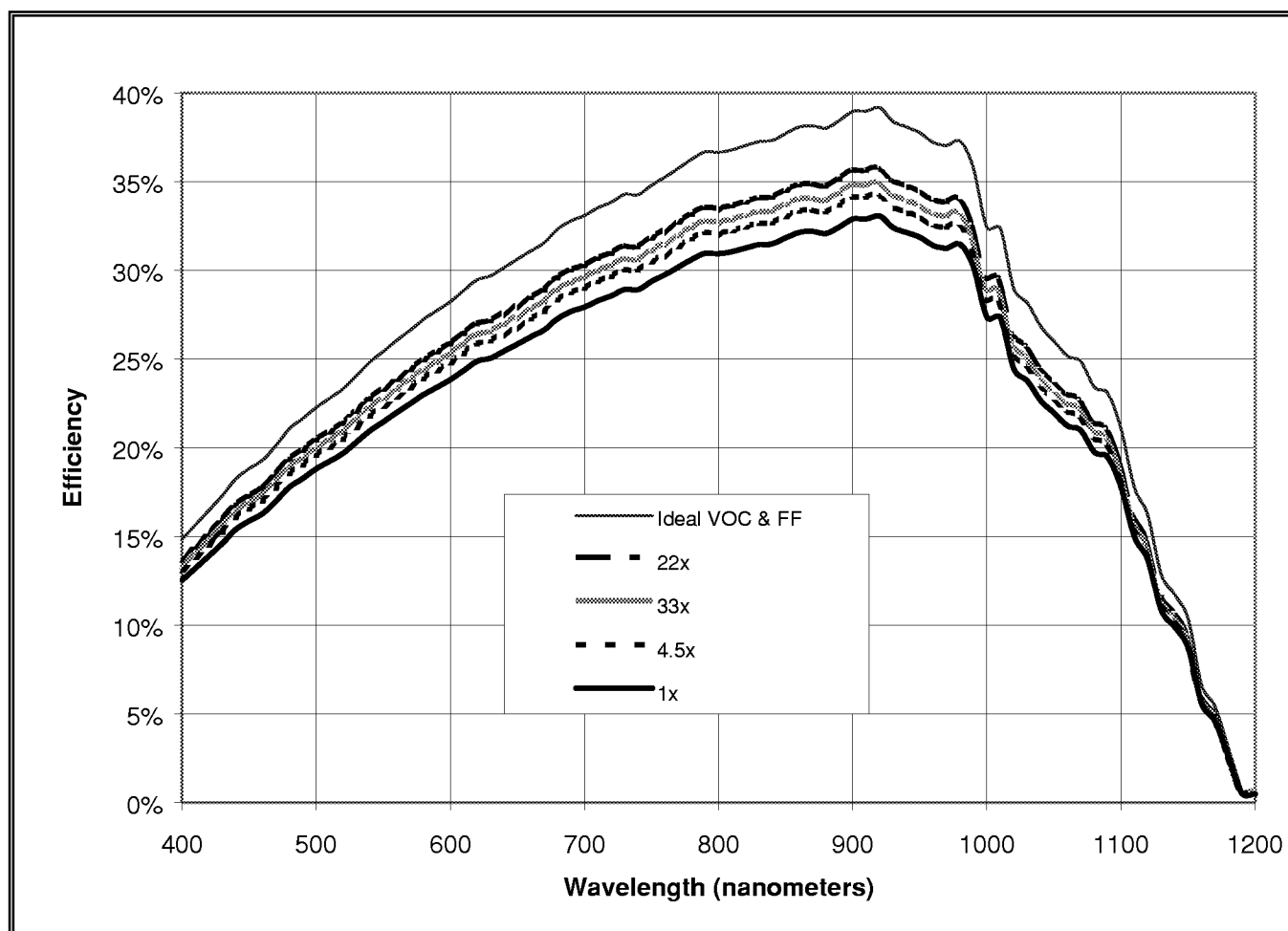


Figure 4.27 Spectral Characteristics Under Concentration

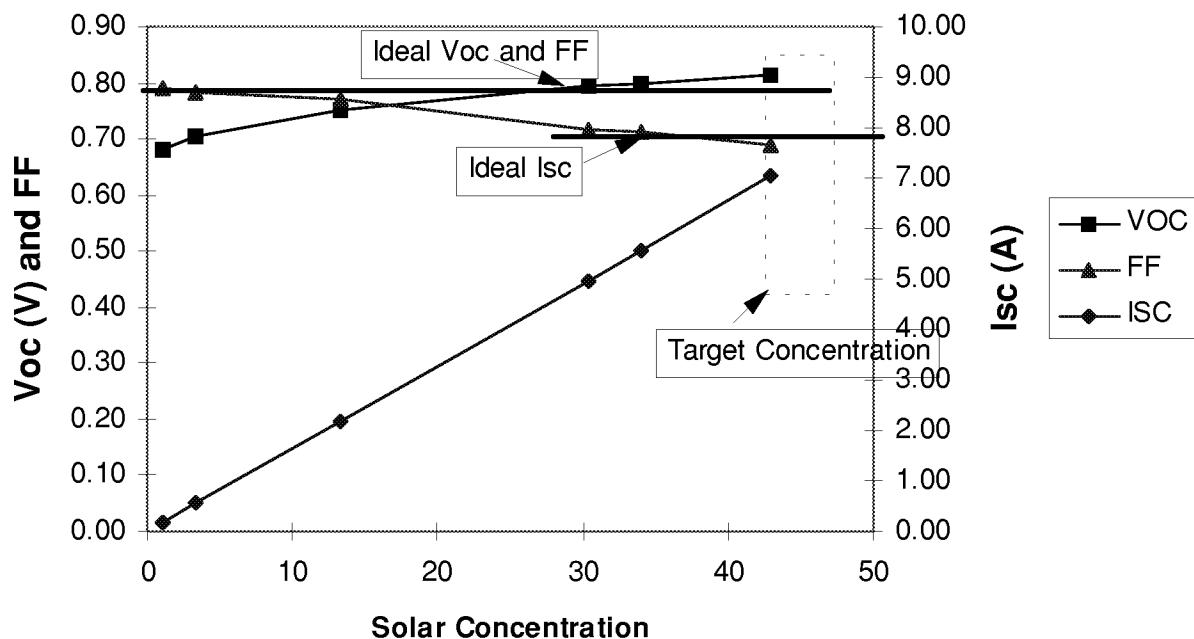


Figure 4.28 PERL Cell V_{oc} , I_{sc} and FF vs. Solar Concentration

The fill factor performance in this case is directly influenced by the presence of intrinsic series resistance. The series resistance losses become significant at the high current injection levels imposed under this application. As such, the focus for improved cell performance was centered upon lowering series resistance. Grid design and substrate characteristics have the greatest contribution to series resistance. The grid design utilized in this cell was optimized for a current density within a 40 to 70 equivalent sun concentration range. The substrate resistance was minimized by selecting wafers of lowest resistivity.

The summary of PV array performance compared to the design goal is presented in Table 4.5.

Table 4.5 PV Array Performance Summary

	<i>Design</i>	<i>Actual</i>
Si convertible input @ PV array	3.5 W/cm ²	2.8 W/cm ²
Number of cells/module	3	3
Number of cells/array	33	33
Array electric power	167	100 W
Average cell power	5.1 W	3.0 W
Average cell open circuit voltage	800 mV	803 mV
Average cell short circuit current	7.9 A	5.39 A
Average CFF	80%	70%
In-band cell efficiency	36%	27%

The test results presented in this section are for the baseline PERL cells made in the early part of the program by Unisearch LTD Consultants at the University of New South Wales. TECSTAR's development efforts at duplicating the process and producing a cell with characteristics that matched better with the ytterbia emitter were not successful. The baseline UNSW cells were, therefore, used for generator system prototypes.

4.4 RECUPERATOR DEVELOPMENT

A high degree of thermal recuperation is needed to achieve the desired overall system efficiency. In a recuperator, the waste heat in the flue gases leaving the emitter is transferred to the combustion air through a heat transfer surface, thereby recovering energy and saving fuel that would otherwise have been required. Because less fuel is used, less combustion air is required. The result is that a greater proportion of heat from the fuel is available for useful work. Flame velocity, i.e. the speed at which flame travels towards the fuel/air mixture, is also increased when combustion air is preheated. This permits a higher rate of heat release within a given combustion chamber volume. Flame temperatures are also increased when preheated air is used.

The relative performance of recuperators is commonly evaluated according to "recuperator effectiveness" which is typically defined as the ratio of actual heat transfer rate to a thermodynamically limited maximum possible heat transfer rate. The relationship among recuperator effectiveness, flue gas inlet temperature, and combustion air preheat temperature is shown in Figure 4.29.

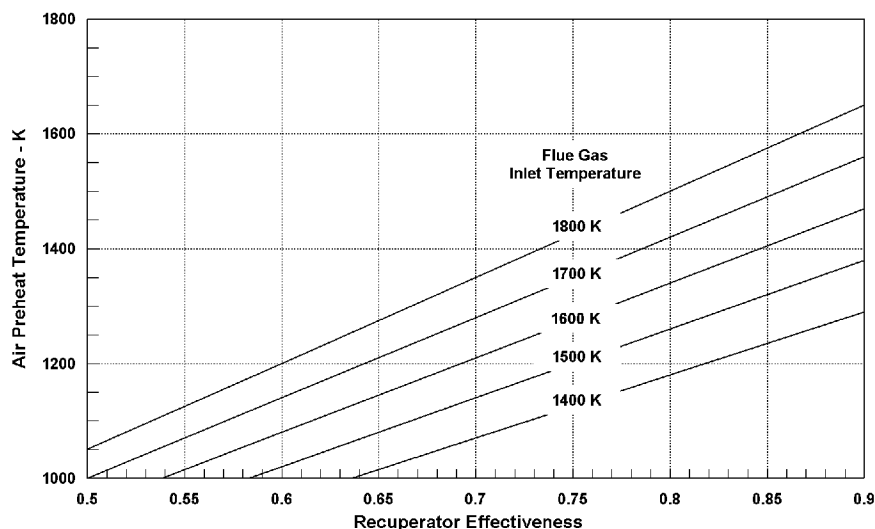


Figure 4.29 Air Preheat Temperature vs. Effectiveness for a Range of Flue Gas Inlet Temperatures

The desired air preheat temperature and the flue gas temperature are the key determinants of the recuperator material. However, temperature related effects such as material differential expansion, thermal shock, and thermal conductivity must be considered and accounted for in a recuperator design. Metallic heat exchangers, used most often in industry, have two major limitations - temperature and corrosion. When constructed of stainless steel, the bulk material temperature should not exceed 650°C and the flue gas inlet temperature should be less than 800°C. A stainless steel heat exchanger must therefore be protected by diluting the flue gas which will lower its performance. A ceramic heat exchanger is therefore

required to achieve the desired air preheat temperatures. Ceramics can withstand considerably higher temperatures and are less susceptible to attack by flue gas constituents. However, proper design features are required for ceramic recuperators to achieve compact size and leak-free operation as well as avoid temperature related problems such as thermal stress, fatigue cracks, and plastic deformation.

Table 4.6 compares the relevant thermal properties of potential ceramic recuperator materials. The baseline material chosen for the initial prototypes was cordierite ($2\text{MgO} \cdot 2\text{Al}_2\text{O}_3 \cdot 5\text{SiO}_2$). Future recuperators will be fabricated using higher temperature materials like silicon carbide and whisker reinforced alumina.

Table 4.6 Ceramic Recuperator Material Options

Recup. Material	Max. Use Temp., °C	Air Preheat Temp., °C		Coeff. of Thermal Expans. $10^{-6}/^\circ\text{C}$	Thermal Conductivity		Thermal Shock Resistance	
		$\varepsilon = 0.8^1$	$\varepsilon = 0.9^1$		W/m-K @20°C	Rating	ΔT_c^2 , °C	Rating
Cordierite	1250	1000	1125	1.5	5	Fair	500	Good
Silicon Nitride	1250	1000	1125	3	20	Good	700	Very Good
Aluminum Titanate	1350	1075	1200	0.5	8	Fair	1000	Excell.
Silicon Carbide	1700	1350	1500	4.0	100	Excell.	375	Good
Whisker Reinforced Alumina	1750	1400	1575	7	35	Very Good	700	Very Good
Alumina	1850	1475	1650	7.5	35	Very Good	250	Fair

¹ ε : Recuperator effectiveness

² ΔT_c : Critical temperature differential at which thermal stress exceeds material fracture strength.
(Reference: Coors Ceramic Company)

The physical configuration selected for the design was plate-fin in which the exhaust gases and the combustion air pass through relatively small alternate passages which accounts for its compact size. The passages are separated by flat plates covered with many fins which significantly increase the amount of heat transfer and give it a high effectiveness. The core of the recuperator is a monolithic honeycomb matrix made of cordierite, a highly thermal stress-resistant mixed oxide ceramic. The major advantage of the monolithic approach is that there are no joints in the core of the heat exchanger and the associated problems of sealing. The compact, ceramic, counter-flow recuperator core is modified at the two ends, as shown in Figure 4.30, by machining and cement (bonding agent) sealing to provide cross flow headers for one of the two fluid streams (flue gas or air). The recuperator assembly consists of this ceramic core, a resilient fibrous refractory seal (gasket), and a metallic housing. The unit is then put under a slight compression from a spring assembly to prevent leakage across ceramic-to-ceramic surfaces.

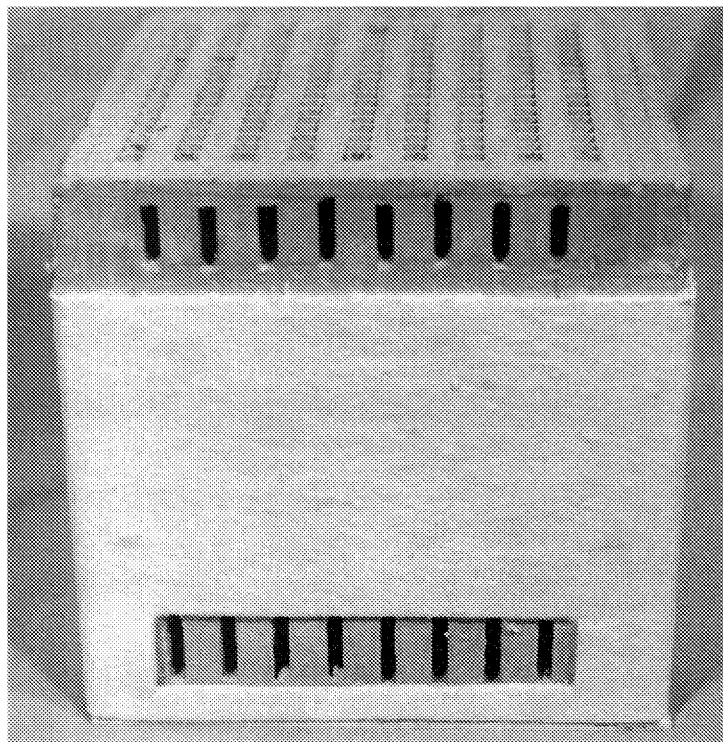


Figure 4.30 Ceramic Recuperator

Three different types of recuperator cores with cell densities of 16 cells/in², 25 cells/in², and 50 cells/in² were selected for calculating recuperator effectiveness and the resulting air preheat temperatures. The comparison of dimensional characteristics like flow passage size, wall thickness, etc. for the three matrices is shown in Table 4.7.

Table 4.7 Recuperator Core Dimensional Characteristics

Cell Density, cells/in² (cells/cm²)	16 (2.48)	25 (3.88)	50 (7.75)
Wall Thickness, inches (cm)	0.045 (0.114)	0.035 (0.089)	0.025 (0.064)
Web Centers, inches (cm)	0.25 (0.635)	0.2 (0.508)	0.141 (0.358)
Hydraulic Diameter, inches (cm)	0.205 (0.521)	0.165 (0.419)	0.116 (0.295)
Open Frontal Area, %	67.2	68.1	67.8
Geometric Surface, in ² /in ³ (cm ² /cm ³)	13.1 (5.16)	16.5 (6.50)	23.3 (9.17)
Bulk Density, gms/in ³ (gms/cm ³)	9.13 (0.56)	8.90 (0.54)	8.98 (0.55)

The results of the calculations comparing the effectiveness of the three core matrices is shown in Table 4.8. The calculations were done for a two module TPV converter with a gross power output of

about 250 to 375 watts (see Table 3.1), a recuperator core size of 15 cm x 15 cm x 15 cm, and fuel firing rates of 3000 watts, 6000 watts, and 12000 watts. The three fuel rates correspond to gross system efficiencies of 10%, 5%, and 2.5% respectively for a gross power output of 300 watts.

Table 4.8 Recuperator Heat Transfer Effectiveness of Various Cell Density Cores at Several Fuel Firing Rates

	Case A	Case B	Case C
Cove Cell Density, cells/in ² (cells/cm ²)	16 (2.48)	25 (3.88)	50 (7.75)
Core Size (cm x cm x cm)	15 x 15 x 15	15 x 15 x 15	15 x 15 x 15
Effectiveness at Fuel Inputs ¹ of:			
3,000 Watts	95%	98%	99%
6,000 Watts	82%	91%	98%
12,000 Watts	64%	76%	91%
Air Preheat Temperature ² at Fuel Inputs of:			
3,000 Watts	1456 K	1502 K	1522 K
6,000 Watts	1308 K	1414 K	1501 K
12,000 Watts	1083 K	1235 K	1410 K

¹ The three fuel rates correspond to overall system efficiencies of 10%, 5%, and 2.5%, respectively, for a total power output of 300 W_e.

² For flue gas inlet temperatures of 1523 K, the maximum recommended temperature for cordierite recuperator material selected for initial prototypes.

Recuperator prototypes of 16 cells/in² and 50 cells/in² were fabricated and tested in the complete system laboratory prototypes. The test results of system prototype testing are presented in Section 5. As expected, the 50 cells/in² recuperator exhibited higher effectiveness and air preheat temperatures than the 16 cells/in² unit. However, at high flow rates, which are associated with slightly higher pressures, some leakage across the recuperator walls from the combustion air side to the flue gas side was observed for the 50 cells/in² core. These test results indicated that a recuperator core cell density of 25 cells/in² should be tested in the next phase since it may provide the optimum choice for obtaining high effectiveness and no leakage across the walls.

5. LABORATORY PROTOTYPE DEVELOPMENT

Laboratory prototypes of both Configurations A and B, described earlier in Chapter 3 and shown in Figures 3.4 and 3.5, were fabricated and tested. The Configuration A prototype is a one module system (one emitter and one array) whereas the Configuration B prototype is a two module system. Each prototype has only one recuperator.

In the Configuration A prototype, fuel tubes are located in the air passages within the substrate just below the surface and fuel is injected from orifices in the fuel tubes to mix with preheated air. Configuration B achieves the same goal with a different fuel tube configuration which requires a considerably larger number of fuel tubes. In both configurations, fuel is delivered from the fuel plenum through fuel tubes to very near the surface of the substrate and mixed with the preheated air. In order to meter and measure the combustion air flow accurately, a laboratory air supply and rotameter was used instead of the blowers shown in Figures 3.4 and 3.5. The laboratory prototypes used once-through water flow for cooling the PV arrays instead of air cooling as shown in the figures. Also, the Configuration B prototype was tested upside down compared to the orientation shown in Figure 3.5. The photographs of the prototypes, some construction details, and the test results are presented in the following sections. The fuel used for all the tests was methane.

Initial operation of the Configuration A laboratory prototype exhibited the same problems with the dielectric filter as described in Section 4.2.1. As a result, all the performance testing of both Configuration A and Configuration B prototypes were conducted without the dielectric filter coating on the second quartz window. The manufacturing defect with the dielectric filter has since been resolved and future testing will be performed with the dielectric filter.

5.1 CONFIGURATION A LABORATORY PROTOTYPE

The details of the emitter design, with respect to fuel and air delivery, are shown in Figure 5.1 for the Configuration A laboratory prototype. It shows perforated fuel tubes placed in between the rows containing ytterbia fibers. A total of 20 fuel tubes with 35 orifices in each tube were used. This provided 700 micromixing locations within the 12 cm x 12 cm active area of the emitter.

The fuel tubes were designed to be made of a ceramic material (cordierite or alumina) capable of withstanding the high air preheat temperature. However, because of time and cost constraints, and to obtain preliminary data on this micromixing approach, the laboratory prototype was tested with water-cooled metallic (inconel) tubes. The manifold design for the water-cooled fuel tubes is shown in Figure 5.2. It shows coaxial water tubes located within the fuel tubes with the inlet water and fuel manifolds on one side of the tubes and the outlet manifolds on the other side.

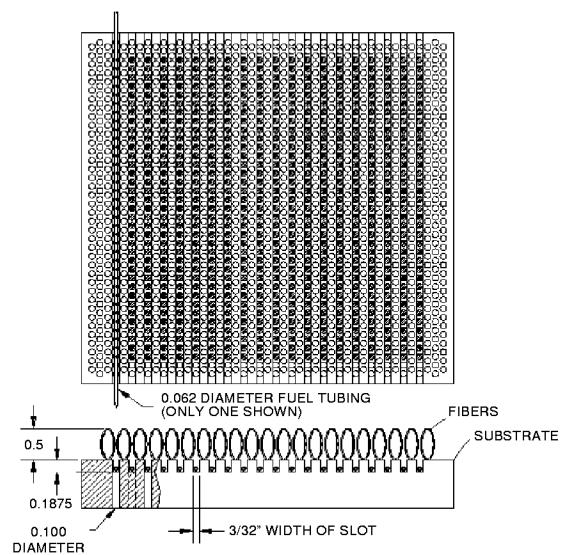


Figure 5.1 Configuration A Emitter

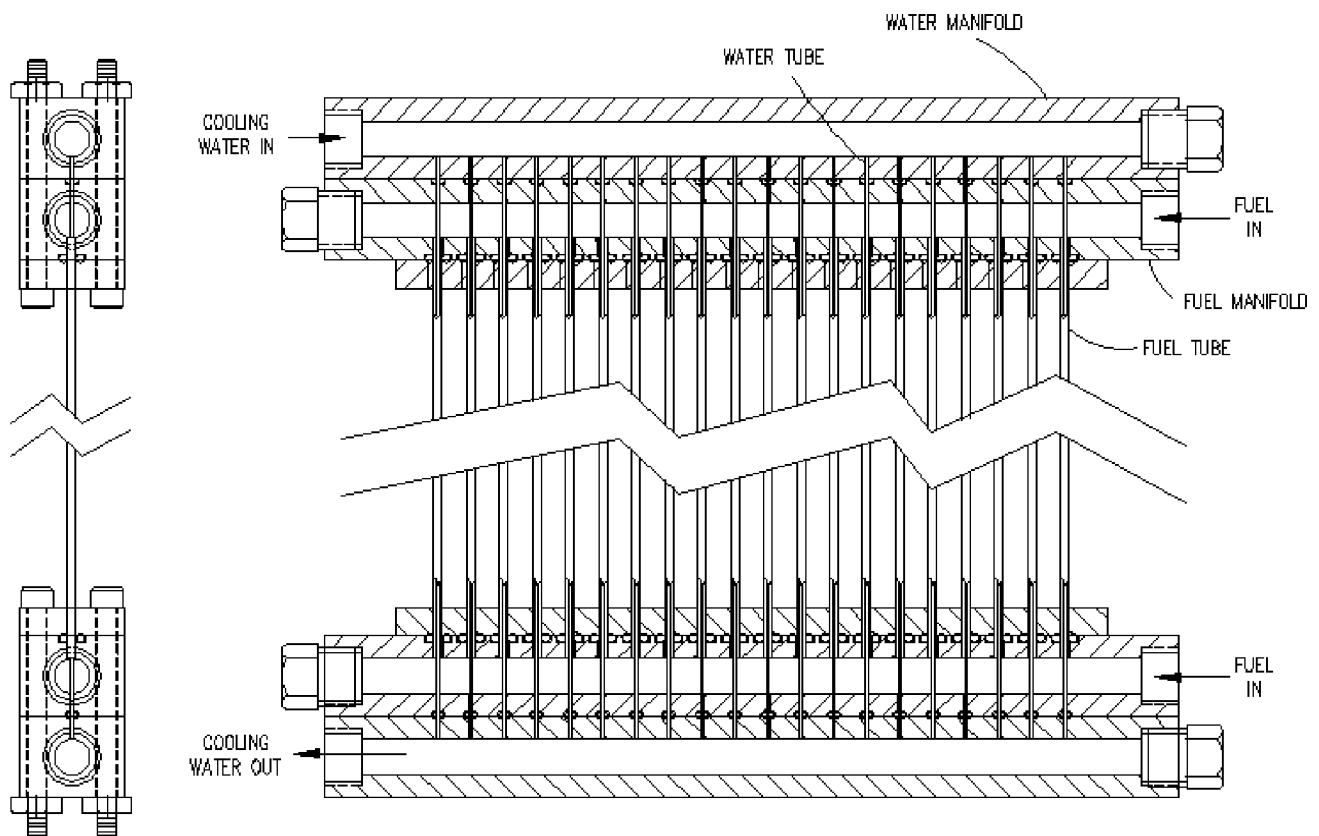


Figure 5.2 Configuration A Water-Cooled Fuel Tube Manifold Assembly

Photographs of the Configuration A laboratory prototype are shown in Figures 5.3 to 5.5. The test setup is depicted in Figure 5.3, the emitter viewed through a dielectric filter is depicted in Figure 5.4, and the swing-away PV array is shown in Figure 5.5.

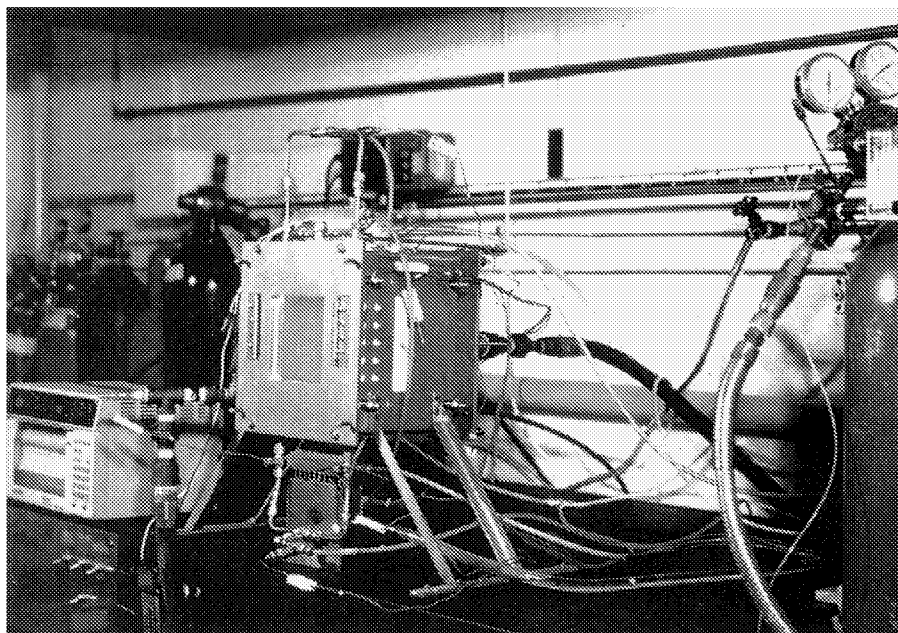


Figure 5.3 Configuration A Prototype – Test Setup

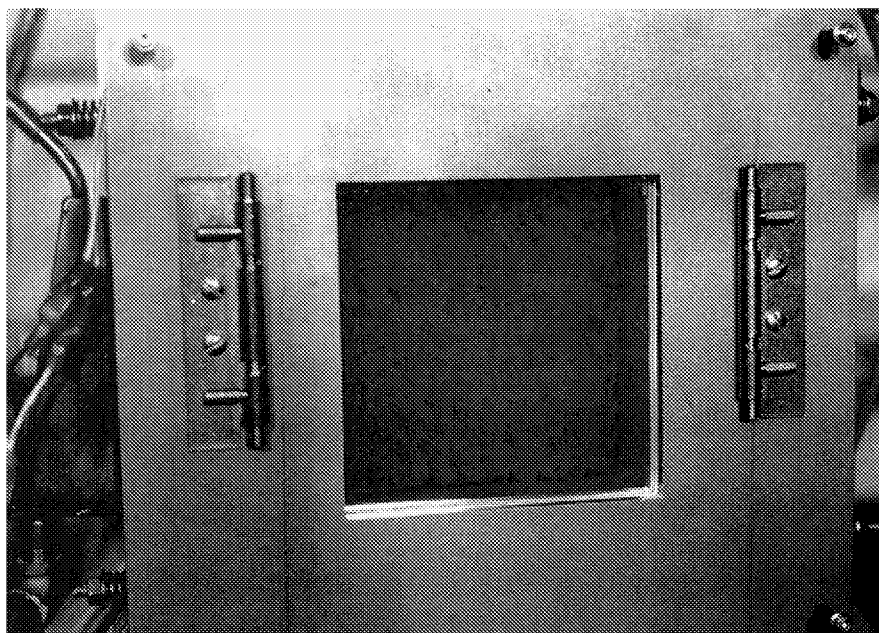


Figure 5.4 Configuration A Prototype – Emitter Viewed Through a Dielectric Filter

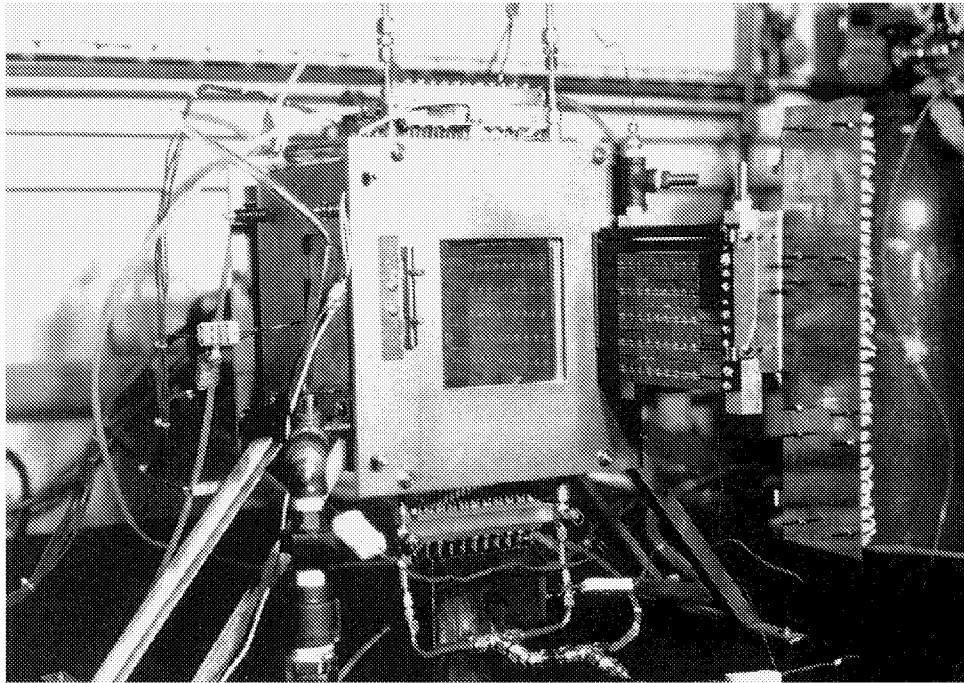


Figure 5.5 Configuration A Prototype – Assembly With Swing-Away PV Array

The silicon convertible exitance measured for this prototype, without the optical filter, is plotted in Figure 5.6 as a function of fuel loading. The design target exitance of 3.5 W/cm^2 was obtained at a fuel loading of $\sim 88 \text{ W/cm}^2$. The water-cooling of the fuel tubes resulted in a substantial heat loss and corresponding increase in fuel loading. Based on later tests with the Configuration B prototype, where the design target exitance of 3.5 W/cm^2 was obtained at a fuel loading of $\sim 50 \text{ W/cm}^2$, the water-cooling of the fuel tubes was estimated to have increased the fuel loading by $\sim 38 \text{ W/cm}^2$. These tests results clearly showed that water-cooling fuel tubes in a high temperature region, while useful in obtaining data, was not a viable long term approach for Configuration A.

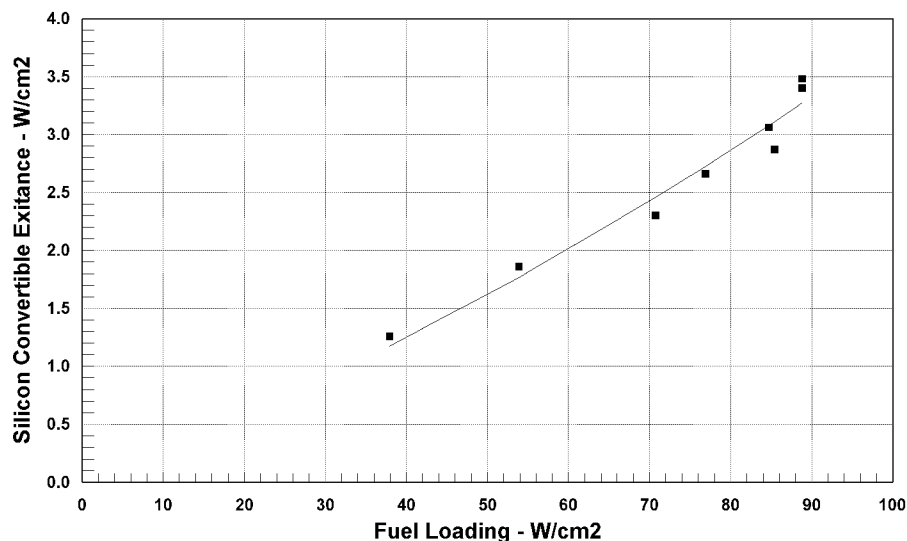


Figure 5.6 Configuration A Prototype – Test Results (No Optical Filter)

The PV cells in the array were connected in three parallel circuits with 11 cells connected in series in each circuit. The location of the PV cells in each of the three circuits is illustrated in Figure 5.7. The location of the PV cells for each of the three circuits was selected to provide the best possible current balance based on prior individual measurements of the current flow through each PV cell. The highest current flows through circuit 1, and the lowest current flows through circuit 3.

3	3	3
3	1	3
2	1	2
2	1	2
2	1	2
1	1	1
2	1	2
2	1	2
2	1	3
3	1	3
3	3	3

Figure 5.7 Location of Cells in the Three Parallel Circuit of PV Array.

The results from the testing of the PV array (11 modules, 33 cells) on the Configuration A prototype are presented in Figures 5.7 to 5.10. The measured current-voltage characteristics and the power characteristics of the PV array are shown in Figures 5.8 and 5.9 respectively. The convertible exitance at the emitter, which was held constant for each series of measurements, is also listed on the figures. At the PV array, the average convertible exitance falling on the cells is reduced to 80% of the convertible exitance at the emitter due to the view factor effect. The voltage at which the peak power occurred dropped substantially as the emitter exitance, and correspondingly the short circuit current, were increased. The fill factor and open circuit voltage measured for the PV array are presented in Figure 5.10. The maximum power output of 75 W was measured at an emitter exitance of 3.68 W/cm² and a 5.0 volts. The fill factor for the PV array was 0.55 at this operating point.

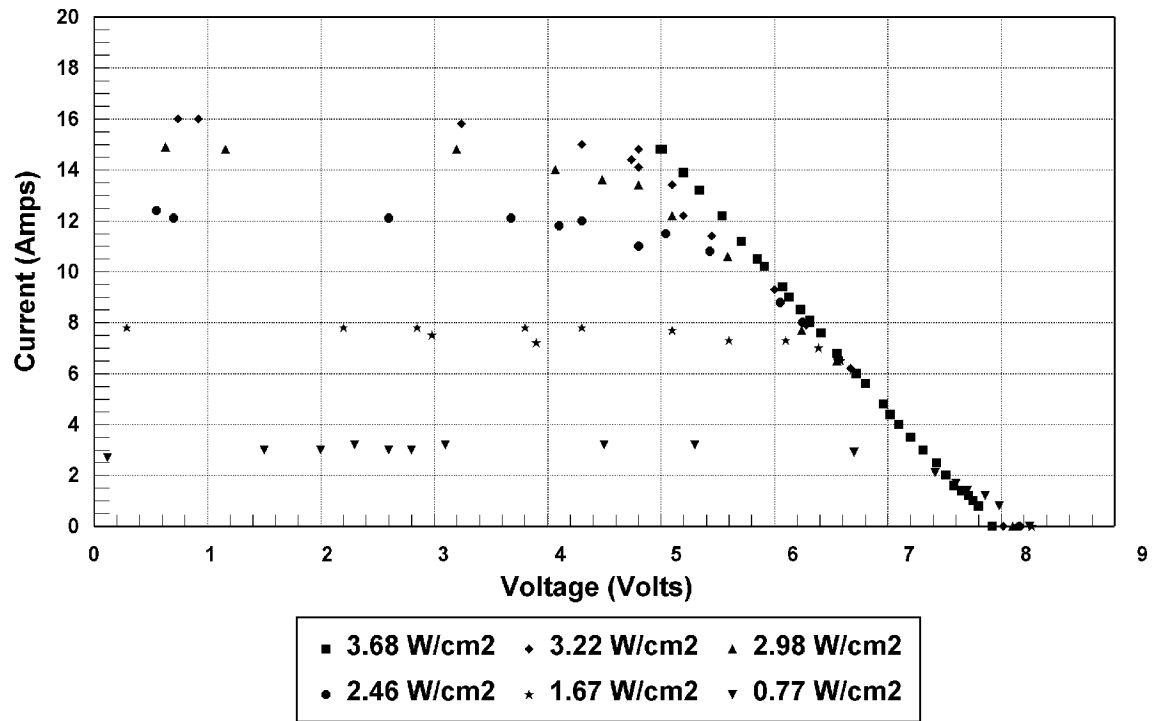


Figure 5.8 Configuration A Current – Voltage Characteristics

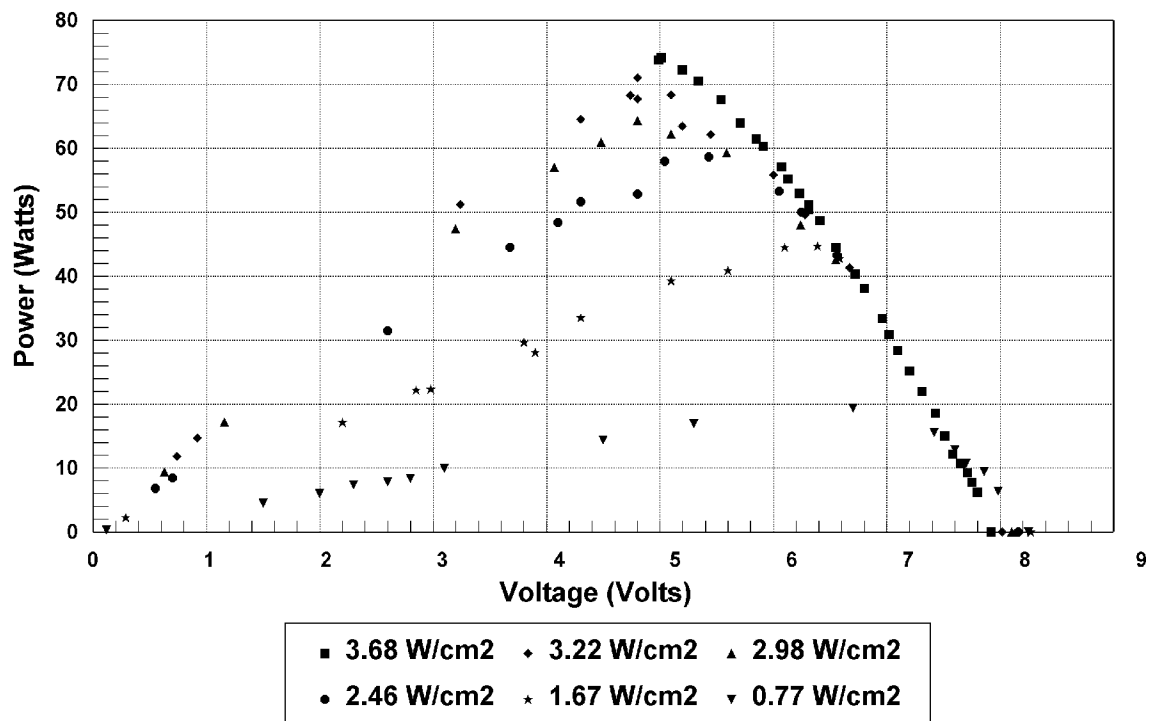


Figure 5.9 Configuration A Power Characteristics

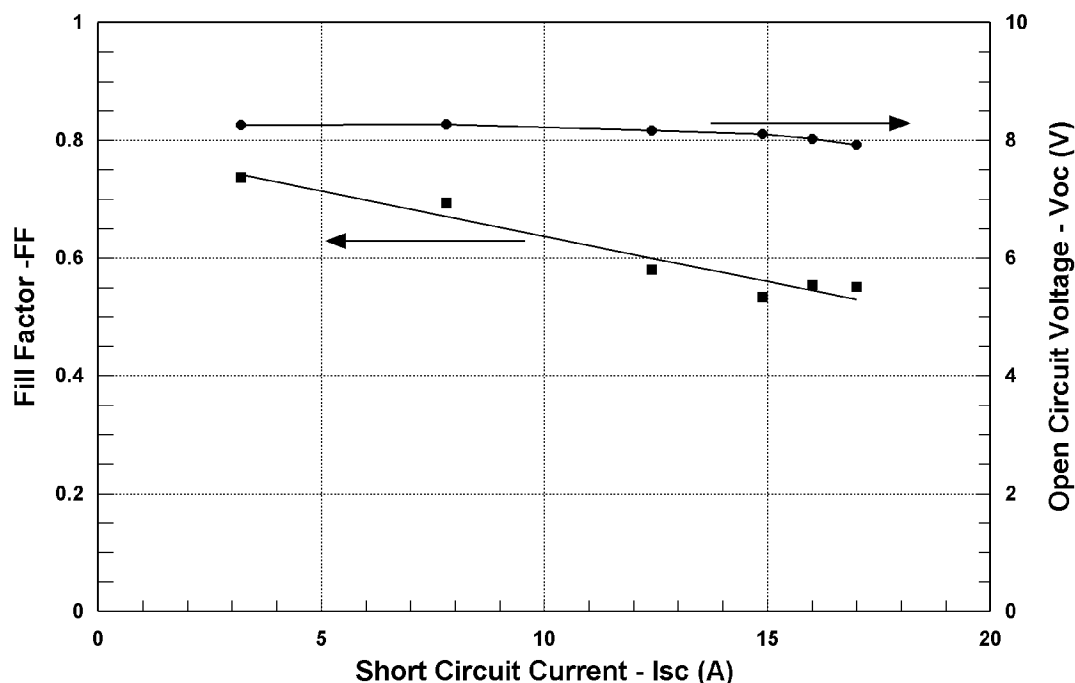


Figure 5.10 Configuration A Fill Factor and Open Circuit Voltage

5.2 CONFIGURATION B LABORATORY PROTOTYPE

The details of the emitter design, with respect to fuel and air delivery, are shown in Figure 5.11 for the Configuration B laboratory prototype. It shows the fuel delivery through ceramic tubes from the back of the emitter. A total of 350 fuel tubes were used within the 12 cm x 12 cm active area of each emitter. The manifold assembly for this configuration is shown in Figure 5.12. A water-cooled metallic fuel plenum/face plate along with an O-ring sealed fuel tube assembly was used to prevent any fuel leakage from the plenum. The heat loss associated with the water-cooling in this case is very low, when compared to the water-cooling loss in Configuration A, because it takes place in a cold zone where the heat transfer is low. A short, close-fitting wire was placed in the cold, inlet end of each ceramic fuel tube to form an annular orifice to control the fuel flow through the tube. By selectively matching the wires to the fuel tubes, it was possible to achieve a uniform distribution of the fuel over the emitter.

Photographs of the Configuration B prototype components and subassemblies are shown in Figures 5.13 to 5.17. The partial assembly side view presented in Figure 5.13 shows one emitter subassembly in place over the recuperator. The ceramic fuel tubes, fuel plenum, emitter substrate and emitter fibers are visible in this partial assembly. A front view of this same partial assembly is shown in figure 5.14 and a close-up of the emitter face is shown in Figure 5.15. The emitter fibers are clearly visible in these pictures because the outer window is a clear quartz window without the dielectric filter. Hot-end and cold-end views of the recuperator with its insulation are shown in Figures 5.16 and 5.17 respectively.

Figure 5.18 shows the Configuration B laboratory prototype assembled and ready for test. The water-cooled PV array is in the swing-away position showing the emitter face and PV cells on one side of this two emitter prototype.

The results from the tests performed on the Configuration B laboratory prototype, without the dielectric filter, during the phase of the work covered by this report are presented in Figures 5.19 to 5.21. The silicon convertible exitance at the emitter, the recuperator effectiveness, the air preheat temperature exiting the recuperator, and the exhaust gas temperature entering the recuperator are plotted as a function of the fuel loading in Figures 5.19 and 5.20 for each test point. The electric power output from the two PV arrays is plotted in Figure 5.21 as a function of the silicon convertible exitance at the emitter.

As shown in Figure 5.19, the maximum silicon convertible exitance measured during these tests was 4.27 W/cm^2 , well above the design goal of 3.50 W/cm^2 . At the design silicon convertible exitance of 3.50 W/cm^2 the fuel loading was $\sim 50 \text{ W/cm}^2$. This is substantially below the fuel loading of $\sim 88 \text{ W/cm}^2$ required with the Configuration A laboratory prototype at the design point. The air preheat temperature was $\sim 1200 \text{ K}$ for most of the test points. At the maximum silicon convertible exitance of 4.27 W/cm^2 , the air preheat temperature was 1170 K . The recuperator effectiveness for the same test conditions is plotted in Figure 5.20. A recuperator effectiveness of 83% was measured at the design silicon convertible exitance of 3.50 W/cm^2 .

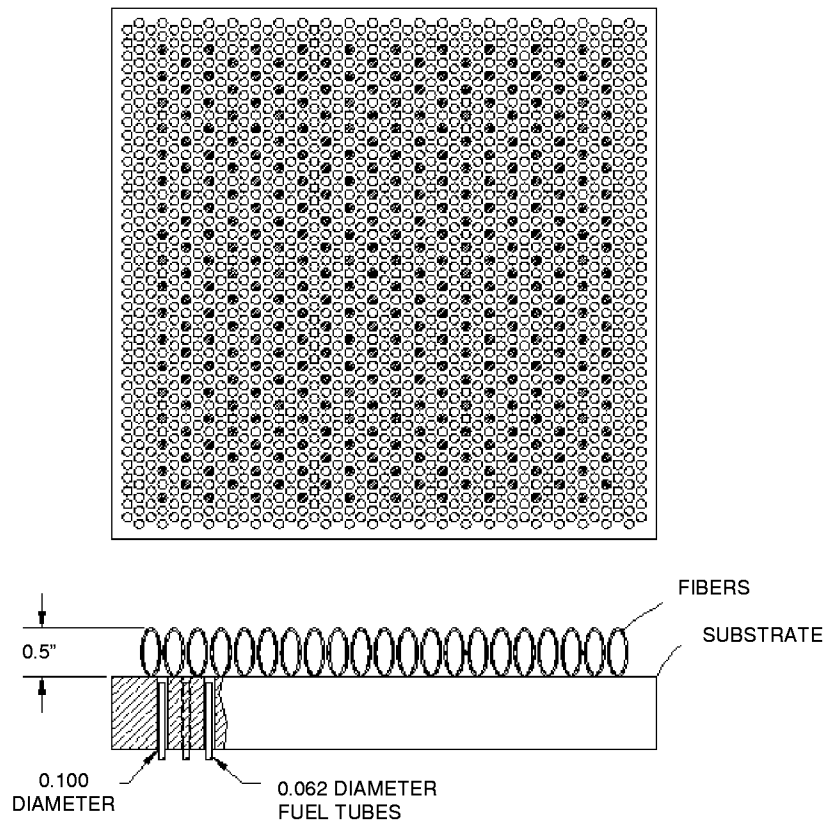


Figure 5.11 Configuration B Emitter

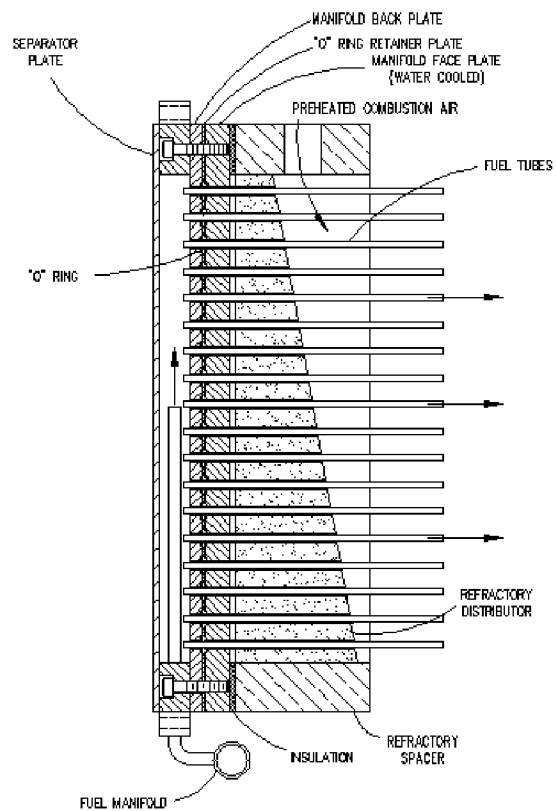


Figure 5.12 Configuration B Manifold Assembly

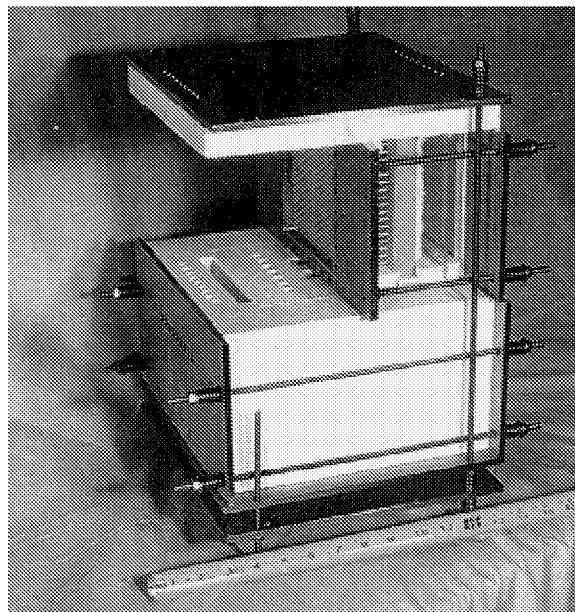


Figure 5.13 Configuration B Prototype – Partial Assembly (Side View)

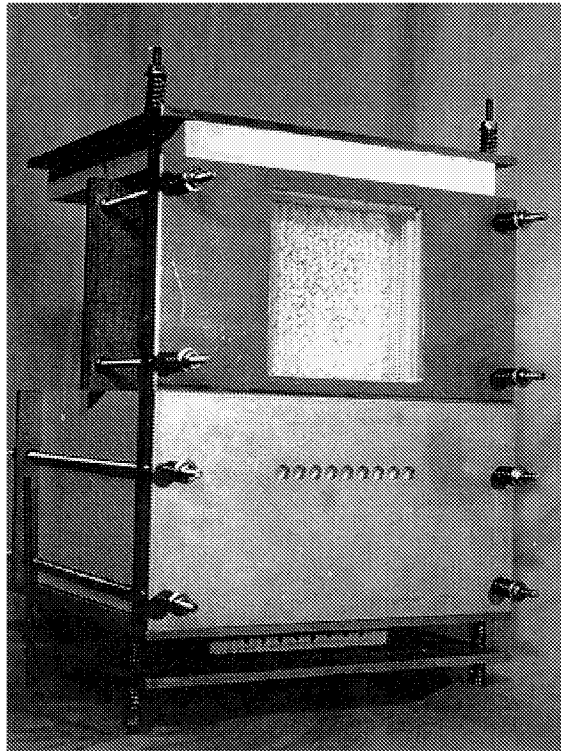


Figure 5.14 Configuration B Prototype – Partial Assembly (Front View)

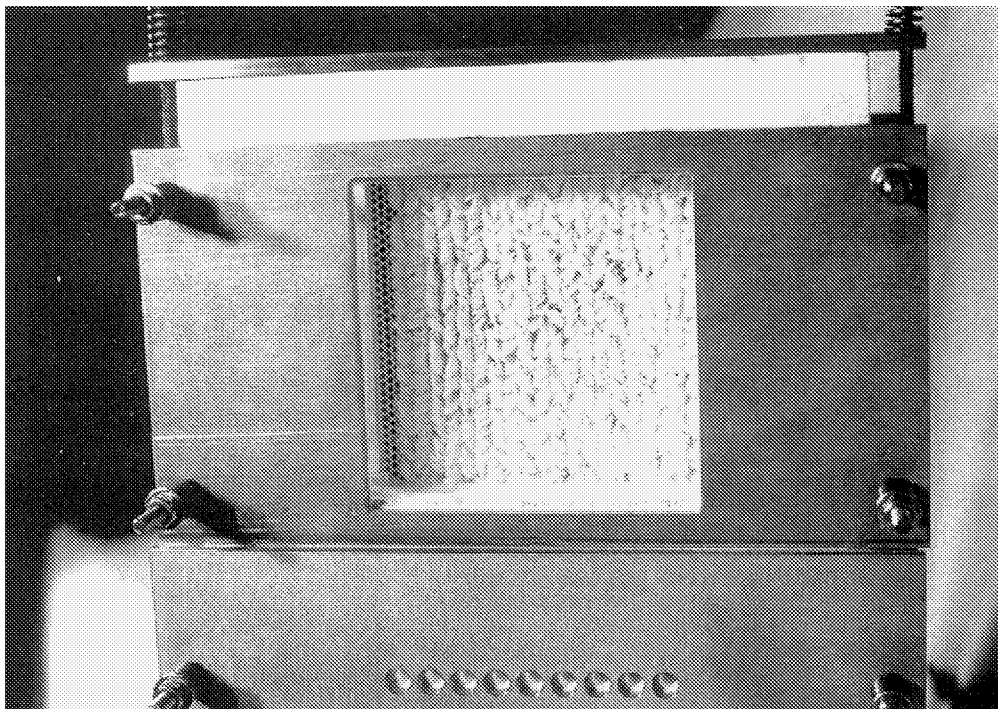


Figure 5.15 Configuration B Prototype – Emitter Face

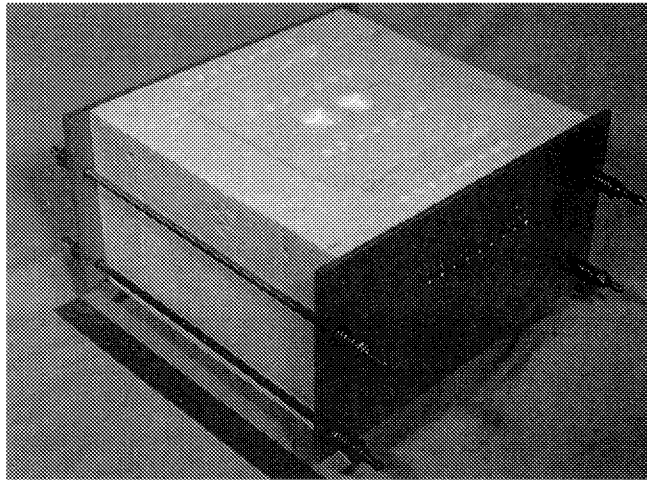


Figure 5.16 Configuration B Prototype – Recuperator (Hot End)

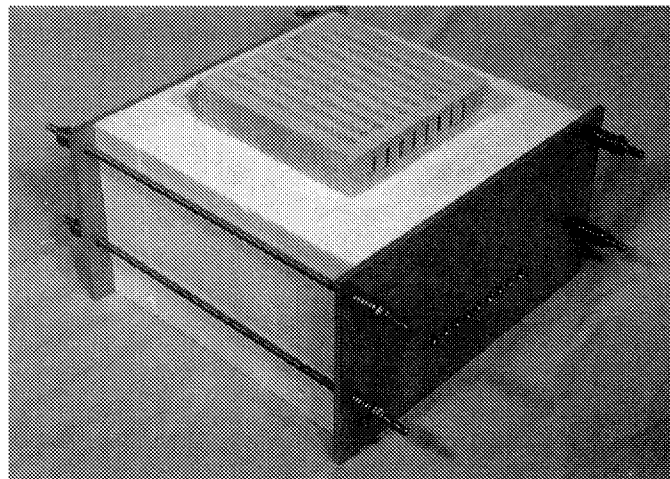


Figure 5.17 Configuration B Prototype – Recuperator (Cold End)

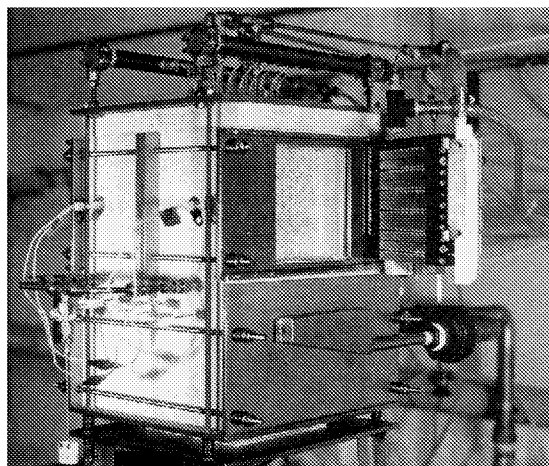


Figure 5.18 Configuration B Laboratory Prototype

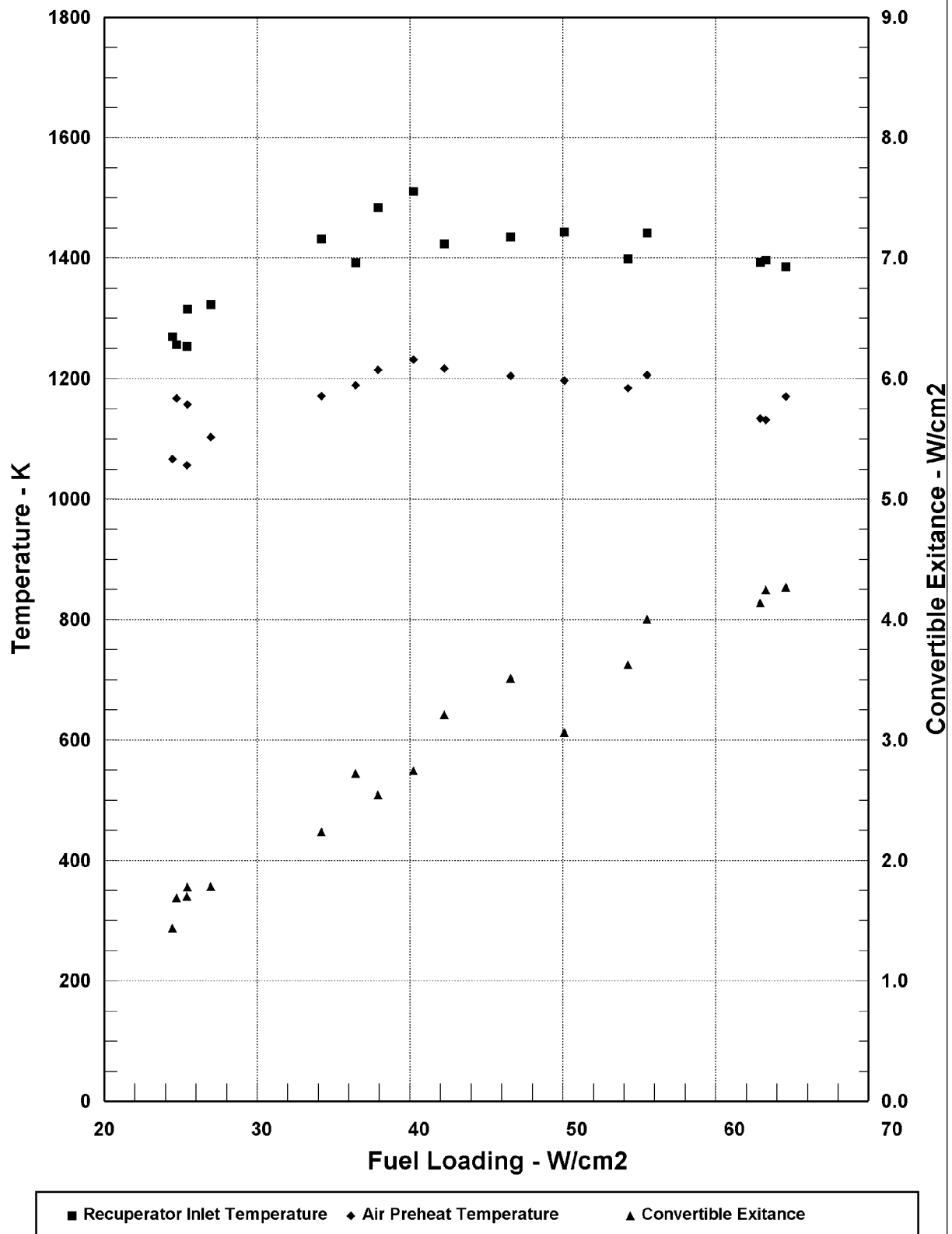


Figure 5.19 Configuration B Prototype – Test Data (No Optical Filter)

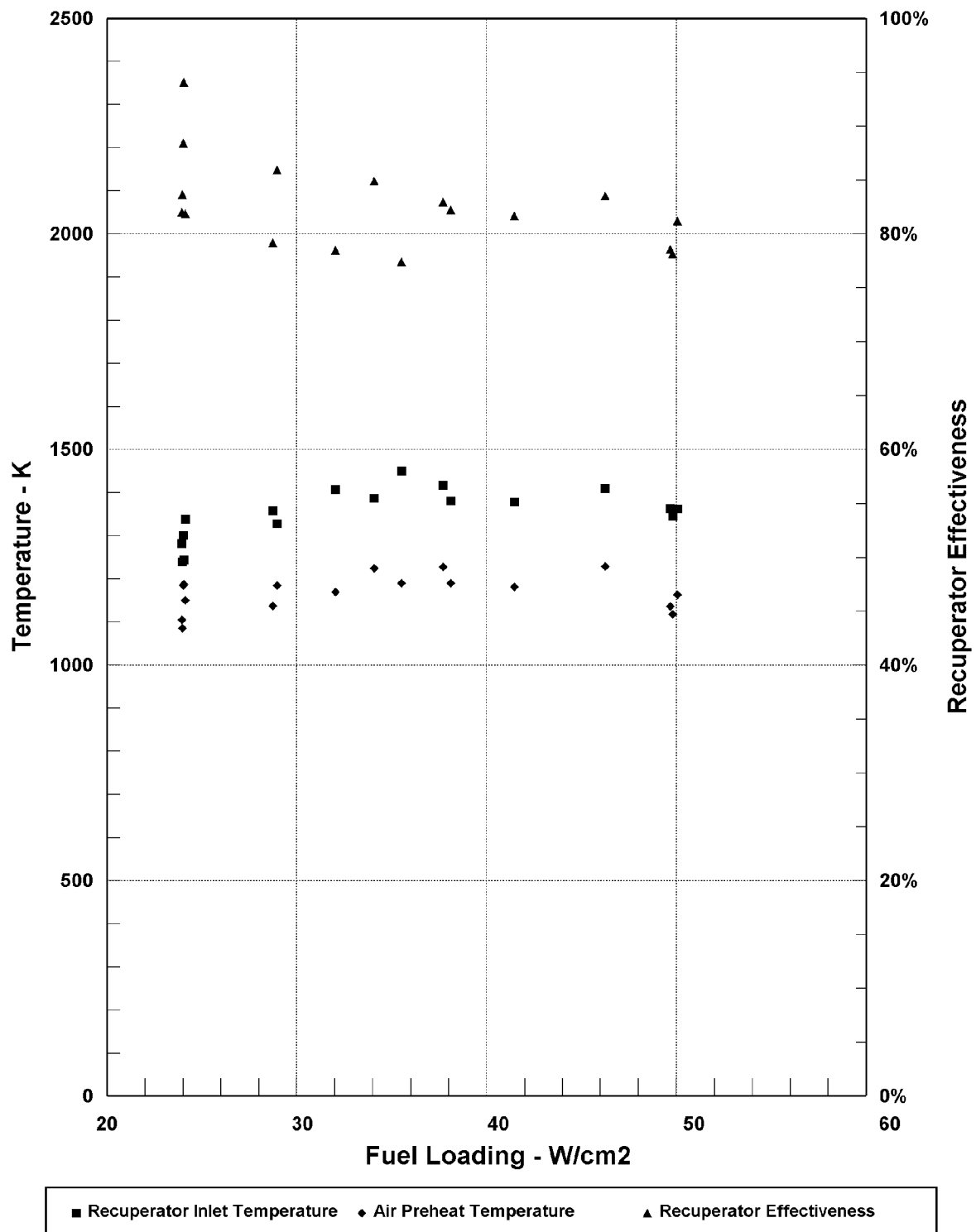


Figure 5.20 Configuration B Prototype – Test Data (No Optical Filter)

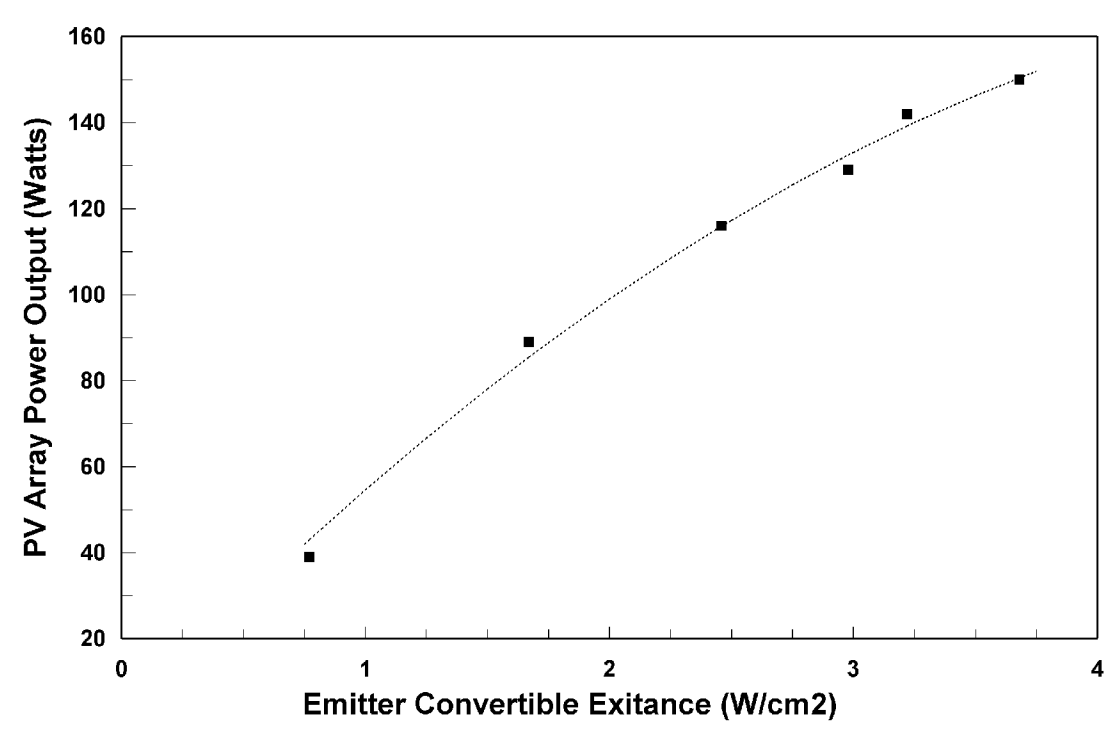


Figure 5.21 PV Array Power vs. Emitter Convertible Exitance for Configuration B Prototype

The electric power output for the Configuration B laboratory prototype, which is shown in Figure 5.21, reached 150 W (75 W per array) at an emitter convertible exitance of 3.7 W/cm^2 and an air preheat temperature of 1200 K. The fuel loading at this operating point was $\sim 52 \text{ W/cm}^2$ which resulted in a gross system efficiency of 1.0% for this prototype. Both the power output and the efficiency of this system could be increased substantially by making the following changes to the system:

- replace the current array (27% PV cells with individual cell wiring and 88% packing factor) with the new array (38% PV cells with integral cell interconnections and 100% packing factor)
- incorporate the dielectric stack filters
- raise the air preheat from 1200 K to 1350 K by increasing the recuperator core cell density from 16 cells/in² to 25 cells/in².
- improve combustion air distribution across the emitter so that the average air/fuel ratio can be reduced substantially without local fuel rich zones occurring.

Based on projections made using the results from the detailed TPV system model discussed in Chapter 6, these changes could increase the power output for this system to $\sim 290 \text{ W}$ and the gross system efficiency to $\sim 4.8\%$.

6. SINGLE MODULE TPV SYSTEM MODEL

6.1 PURPOSE

A detailed computer model was developed for a single module TPV system of the specific geometry and configuration of the systems under development. The purpose was:

- to provide an accurate model for predicting the performance of the TPV systems under development and comparing it to the test results,
- to gain a better understanding of the impact of various parameters on the performance of the overall TPV system, and
- to accurately predict the overall system performance gains that could be achieved with specific component improvements.

The predictions can readily be extended to multiple module systems.

6.2 DESCRIPTION OF MODEL

The computer model for the single module TPV system takes into account the critical thermophysical properties and dimensions of the main components which influence the performance and operating conditions of the overall system. The model breaks the TPV system into two sections, the TPV converter section and the recuperator. The TPV converter section is modeled in great detail, but the recuperator is modeled simply as a counter-flow heat exchanger with a variable effectiveness. The properties and flow rates of the combustion air and the exhaust gas and the temperature of the combustion air entering the recuperator are used in the recuperator calculations. An overall efficiency and power output estimate for the entire TPV system is made by combining the model of the TPV converter section with the characteristics of the recuperator and taking into account the combustion of the fuel and air at the emitter fibers.

The components of the TPV converter section, shown in Figure 6.1, are the emitter fibers, emitter substrate, hot window, cold window (with or without optically filtering surface), and PV array. The ambient air for combustion enters the TPV converter section as cooling air for the windows and is preheated some in the process. The combustion air flows from the windows through the recuperator, where it is preheated further before flowing back into the converter section. The combustion air then flows through the substrate and combines with the fuel just before entering the fibers. The combustion of the fuel/air mixture takes place completely within the fibers.

The TPV converter section of the computer model is used to calculate the radiative and convective heat transfer that takes place between the various components the TPV converter section.

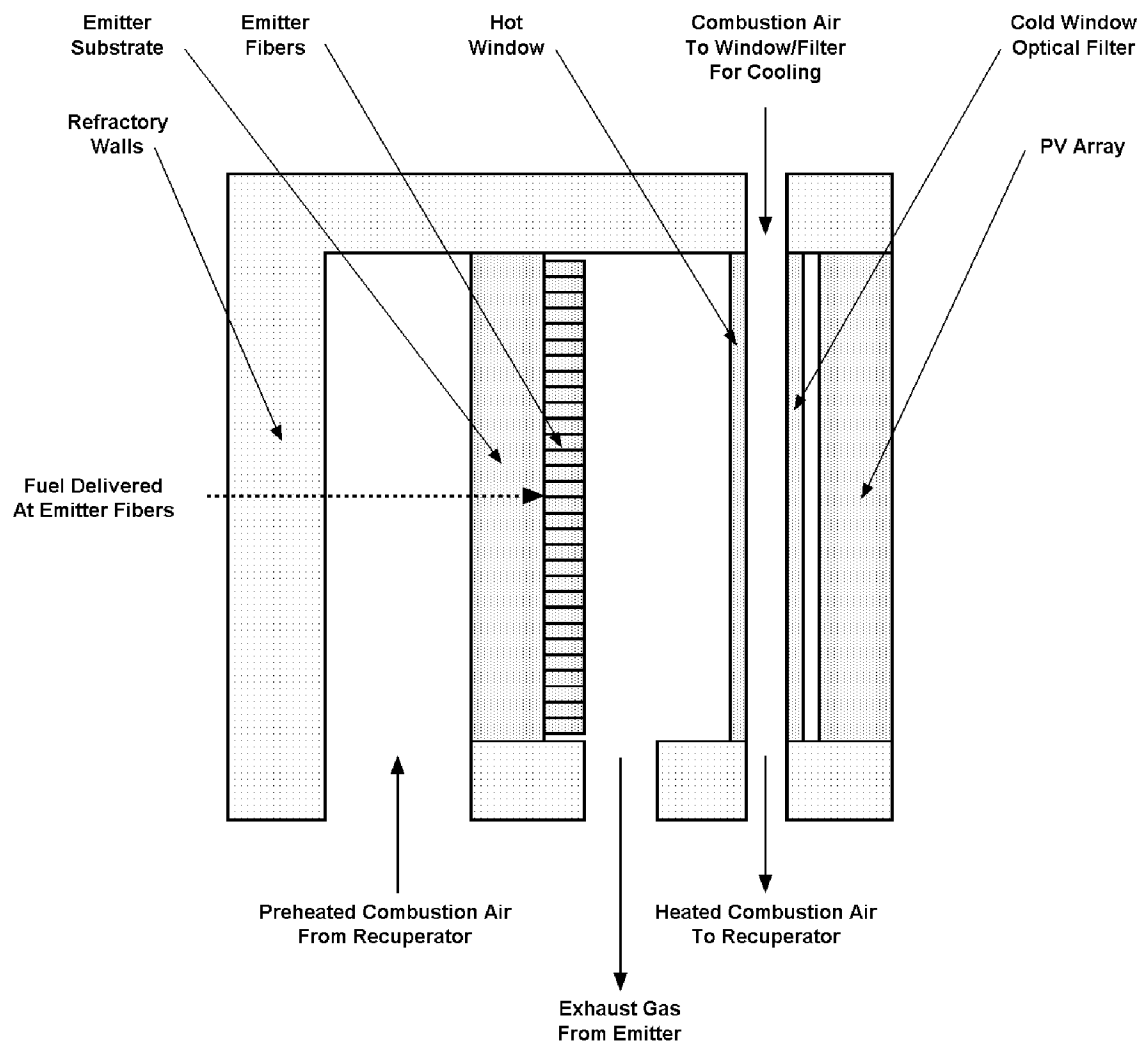


Figure 6.1 Single Module TPV System Model

The net radiation heat transfer is calculated for:

- The emitter fibers
 - to the emitter substrate
 - to the hot window
 - to the cold window/optical filter
 - to the PV array
- The emitter substrate
 - to the hot window
 - to the cold window/optical filter
 - to the PV array
- The hot window
 - to the cold window/optical filter
- The cold window/optical filter
 - to the PV array

The convective heat transfer is calculated for:

- The exhaust gas
 - to the hot window
- The hot window
 - to the cooling air
- The cold window/optical filter
 - to the cooling air

The radiation heat transfer section of the TPV system model breaks the radiation into six (6) regions, each defined by a bandwidth where the characteristics of the emitter fibers, emitter substrate, hot window, cold window (with or without optically filtering surface) and PV array are held constant. The emitter substrate is treated as a gray body (constant emissivity, typically 0.50) in all regions. Each of the other components are treated differently in each region and can be treated as an opaque body, a transparent-reflecting body, or a transparent-emitting body. The way in which each component is treated in each radiation region is defined in Table 6.1 which also shows the wavelength range used to define each region. The emissivities or transmissivities that were typically used in the calculations are also listed in the table for each component in each region. The bandwidths, emissivities and transmissivities are inputs to the model which can be easily changed.

Table 6.1 Radiation Regions and Component Treatment for TPV System Model

Region	Bandwidth	Emitter Fibers	Hot Window	Cold Window With or Without Filter	PV Array With AR Coating
1	0.00 - 0.88 m	Transparent-Emitting ($\epsilon = 0.05$)	Transparent-Reflecting ($\tau = 0.93$)	Transparent-Reflecting ($\tau = 0.93$)	Opaque-Converting ($\epsilon = 0.90$)
2	0.88 - 1.08 m	Opaque ($\epsilon = 0.65$)	Transparent-Reflecting ($\tau = 0.93$)	Transparent-Reflecting ($\tau = 0.93$)	Opaque-Converting ($\epsilon = 0.85$)
3	1.08 - 1.18 m	Transparent-Emitting ($\epsilon = 0.07$)	Transparent-Reflecting ($\tau = 0.93$)	Transparent-Reflecting ($\tau = 0.93$)	Opaque-Converting ($\epsilon = 0.85$)
4	1.18 - 3.5 m	Transparent-Emitting ($\epsilon = 0.07$)	Transparent-Reflecting ($\tau = 0.93$)	Transparent-Reflecting ($\tau = 0.14$ with filter) ($\tau = 0.93$ without filter)	Opaque- Non-Converting ($\epsilon = 0.70$)
5	3.5 - 10 m	Transparent-Emitting ($\epsilon = 0.07$)	Opaque ($\epsilon = 0.93$)	Opaque ($\epsilon = 0.15$ with filter) ($\epsilon = 0.93$ without filter)	Opaque- Non-Converting ($\epsilon = 0.60$)
6	> 10 m	Opaque ($\epsilon = 0.80$)	Opaque ($\epsilon = 0.93$)	Opaque ($\epsilon = 0.93$)	Opaque- Non-Converting ($\epsilon = 0.60$)

The insulating walls that interconnect the various components in the TPV converter section are modeled as refractory surfaces. The net radiation from the refractory walls is equal to zero and all the radiation arriving at the refractory walls is either reflected or absorbed and re-emitted. The refractory walls are also treated as diffuse with a cosine distribution of the reflected and re-emitter radiation.

The convective heat transfer that takes place within the TPV converter section results in a net loss in efficiency. Some of this loss is recovered as air preheat, but this only serves to reduce the size of the recuperator and does not raise the potential air preheat because the exhaust temperature is always high enough to provide all the air preheat needed. The heat transfer coefficients used in the calculations (typically $56.8 \text{ W/m}^2/^{\circ}\text{C}$) are somewhat higher than might actually be expected so as not to underestimate these losses and consequentially overestimate the system efficiency.

The single Module TPV System Model is set-up as a Lotus 123 spreadsheet. The emissivities or transmissivities (for the emitter fibers, emitter substrate, optical filter and PV cells in each region) and convective heat transfer coefficients are inputs to the calculation. The cold window/optical filter can be selected to be either a clear window or a window with a reflective optical. The calculation then starts with the selection of an emitter fiber temperature and a PV cell temperature. A compound iteration process is then performed to determine the combination of emitter substrate and window temperatures which produce a heat balance at the emitter substrate and the windows for a selected recuperator effectiveness.

The fuel flow is then calculated using the heating value of the fuel (typically methane), a selected air/fuel ratio (typically 10%), the specific heats of the air, fuel and exhaust gases and an assumed final exhaust gas temperature. An iteration is then carried out to obtain the correct exhaust gas temperature and fuel flow. (This iteration requires adjustments to the initial iterations of the emitter substrate and filter temperatures.) With the correct fuel flow and a PV cell efficiency and array uniformity factor, the overall TPV system efficiency and power output can then be determined.

Some of the assumptions currently built into the model are:

1. The exhaust gas temperature exiting the emitter fibers is assumed to be a fixed amount (typically 30°C) above the fiber temperature right after combustion. This temperature is then used as the exhaust gas temperature for the convective heat transfer calculations, thereby avoiding another iteration loop.
2. The exhaust gas temperature exiting the TPV converter section and entering the recuperator must be at least a minimum amount (typically 30°C) above the hot window temperature.
3. When the preheated air from the recuperator flows through the emitter substrate it can be either heated, if the substrate is hotter, or cooled, if the substrate is cooler. It is assumed that the preheated air exits the substrate a fixed amount (typically 30°C) above the substrate temperature when it is being cooled or below the substrate temperature when it is being heated. The air preheat temperature for the system is the preheat temperature exiting the recuperator, but the air preheat temperature used for the combustion process is the air temperature exiting the substrate.
4. The combustion air temperature exiting the windows and entering the recuperator must be at least a minimum amount (typically 30°C) below the cold window temperature.
5. The fuel is at ambient temperature when it mixes with the preheated air and combusts, and no dissociation of the fuel occurs before combustion takes place.

6.3 MODEL RESULTS

The Single Module TPV System Model was used to analyze various system options and the impact of various parameters on TPV system performance. Some of the results from this analysis are presented in Figures 6.2 to 6.10.

Figures 6.2 to 6.4 show calculated TPV system efficiency, TPV system power, and temperatures of the emitter substrate, hot window and cold window as a function of the air preheat temperature exiting the recuperator for an emitter temperature of 2000 K and with a dielectric stack filter on the cold window. The results are shown for two PV cell efficiencies, 27% for the PV array used in this phase of the work and 38% for the new PV cells that will be used in the next phase. The active area for the 27% efficient PV cells is 132 cm², whereas the active area for the more densely packed 38% PV cells is 144 cm². The effective area of the emitter is 145.6 cm².

For this phase of the project, we have elected to design the system to operate initially at an emitter temperature of 2000 K with a dielectric stack filter on the cold window and an air preheat temperature of 1350 K. The model predicts a TPV system efficiency of 5.2% and a power output of 115 watts with the 27% efficient PV cells. With the new 38% efficient PV cells that will be used in the next phase of the project, the predicted TPV system efficiency increases to 8.0% and the power output to 177 watts. The predicted ratio of the in-band (wavelength < 1.18 microns) radiation to the total radiation arriving at the PV array is 41.7%. The predicted temperatures for the emitter substrate, hot window and cold window are 1713 K, 1399 K, and 972 K respectively. These temperatures and the convertible fraction are independent of the PV cell efficiency.

Figures 6.5 to 6.7 show calculated TPV system efficiency, TPV system power, and temperatures of the emitter substrate, hot window and cold window as a function of the air preheat temperature exiting the recuperator for an emitter temperature of 2000 K and with no optical filter on the cold window. The results are again shown for PV cell efficiencies of 27% and 38%. Not using the dielectric stack filter would reduce the TPV system efficiency to ~3% and the power output to ~95 watts with the 27% efficient PV cells and to ~4.5% and ~148 watts with the 38% efficient PV cells at the same emitter temperature of 2000 K and air preheat temperature of 1350 K. The predicted ratio of the in-band (wavelength < 1.18 microns) radiation to the total radiation arriving at the PV array drops to ~21% without the dielectric stack filter. This illustrates the substantial impact that the dielectric stack filter can have on the system performance. The predicted temperatures for the emitter substrate, hot window and cold window are much lower without the dielectric stack filter at ~1385 K, ~1108 K, and ~860 K respectively.

Figures 6.8 to 6.10 show calculated TPV system efficiency, TPV system power, and temperatures of the emitter substrate, hot window and cold window as a function of the emitter temperature for a recuperator effectiveness of 90% and with a dielectric stack filter on the cold window. The results are again shown for PV cell efficiencies of 27% and 38%. The results indicate that increasing the emitter temperature to 2050 K, with a recuperator effectiveness of 90% (~1650 K air preheat temperature), would increase the TPV system efficiency to 10.3% and the power output to 236 watts with 38% efficient PV cells.

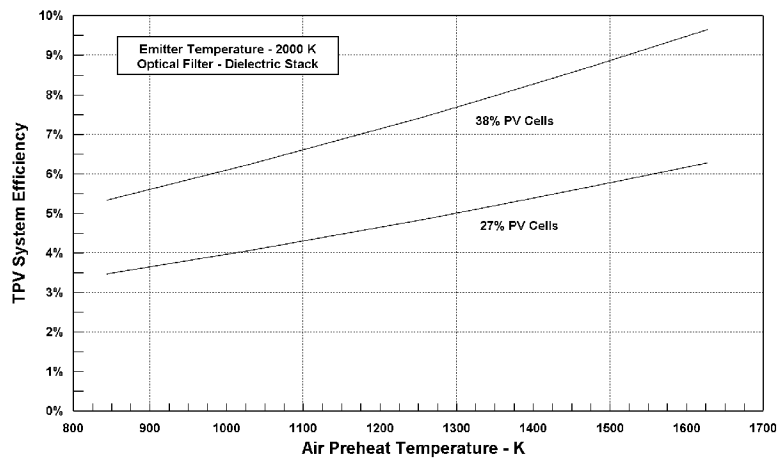


Figure 6.2 TPV System Model Results – One Module Size

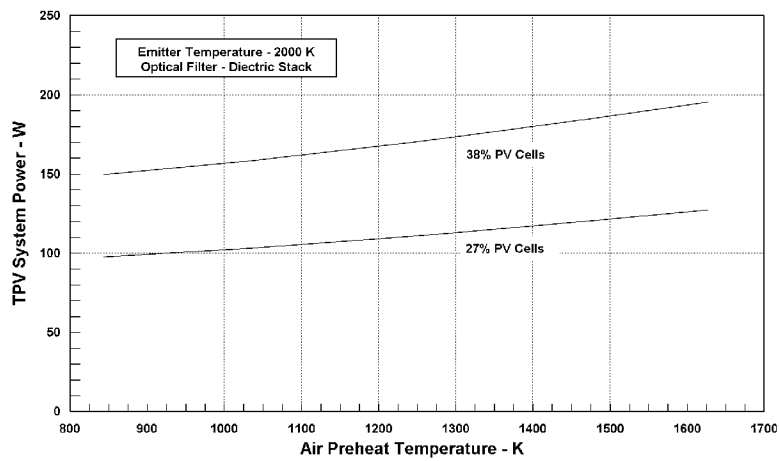


Figure 6.3 TPV System Model Results – One Module Size

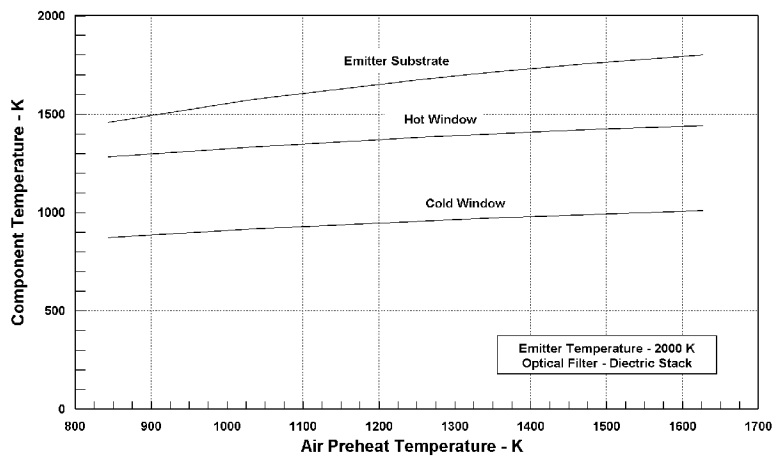


Figure 6.4 TPV System Model Results – One Module Size

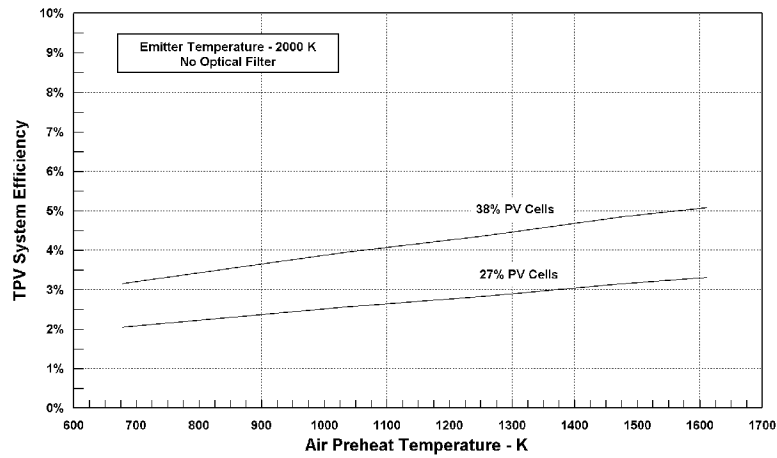


Figure 6.5 TPV System Model Results – One Module Size

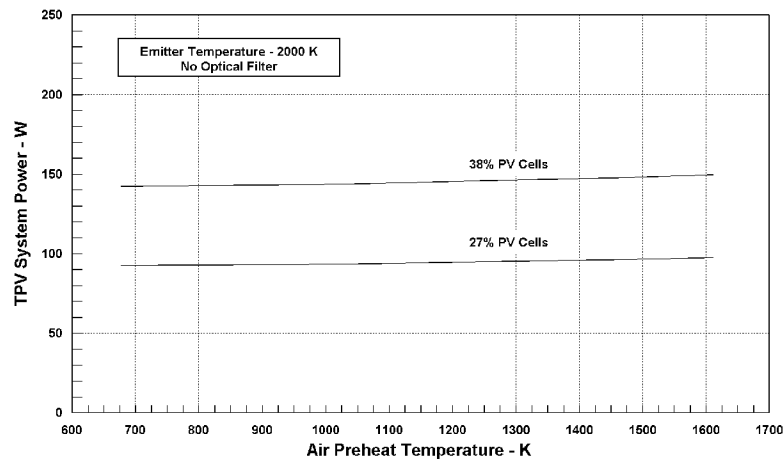


Figure 6.6 TPV System Model Results – One Module Size

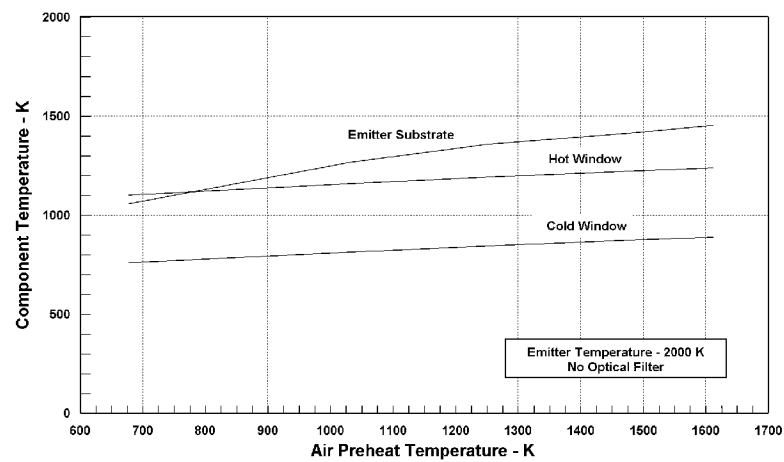


Figure 6.7 TPV System Model Results – One Module Size

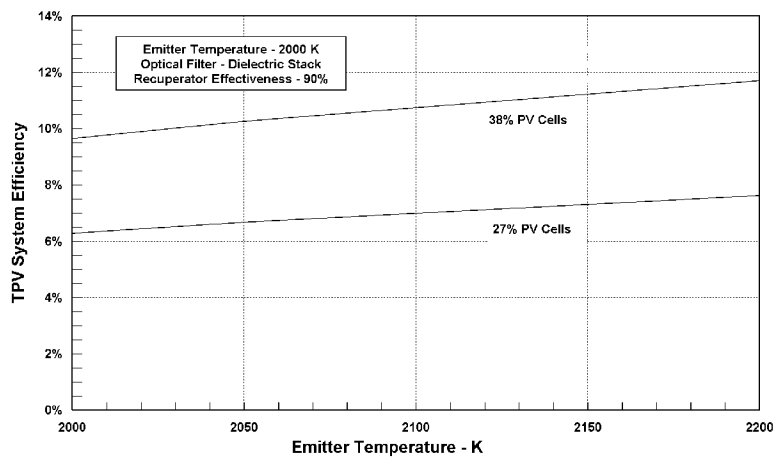


Figure 6.8 TPV System Model Results – One Module Size

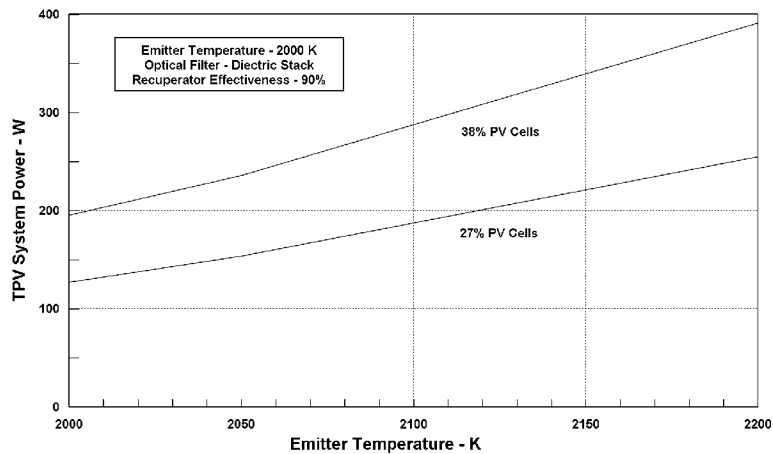


Figure 6.9 TPV System Model Results – One Module Size

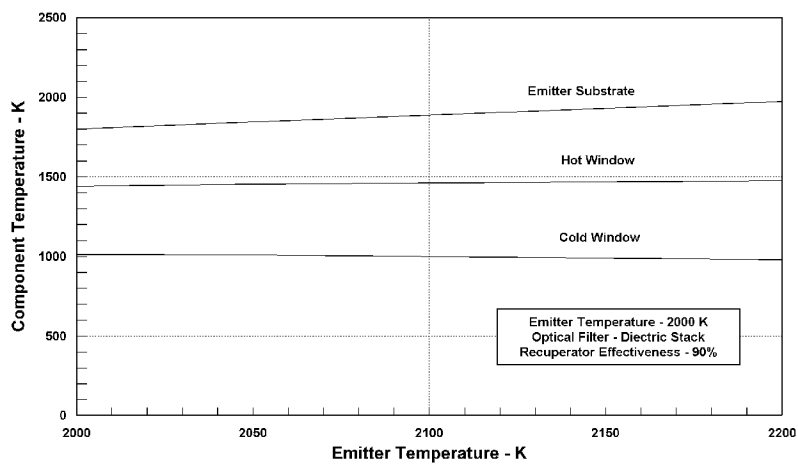


Figure 6.10 TPV System Model Results – One Module Size

7. CONCLUSIONS

The work covered by this report has successfully demonstrated the operation of laboratory prototype TPV systems that used wavelength selective emitters radiating to bandgap matched photovoltaic cells. To enhance performance, the systems also used both optical and thermal recuperation. Specific accomplishments of this work included:

- extensive testing of two laboratory prototype TPV generators
- operating these systems with emitter temperatures of 2000 K and air preheat temperatures of 1350 K for many hours
- developing and demonstrating the feasibility of the micromixed surface combustion concept needed to:
 - initiate and complete the combustion process within the ytterbia ceramic fibers of the emitter
 - operate the emitter fibers at 2000 K with uniform temperature across the entire emitter surface
 - operate with air preheat temperatures (1350 K), which are well above the auto-ignition temperature of the fuel (methane), without pre-igniting the fuel in the recuperator or emitter support structure
- developing and demonstrating a dielectric optical filter which resulted in a 50% convertible radiation fraction at the PV array
- developing and demonstration of a ceramic recuperator capable of producing air preheat temperatures up to 1350 K.
- achieving a power output from a two emitter system of 150 W at an emitter convertible exitance level of 3.7 W/cm^2 .

The development by TECSTAR of silicon PERL cells, whose performance was optimized for the operating characteristics of the Thermo Power fibrous ytterbia emitter, was not successful and this compromised the overall performance of the systems. The design objective for the PERL cell development was a peak monochromatic efficiency of about 45% at or beyond the 980 nm wavelength where the ytterbia peak emission is centered. Figure 7.1 shows the spectral exitance of the fibrous ytterbia emitter and the spectral efficiency of the PERL cells supplied by TECSTAR. The TECSTAR PV cells had a peak monochromatic efficiency of 35% at 920 nm. At the ytterbia emission peak of 980 nm, the monochromatic efficiency of these cells dropped to 33% and continued to drop at higher wavelengths where the ytterbia emitter was still emitting strongly. As a result, the overall efficiency of these PV cells in converting radiation below 1180 nm was reduced to 27% when matched with the ytterbia emitter.

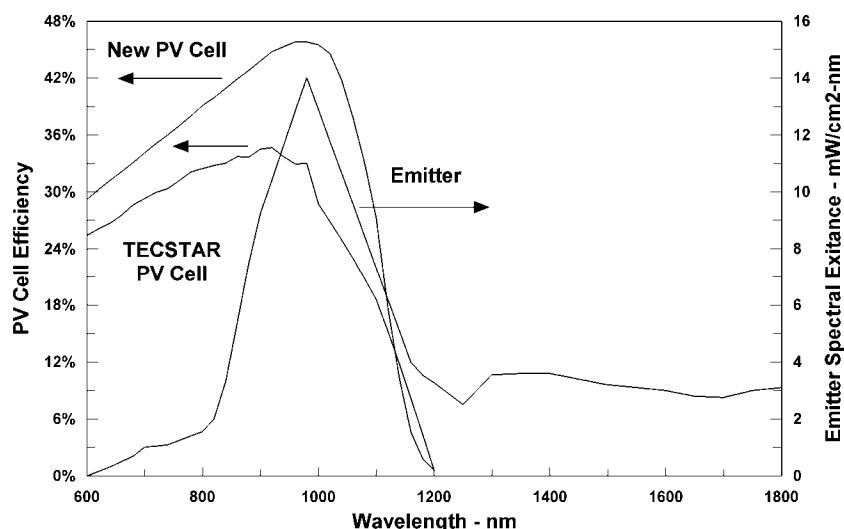


Figure 7.1 PV Cell Efficiency and Emitter Spectral Exitance vs. Wavelength

The spectral characteristics for the "New PV cells", which will be used in the next generation prototype, are also presented in Figure 7.1. These cells, which will be supplied by SunPower Corporation, are much better matched to the ytterbia emitter characteristics. As shown in Figure 7.1, the peak monochromatic efficiency for these cells is 46% and occurs at the ytterbia peak of 980 nm. With the better matching characteristics and higher peak efficiency, the new PV cells have an overall efficiency of 38% when matched with the ytterbia emitter. The open circuit voltage, short circuit current, fill factor, peak power and overall efficiency for each of these cells are listed in Table 7.1.

Table 7.1 PV Cell Characteristics

	TECSTAR PV Cells	New PV Cells
Voc – Volts	0.79	0.77
Isc – A/cm ²	1.59	2.04
FF	0.72	0.80
PM – A/cm ²	0.90	1.26
Responsivity – A/W	0.47	0.61
Efficiency	27%	38%

Figure 7.2 shows the measured power output for a two-module prototype as a function of the convertible exitance at the emitter for the TECSTAR PV arrays, and the projected power for arrays with the new high efficiency PV cells. A peak power of 150 watts was measured with the TECSTAR array at an emitter convertible exitance of 3.7 W/cm². At the same emitter convertible exitance level, the arrays with the new high efficiency PV cells should produce 290 watts. The higher power output projected for the new arrays also includes the impact of the higher packing factor and lower cell interconnection losses which are achievable with the new PV cells.

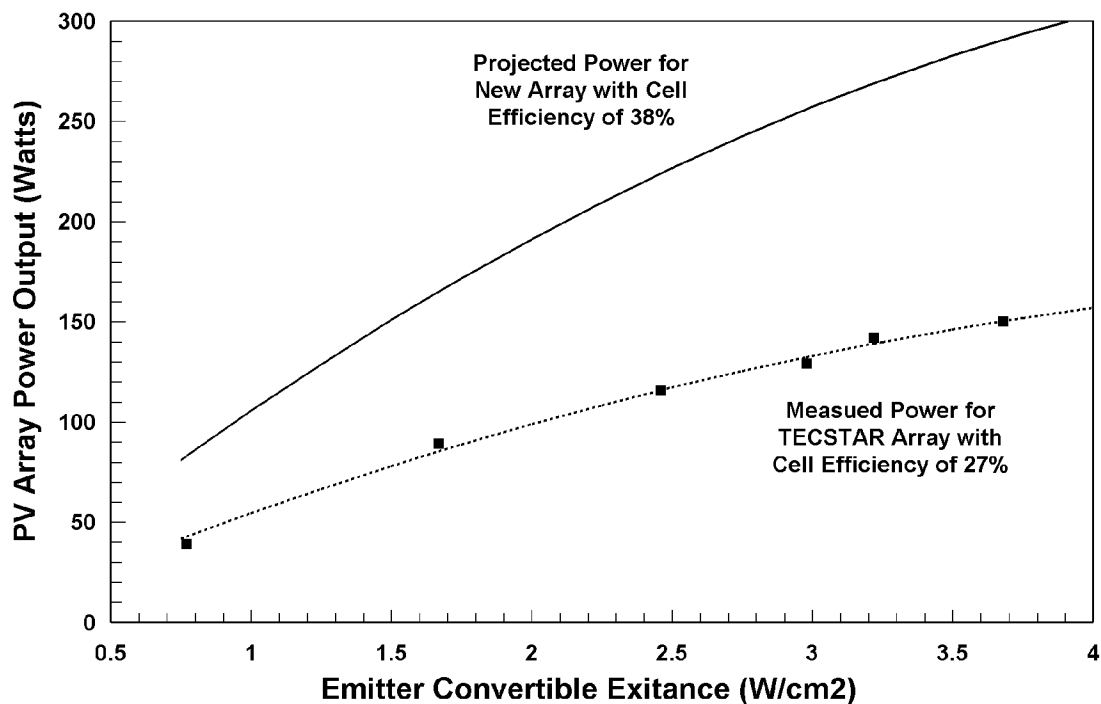


**Figure 7.2 PV Array Power vs. Emitter Convertible Exitance
for a Two-Module Laboratory Prototype**

The power increase with the new array will also result in a corresponding increase in the overall system efficiency. Substantial further increases in the overall efficiency will be made by incorporating the dielectric stack filters, raising the air preheat from 1200 K to 1350 K by increasing the recuperator core cell density from 16 cells/in² to 25 cells/in², and improving combustion air distribution across the emitter so that the average air/fuel ratio can be reduced substantially without local fuel-rich zones occurring. Based on projections made using the results from the detailed TPV system model, these changes could increase the overall system efficiency from the 1.0% measured with the two emitter prototype to ~4.8%.

In conclusion, the work performed on the program to date has identified the technological pathways for the development of efficient, portable thermophotovoltaic power sources in the power range of 100 to 500 watts. The technology is based on the use of rare earth selective emitters and matched photovoltaic cells. Highly efficient thermal and optical energy recovery are also an integral part of the technology. The technology has been demonstrated at the laboratory prototype level where the key components of the system – emitter, PV array, recuperator, and optical filter – have been integrated into an operating prototype. Future plans are to build and demonstrate a completely self-contained, portable TPV power source based on this technology.

REFERENCES

1. Krist, K, "GRI Research on Thermophotovoltaics", The First NREL Conference on Thermophotovoltaic Generation of Electricity, Copper Mountain, 1994, pp. 54-63.
2. Becker, F.E., Doyle, E.F., Shukla, K., "Development of a Portable Thermophotovoltaic Power Generator," The Third NREL Conference on the Thermophotovoltaic Generation of Electricity, Colorado Springs, 1997.
3. Becker, F.E., Doyle, E.F., Mastronardi, R., Shukla, K., Linder, E.B., and Garverick, L.M., "Development of a 500 Watt Portable Thermophotovoltaic Power Generator," Twenty-Fifth IEEE Photovoltaic Specialists Conference, Washington, D.C., 1996, pp. 1413-1416.
4. Becker, F.E., "Recuperators for Thermophotovoltaic Energy Conversion Systems," Prospector VIII: Thermophotovoltaics – An Update on DOD, Academic, and Commercial Research, sponsored by Space Power Institute. Auburn University, Alabama and Army Research Office, Research Triangle Park, North Carolina, July 14-17, 1996, Edited by M. Frank Rose, pp. 173-194.
5. Doyle, E.F., "System Aspects of TPV Energy Conversion," Prospector VIII: Thermophotovoltaics – An Update on DOD, Academic, and Commercial Research, sponsored by Space Power Institute. Auburn University, Alabama and Army Research Office, Research Triangle park, North Carolina, July 14-17, 1996, Edited by M. Frank Rose, pp. 173-194.
6. Nelson, R.E., "Grid Independent Residential Power Systems," The Second NREL Conference on Thermophotovoltaic Generation of Electricity, Colorado Springs, 1995, pp. 221-237.
7. Nelson, R.E., "Thermophotovoltaic Emitter Development," The First NREL Conference on Thermophotovoltaic Generation of Electricity, Copper Mountain, 1994, pp. 80-95.

REPORT DOCUMENTATION PAGE			Form Approved OMB No. 0704-0188	
Public reporting burden for this collection of information is estimated to average 1 hour per response, including the time for reviewing instructions, searching existing data sources, gathering and maintaining the data needed, and completing and reviewing the collection of information. Send comments regarding this burden estimate or any other aspect of this collection of information, including suggestions for reducing this burden, to Washington Headquarters Services, Directorate for Information Operations and Reports, 1215 Jefferson Davis Highway, Suite 1204, Arlington, VA 22202-4302, and to the Office of Management and Budget, Paperwork Reduction Project (0704-0188), Washington, DC 20503.				
1. AGENCY USE ONLY (Leave blank)		2. REPORT DATE December 1998		3. REPORT TYPE AND DATES COVERED Final Contractor Report
4. TITLE AND SUBTITLE Thermophotovoltaic Energy Conversion Development Program			5. FUNDING NUMBERS WU-632-1A-1A-00 NAS3-27565	
6. AUTHOR(S) Kailash Shukla, Edward Doyle, and Frederick Becker				
7. PERFORMING ORGANIZATION NAME(S) AND ADDRESS(ES) Thermo Power Corporation Tecogen Division 45 First Ave. Waltham, Massachusetts 02454-9046			8. PERFORMING ORGANIZATION REPORT NUMBER E-11284	
9. SPONSORING/MONITORING AGENCY NAME(S) AND ADDRESS(ES) National Aeronautics and Space Administration Lewis Research Center Cleveland, Ohio 44135-3191			10. SPONSORING/MONITORING AGENCY REPORT NUMBER NASA CR-1998-208512 TR7020-003-98	
11. SUPPLEMENTARY NOTES Project Manager, David M. Wilt, Power and On-Board Propulsion Technology Division, NASA Lewis Research Center, organization code 5410, (216) 433-6293.				
12a. DISTRIBUTION/AVAILABILITY STATEMENT Unclassified - Unlimited Subject Category: 44 This publication is available from the NASA Center for AeroSpace Information, (301) 621-0390.			12b. DISTRIBUTION CODE Distribution: Nonstandard	
13. ABSTRACT (Maximum 200 words) Completely integrated thermophotovoltaic (TPV) power sources in the range of 100 to 500 watts are being developed. The technical approach taken in this project focuses on optimizing the integrated performance of the primary subsystems in order to yield high energy conversion efficiency and cost effectiveness. An important aspect of the approach is the use of a narrow band fibrous emitter radiating to a bandgap matched photovoltaic array to minimize thermal and optical recuperation requirements, as well as the non-recoverable heat losses. For the prototype system, fibrous ytterbia emitters radiating in a narrow band centered at 980 nm are matched with high efficiency silicon photoconverters. The integrated system includes a dielectric stack filter for optical energy recovery and a ceramic recuperator for thermal energy recovery. The prototype TPV system uses a rapid mix distributed fuel delivery system with controlled feeding of the fuel and heated air into a flame at the surface of the emitter. This makes it possible to operate at air preheat temperatures well above the auto-ignition temperature of the fuel thereby substantially increasing the system efficiency. The system has been operated with air preheat temperatures up to 1367 K and has produced a uniform narrow band radiation over the surface of the emitter with this approach. The design of the system is described and test data for the system and some of the key components are presented. The results from a system model, which show the impact of various parameters on system performance, are also discussed.				
14. SUBJECT TERMS Thermophotovoltaics; Wavelength-selective radiators; Emitters; Concentrator PV silicon cells; TPV optical filters			15. NUMBER OF PAGES 95	
			16. PRICE CODE A05	
17. SECURITY CLASSIFICATION OF REPORT Unclassified	18. SECURITY CLASSIFICATION OF THIS PAGE Unclassified	19. SECURITY CLASSIFICATION OF ABSTRACT Unclassified	20. LIMITATION OF ABSTRACT	